International Relativistic Astrophysics PhD
Erasmus Mundus

Università degli Studi di Ferrara

PhD Thesis

Extending the band of focusing X-ray telescopes beyond 100 keV: motivations and proposed solutions

Supervisor
Prof. Filippo Frontera

Co-supervisor
Dr. Enrico Virgilli

Candidate
Vineeth Valsan

2010–2013

To the thoughts that move me forward

Acknowledgements

"*But, I am an engineer, with only very basic knowledge in physics*"
"*This project is not far from engineering and you have the will power. We will do it together.*"

This was one of the first conversations that was exchanged between my supervisor, **Prof. Filippo Frontera** and myself. Even though I liked the subject, the initial uneasiness of a nervous – me, in dealing with this subject, was slowly and steadily wiped out with these words. I will always be indebted to him for giving me an insight into this wonderful topic. He was always there to help whenever required, and I couldn't have asked for more. I am very much grateful and looking forward to work with him in the years to come.

This subject became even more interesting, thanks to my friend and big-brother (co-guide, of course), **Enrico Virgilli**. His funny, quick and smart way of thinking has always left me spellbound. A great companion, he is the core of friends network that I have here in Ferrara. I am also thankful to him for inclining me towards *ginnastica* and playing *calcetto*.

Over these three years, I was fortunate to have a blameless *coinquilino*, **Vincenzo Liccardo**. My collaborator in the lab, a great photographer and a great chef, he has whole heartedly made a number of delicious Italian cuisines, including *gnocchi-ardo*, all of which I have enjoyed a lot. Words of gratitude will not be enough for his everlasting friendship.

I would really like to thank my friend, **Alessandro Pisa**, for the incredible foundation he has made for the simulation aspect of focusing high energy photons using crystals. The algorithm that he has written has highly influenced my works on simulation and modelling for the Laue project.

Experimental stages are always with unlikely and untimely event of hitches. **Vito Carassiti**, **Stefano Squerzanti** and **Marco Statera** were always there to help us at these times. I am thankful to them for their aid, without which this

project would have faced enormous delay.

Ezio Caroli and **John B. Stephen** are two of the energetic people, I have ever met, who make the work domain, an adobe. The charm and liveliness they posses along with their intellect, were very helpful for me in my work. I am thankful to both of them for providing me with the necessary data and also for umpteen lively discussions about ethical and unethical (but healthy) topics. I also thank **Natalia Auricchio** for her time to time support in dealing with the detectors.

I thank **Manuel Sànchez Del Rìo**, for his kindness to provide me with the latest copy of XOP program, that he had written. His hospitality in ESRF, Grenoble is also worth mentioning.

My humble thanks to **Prof. Piero Rosati** for taking his time to give me his valuable comments and suggestions related to my work and presentation.

My heartfelt gratefulness also goes to **Stefano Silvestri** and **Angelo Basili** for the humorous environment they provided during the final year of my thesis and of course, also for numerous *colazioni*.

I also thank IRAP–PhD program director **Prof. Remo Ruffini** and co-ordinator **Prof. Pascal Chardonet**, without whose efforts this program would have been lifeless.

Special mentioning should be made for **Biju**, **Jasmine** and their little angel, **Savio**, who have provided me shelter, food and most importantly for their affection in the days of writing my thesis.

The unconditional love and support I get from my family is the backbone to the thoughts that move me forward. My parents and my sister have always been there for me. Heartfelt blessings from sagacious and thoughtful people, including my grandparents, is a source of positive energy that I have felt all these years. I will always be beholden to these vibrant people.

I acknowledge the support from Erasmus Mundus Joint Doctorate Program by Grant Number 2010-1816 from the EACEA of the European Commission.

The LAUE project is the result of huge efforts of large number of organizations and people. I would like to thank all of them. I also acknowledge the ASI (Italian Space Agency) for its support to the LAUE project under contract I/068/09/0.

Contents

List of Figures

List of Tables

Chapter 1

Justification for the need of a Laue lens

The main motivations that justify the need of new focusing optics for hard X–rays to overcome the sensitivity limitations of the presently employed direct–view telescopes, are inscribed in this introductory chapter. The available solutions are presented and the Laue lenses, principal subject of this thesis, are finally introduced.

1.1 Introduction

The telescopes in the X–/ soft Gamma ray band can be divided into two categories depending upon their configuration for collecting the photons. The *direct–view telescopes* are mainly detectors provided with collimator and/or coded masks. The *focusing telescopes* are the ones employing focusing optics. The latter category of telescopes concentrates the collected photons on the focal plane, where the detectors will be placed.

To explore the hard X-ray / soft Gamma ray band, direct–view telescopes are being used. The advantages of focusing telescopes are exploited only up to 80 keV. The *NuSTAR* mission [53], with on board, two focusing telescopes operating in the 3–79 keV band, is performing very sensitive (10^{-8} photons cm^{-2} s^{-1} keV^{-1}) studies of the hard X–ray sky. A significant part of the *NuSTAR* core program time is devoted to sensitive studies of extragalactic and Galactic surveys, which will supplement the extended surveys beyond 20 keV already performed [9, 19] or planned to be continued with the INTEGRAL observatory [103], and with the *Swift* satellite [42].

Evidence of extended matter-antimatter annihilation emission (at 511 keV) from the Galactic Center [99] and of Galactic nucleosynthesis processes [99, 26] has been found with INTEGRAL. Furthermore, polarization of high energy photons (> 400 keV) emitted from a strong source like the Cygnus X-1 has been clearly measured [57].

However, in order to take full advantage of these results, a new generation of focusing telescopes which extend the energy band up to several hundreds of keV is needed. In spite of its high sensitivity, *NuSTAR* optics are based on multilayer reflectivity and therefore are limited in the energy passband. A focusing telescope that could extend the band upto several hundreds of keV would allow two–order of magnitude increase in sensitivity and angular resolution and thus a leap forward in our understanding of the (especially non–thermal) processes occurring in the Universe, in similar way to the leap obtained with the soft X–ray optics in the seventies.

Laue lenses, based on diffraction from crystals in transmission configuration, offer the best technical solution to the implementation of a focusing telescope that can extend the energy band beyond 80 keV. Indeed, the adoption of grazing incidence mirrors, like those used for the telescopes aboard, e.g., *Chandra* or *XMM-Newton*, or of multilayer mirrors, like those used for the *NuSTAR* telescopes, would require hundred meter focal lengths to extend the energy band up to several hundreds of keV. The advantage of Laue lenses is that we can extend the band up to 600 keV with a focal length of about 20 m, which is still feasible with a single satellite.

In order to understand the parameters that govern the value of the sensitivity, the sensitivity calculation (Continuum as well as line sensitivity) for both focusing and direct–view telescopes is derived and presented in Sections 1.2.2 and 1.2.3.

1.2 Telescope parameters

The different parameters that quantify the observational limits of a high energy telescope are discussed in this section.

1.2.1 Angular resolution

Angular resolution of a telescope is defined as its ability to resolve two point sources. The Rayleigh criterion is a theoretical criterion to establish this phenomenon. The angular resolution, θ_T of a telescope is given by

$$\begin{aligned} \theta_T &= 1.22\frac{\lambda}{D} \quad \textit{(in radians)} \\ \theta_T &= 251643\frac{\lambda}{D} \quad \textit{(in arcsec)} \end{aligned} \tag{1.1}$$

where λ is the radiation wavelength and $D(=2R)$ corresponds to the telescope objective diameter. Also, $\lambda = \dfrac{hc}{E}$, E being the corresponding energy in keV.

These formulae give the maximum limit that can be achieved theoretically. Practically, the angular resolution depends upon various factors (e.g. the quality of the reflecting

mirrors) that limit the maximum achievable value. In the case of a lens we expect to achieve an angular resolution of about 30 arcsec.

1.2.2 Continuum sensitivity

Sensitivity of a telescope is defined as the minimum intensity, I_s^{min} which can be "detected" in an observation time T_{obs}. The expression for continuum sensitivity is different for a direct viewing telescope and for a focusing telescope.

1.2.2.1 Case of direct–view telescopes

Let N_{tot} be the number of photons counted by the detector of a direct–view telescope, in a time interval T_{obs} and within an energy band ΔE around the energy E. N_{tot} can be expressed as:

$$N_{tot} = N_S + N_B \tag{1.2}$$

where, N_S are counts due to the photons from the X–ray source and N_B are the counts due to the telescope background. For a direct–view telescope, N_S and N_B are given by:

$$N_S = \eta_d A_d T_{obs} I(E) \Delta E \tag{1.3}$$

$$N_B = A_d T_{obs} B(E) \Delta E \tag{1.4}$$

where,

- η_d is the detector efficiency;
- A_d is the detector area;
- $I(E)$ is the photon intensity (in photons/s/cm^2/keV), at energy E coming from the X–ray source;
- $B(E)$ is the intensity of the measured background spectrum (in counts/s/cm^2/keV) at the energy E;

What we need is the information on the source intensity, I(E), which is contained in N_S. This can be derived subtracting from the total counts the background counts.

$$N_S = (N_S + N_B) - N_B \tag{1.5}$$

$$= N_{tot} - N_B \tag{1.6}$$

Assuming Poisson statistics, the standard deviation of the counts due to the source is given by:

$$\sigma_{N_S} = \sqrt{\sigma^2_{N_{tot}} + \sigma^2_{N_B}} \tag{1.7}$$
$$= \sqrt{N_{tot} - N_B} \tag{1.8}$$

where $\sigma^2_{N_{tot}}$ and $\sigma^2_{N_B}$ are the variances of N_{tot} and N_B respectively. This expression for σ_{N_S} is valid if the flux from the source and from the background are uncorrelated.

When the number of counts is dominated by the background, i.e., $N_S \ll N_B$, (this assumption is taken in order to evaluate the sensitivity), we get

$$\begin{aligned} \sigma_{N_S} &\approx \sqrt{2\sigma^2_{N_B}} \\ &= \sqrt{2B(E)A_d T_{obs}\Delta E} \end{aligned} \tag{1.9}$$

Let n_σ be the standard deviation corresponding to a given confidence level. For e.g., at 99.7% confidence level, the number of standard deviation is 3. Hence,

$$\begin{aligned} N_S^{min} &= \eta_d A_d T_{obs} I_{dv}^{min}(E)\Delta E \\ &= n_\sigma \sqrt{2B(E)A_d T_{obs}\Delta E} \end{aligned} \tag{1.10}$$

from which the minimum source intensity, $I_{dv}^{min}(E)$, that can be detected with a direct–view telescope at a confidence level corresponding to n_σ, is given by:

$$I_{dv}^{min}(E) = \frac{n_\sigma}{\eta_d}\sqrt{\frac{2B(E)}{A_d T_{obs}\Delta E}} \tag{1.11}$$

From the above equation it is clear that in order to improve the sensitivity of a direct–view telescope, it is necessary to decrease the background. Increasing the detector area A_d will also yield a better sensitivity. However the sensitivity dependence on A_d implies that the minimum detectable intensity decreases by a factor 10 when the detector surface increases by a factor 100. This is the limit of a direct view telescope.

1.2.2.2 Case of focusing telescopes

For a focusing telescope, the background remains the same as that of equation 1.4. But due to the focusing optics, the number of counts, N_S is given by:

$$N_S = \eta_d f_\epsilon A_{eff} T_{obs} I(E)\Delta E \tag{1.12}$$

where,

- f_ϵ is the fraction of photons that is focused on the detector. It depends on the response function of the telescope to a point-like celestial source (called Point Spread Function or PSF), that is inside the section A_d of the focal plane detection surface. For example, $f_\epsilon = 0.5$ if the number of photons in A_d is 50% of the total reflected photons. In this case $A_d = \pi R^2_{hpr}$ where, R_{hpr} is known as the Half Power Radius.

- A_{eff} is the effective area at an energy E of the telescope optics, given by the product of the geometrical area of the optics times its reflection efficiency at the same energy E.

Following the same steps that lead to the equation 1.11, the sensitivity $I_{ft}^{min}(E)$ of a focusing telescope, at a confidence level corresponding to n_σ, can be derived to:

$$I_{ft}^{min}(E) = \frac{n_\sigma}{\eta_d f_\epsilon A_{eff}} \sqrt{\frac{2B(E)A_d}{T_{obs}\Delta E}} \tag{1.13}$$

Here, more generally, $A_d (= \pi R_{spot}^2)$ is the part of the detector area in which the fraction f_ϵ of the total reflected photons are contained. If the total noise measured is only due to the background under the source photon distribution i.e., if the background outside PSF, can be determined with high accuracy. For example, by taking an average of the values measured in more contiguous regions, the instrument sensitivity, $I_{ft}^{min}(E)$ at the confidence level corresponding to n_σ is given by:

$$I_{ft}^{min}(E) = \frac{n_\sigma}{\eta_d f_\epsilon A_{eff}} \sqrt{\frac{B(E)A_d}{T_{obs}\Delta E}} \tag{1.14}$$

From equation 1.14 we see that the sensitivity is directly proportional to the square root of the detector area A_d and inversely proportional to the effective area A_{eff}. Hence decreasing the detector area and increasing the effective area of the the telescope contributes to a better sensitivity. A comparison of the sensitivity at the confidence level corresponding to 3σ, for different instruments (focusing or not), is shown in Figure 1.1.

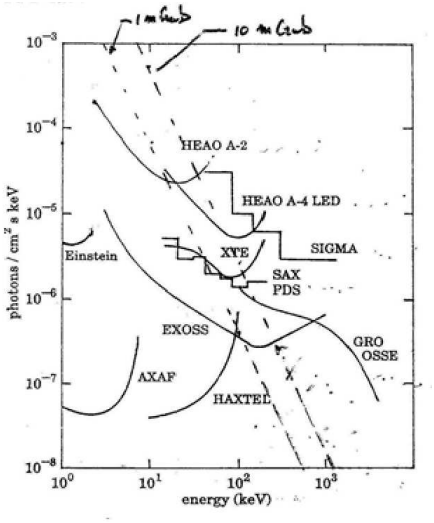

Figure 1.1: 3σ sensitivity estimated for the most important hard X–ray experiments (flown or proposed) in the 90s as a function of energy.

1.2.3 Sensitivity to narrow emission lines

The sensitivity to narrow emission lines is derived by superposing the continuum source level to the emission line. Due to the finite energy resolution of the instrument, it can be assumed that the line is having a Gaussian shape.

$$G(E) = \frac{I_L}{\sqrt{2\pi}\sigma_E} \exp\left[-\frac{(E-E_L)^2}{2\sigma_E^2}\right] \tag{1.15}$$

Where, E_L is the centroid energy of the emission line and σ_E is the standard deviation.

From the properties of the Gaussian distribution, the integral of the line is equal to I_L and the Full Width at Half Maximum (FWHM) is given by

$$\begin{aligned} \Delta E &= \sqrt{8\ln 2}\sigma_E \\ &= 2.35\sigma_E \end{aligned} \tag{1.16}$$

The intensity of the line can be determined from the estimate of the counts in ΔE, equal to 0.76 I_L, i.e.,

$$\int_{E_L-\Delta E/2}^{E_L+\Delta E/2} G(E)dE = 0.76 I_L \tag{1.17}$$

The line sensitivity is different for direct–view telescopes and focusing telescopes.

1.2.3.1 Case of direct–view telescopes

Assuming that the continuum level can be accurately determined, the signal S, noise N and signal to noise ratio $\frac{S}{N}$ is given by

$$S = 0.76 I_L \eta_d A_u T_{obs} \tag{1.18}$$

$$N = \sqrt{I_C(E_L)\eta_d A_u T_{obs}\Delta E + 2B(E_L)A_t T_{obs}\Delta E} \tag{1.19}$$

$$\frac{S}{N} = \frac{0.76 I_L \eta_d A_u T_{obs}}{\sqrt{I_C(E_L)\eta_d A_u T_{obs}\Delta E + 2B(E_L)A_t T_{obs}\Delta E}} \tag{1.20}$$

where,

- I_L is the intensity of the line corresponding to the centroid energy, E_L;
- η_d is the detector efficiency at photons of energy E_L;
- A_u is the useful geometric area (or cross section) of the detector (i.e., that area seen through the field collimator) exposed to the source;
- T_{obs} is the observation time of the source, assumed to be identical to the measurement time duration of the background;

- $B(E_L)$ is the instrumental background of the detector corresponding to the energy E_L;
- A_t is the total geometric area of the detector;
- $I_c(E_L)$ is the source continuum intensity (in $photons/s/cm^2/keV$) at the centroid of the line.

From the above equations, the minimum detectable intensity, $I^{min}_{L_{dv}}$, (in $photons\ s^{-1}\ cm^{-2}$) of a line for a direct–view instrument can be derived, and is given by:

$$I^{min}_{L_{dv}} = 1.31 n_\sigma \frac{\sqrt{[2B(E_L) + I_c(E_L)\eta_d f_\epsilon]\,\Delta E}}{\eta_d f_\epsilon \sqrt{A_t}\sqrt{T_{obs}}} \tag{1.21}$$

in which $A_u = f_\epsilon A_t$, and all other terms are as defined before.

1.2.3.2 Case of focusing telescopes

In the case of a focusing telescope, the signal S, noise N and signal to noise ratio $\frac{S}{N}$ are given by:

$$S = 0.76 I_L \eta_d f_\epsilon A_{eff} T_{obs} \tag{1.22}$$

$$N = \sqrt{I_C(E_L)\eta_d f_\epsilon A_u T_{obs}\Delta E + 2B(E_L)A_d T_{obs}\Delta E} \tag{1.23}$$

$$\frac{S}{N} = \frac{0.76 I_L \eta_d f_\epsilon A_{eff} T_{obs}}{\sqrt{I_C(E_L)\eta_d f_\epsilon A_u T_{obs}\Delta E + 2B(E_L)A_d T_{obs}\Delta E}} \tag{1.24}$$

Where A_{eff} is the effective area of the telescope, and all other terms have the same meaning as defined before. Similarly to the case of direct-viewing instruments, from the above expressions, we can get the minimum detectable intensity $I^{min}_{L_{ft}}$, (in photons s^{-1} cm^{-2}) at a confidence level corresponding to n_σ, of a line for a focusing instrument can be derived, and is given by:

$$I^{min}_{L_{ft}} = 1.31 n_\sigma \frac{\sqrt{[2B(E_L)A_d + I_c(E_L)\eta_d f_\epsilon A_{eff}]\,\Delta E}}{\eta_d f_\epsilon A_{eff}\sqrt{T_{obs}}} \tag{1.25}$$

1.2.4 Estimation of parameters for the sensitivity

The estimation of different parameters for obtaining the sensitivity is described in [24]. A brief description of these are given below.

Confidence level

This gives the statistical significance of the measurement. Usually for the sensitivity a confidence level of 99.7% is taken. For this Confidence level, the number of standard deviations is 3. In my estimates, the value of n_σ is taken as 3.

Efficiency of detector, η_d

This is the X-/Gamma-ray detection efficiency of the detector system. This is estimated by calculation (at low energies) or on the basis of Monte–Carlo simulations. A more simple way to calculate this term is using the mass absorption coefficient $\mu(E)$ for the detector at energy E and is given by:

$$\eta_d(E) = 1 - e^{-\mu x} \tag{1.26}$$

where x is the thickness (in cm) of the detector and the μ is the absorption coefficient (in cm^{-1}). Hence the term μx is a dimensionless quantity. The calculations that have been carried out throughout this work takes 90% as the efficiency of the detector.

Fraction of photons, f_ϵ

This term represents the fraction of photons that is incident on the detector area A_d and is obtained from the radial profile data. We have considered $f_\epsilon = 50\%$ for this work.

Area of detector, A_d

From the radial profile data, the radius corresponding to 50% of the enclosed photons is obtained (Half Power Radius). Then, for the case of a focusing instrument, the detector area A_d corresponds to the area estimated from this radius.

Effective area of the telescope, A_{eff}

The effective area at an energy E is defined as the product of the geometrical area of the optics times its reflection efficiency at the same energy E.

In the case of Laue lenses made of crystals, the effective area is the product of the geometric area of the crystals that reflect photons in a narrow energy interval ΔE around $E\left(E - \dfrac{\Delta E}{2} \leq E \leq E + \dfrac{\Delta E}{2}\right)$ times the mean reflection efficiency in this energy interval.

In our case, if the entire energy range (90-600 keV) of the lens is sub–divided into 10 equal bins (in logarithmic scale), the total geometric area in a given energy bin, GA^{bin}_{total}, is the total cross section of the crystals that reflect photons in the energy range of the bin.

If $N_c(\Delta E)$ is the number of crystal tiles that reflect photons in a given energy bin, and $xtal_{area}$ is the surface area ($dim[0] \times dim[1]$) of a single crystal tile, then,

$$GA^{bin}_{total} = N_c(\Delta E) \times xtal_{area} \tag{1.27}$$

The effective area $Area^{bin}_{eff}$, in a given energy bin is given by:

$$Area^{bin}_{eff} = GA^{bin}_{total} \times \overline{R_{bin}} \tag{1.28}$$

where $\overline{R_{bin}}$ is the mean reflectivity in that bin.

Background noise, $B(E)$

The background noise of an X–/ Gamma–ray observing satellite comes from the contribution of many complex processes.

- Cosmic diffuse X–/ Gamma–ray background contribution from aperture leakage:
  This contribution can be expressed (in units of $counts\ s^{-1}cm^{-2}keV^{-1}$) as:

$$B_{cd}(E) = \eta_d(E)\frac{dN(E)}{dE}\Omega$$

  where $\eta_d(E)$ is the efficiency of the detector and $\frac{dN(E)}{dE} = 87.4E^{-2.3}$, is the spectral shape of the isotropic cosmic diffuse emission. The aperture solid angle, Ω is the major factor affecting this background.

- Neutron–induced background contribution:
  Neutrons, which are produced throughout the material of the telescope and spacecraft, can interact within the detector to generate background noise events. This contribution depends directly upon the volume of the detector and also on the material of the detector element.

- Spallation–induced background contribution:
  Radioactive isotopes are generated when cosmic Ray Protons interact within the detector elements. The subsequent β–decay of these isotopes produces background counts within the detector system which are indistinguishable from true events. This contribution also depends upon the volume of the detector and also on the material of the detector element.

- Geomagnetic cut-off:
  Earth's magnetic field prevents cosmic rays below a cut-off rigidity from reaching Earth. And when the satellite revolves around Earth, this value causes the change in background intensity. The value of rigidity is different for High Earth Orbit (HEO) and Low Earth Orbit (LEO). If the orbit is equatorial then the rigidity is at a high value typically (11–15) GV. If the orbit is polar the rigidity cut-off varies from 1–15 GV, thus giving rise to variable background.

- Shield leakage background contribution:
  The spacecraft will be immersed in a sea of photons derived from the Cosmic Diffuse Background, Gamma–rays produced in the material of the spacecraft and also from the atmospheric albedo Gamma–rays. These contributions may be reduced by increasing the thickness of the anti-coincidence counter or the shield.

The total background noise may be taken to be the sum of all the above contributions. An extensive report on the background of X–/ Gamma–ray observing satellite has been given in [24]. Figure 1.2 shows the total background of the two main instruments (SPI and IBIS) on–board the INTEGRAL satellite along with a constant background, that

has been considered for calculating the sensitivity in this thesis. The value assumed is realisticconsidering the fact that a focal plane detector (small size) can be better shielded.

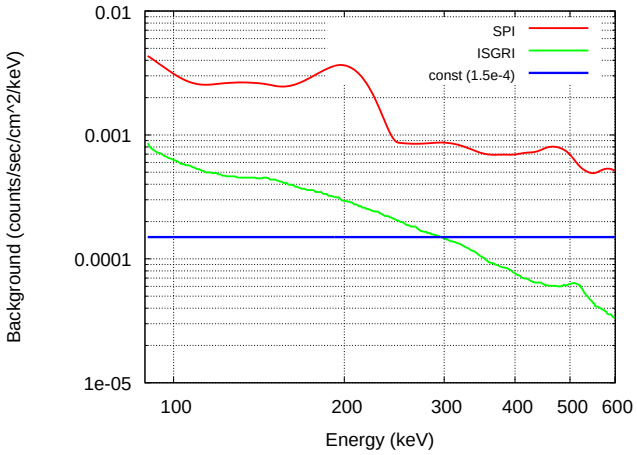

Figure 1.2: The different background data that have been considered in calculating the continuum sensitivity of the lens in this thesis.

Observation time, T_{obs}

The satellites placed in Low Earth Orbit (LEO) have an orbital period of approximately 90 minutes. But due to the periodic earth occultation, the maximum time that can be taken to continuously observe a target of interest is limited to 40 minutes. In case of spacecraft in High Earth Orbit (HEO), this time will be even longer. For calculating the sensitivity, I have used $T_{obs} = 10^5$ seconds throughout the thesis, unless otherwise mentioned.

Energy bandwidth, ΔE

In order to identify the physical processes taking place within a cosmic X-ray source, estimation of the shape of the emission spectrum of the astronomical object is important. For this estimation, at least 5 bands are required over the operational range of the telescope. That makes the minimum required value of ΔE to be $E/2$. In this thesis I have considered binning the total energy passband (90 – 600 keV) subdivided in 10 equal logarithmic intervals and also $\Delta E = E/2$.

1.3 Significant high–energy missions

Significant advances in science always occur when the state of the art in instrumentation improves dramatically. In this section, the most significant High– Energy (HE) astronom-

ical missions, launched until November 2013, are discussed. A summary of them are given in Tables 1.1 and 1.2.

Vela satellites

Launched initally with the aim of monitoring the terrestrial nuclear tests, these satellites captured extra terrestrial Gamma rays, hence commencing a new era in the field of astronomy [82]. Vela satellites were equipped with X-ray detectors, neutron and gamma-ray detectors. There were scintillation X-ray detectors (XC) aboard Vela 5A and its twin, Vela 5B. Two energy channels, 3–12 keV and 6–12 keV, were possible through electronic thresholds.

Uhuru (SAS–1)

Uhuru was the first dedicated mission for X–ray astronomy [46]. Launched in 1969, it was the first of the Small Astronomy Satellite (SAS) series. It consisted of 2 sets of proportional counters, which perfomed the first comprehensive all–sky survey for X-ray sources. The counters, placed back to back and having a sensitivity of more than 10% efficiency to X-ray photons, operated in the 2-20 keV range bandwidth.

In its 2 years and 3 months long life time, Uhuru had discovered many important celestial sources, which include Cen X-3, Vela X-1, Her X-1 and Cygnus X-1.

SAS–2

The second in the SAS series, was dedicated for the study of high energy Gamma ray astronomy [31]. The payload contained 32–level wire spark–chamber, with an effective area of 540 cm^2. SAS–2 had an energy bandwidth of 20 MeV – 1 GeV .

Some of the science highlights include the first detailed survey of the Gamma–ray sky, establish the high energy component of diffuse celestial radiation and also correlated the gamma-ray background with galactic structural features.

COS–B

Caravane Observational Satellite (COS)–B is entitled for providing the first complete map of the Galaxy in Gamma-rays [8]. It had two instruments on–board. The first one was Magnetic-core, wire-matrix, spark chamber gamma-ray detector, which operated in the 30 MeV–5 GeV energy band. The other instrument was a proportional counter, operating in a bandwidth of 2–12 keV.

COS–B is mainly credited for providing the Gamma-ray map of the Galaxy. This satellite also observed and studied gamma-ray pulsars and binary systems.

HEAO–1

This is the first satellite in the series of High Energy Astronomy Observatories (HEAO) [75]. There were four experiments onboard.

- The A1 experiment (Large Area Sky Survey). Using seven large proportional counters;
- The A2 experiment (Cosmic X-ray Experiment) included six proportional counters covering the band: 2.5-60 keV;
- The A3 experiment had Modulation Collimator (MC) working in the energy band 0.9-13.3 keV;
- The A4 experiment included seven inorganic phoswich scintillator detectors covering a total energy bandwidth from 15 keV – 10 MeV.

With this mission, for the first time a hard X-ray sky survey was performed. Some of the science highlights include measurement of X-ray background from 3-50 keV, complete flux-limited High Galactic Latitude Survey, monitoring the variability of a variety of objects from AGNs to X-ray binaries. HEAO–1 is credited with the discovery of first eclipse seen in a low-mass X-ray binary.

Einstein Observatory

The second satellite of the HEAO series, HEAO–2, is commonly known as Einstein observatory [45]. This was the first satellite with the capability of fully imaging X-ray sources. The Einstein Observatory had a single large Wolter Type–I grazing incidence focusing X-ray telescope, which is combined with different instruments in the focal plane to provide arc-second angular resolution of point sources and extended objects. The total bandwidth of Einstein Observatory is from 0.1 keV – 20 keV. The imaging capability is in the bandwidth from 0.1 keV – 4.0 keV using Imaging Proportional Counter (IPC) and High Resolution Imager (HRI) [0.15-3.0 keV]. The Monitor Proportional Counter (MPC) had an energy bandwidth of 1.5 - 20 keV.

The Einstein Observatory had almost 4 years of mission duration. In this period, it examined stellar atmospheres and supernova remnants, identified many X-ray double stars (some containing suspected Black holes candidates), and detected X-ray sources in other galaxies.

European X-ray Observatory Satellite (EXOSAT)

EXOSAT was the second satellite launched with the capability of imaging astronomical X–ray sources [23, 72, 89]. The total bandwidth of this satellite was from 0.05 keV – 50 keV. The imaging capability in the energy range 0.05 keV – 2 keV was provided by Wolter Type I grazing incidence telescope equipped with two low-energy imager (LEIT).

Unfortunately this instrument had problems in flight and the imager in the focal plane failed during the science verification phase. EXOSAT also included a Gas Scintillation (GS) Proportional Counter working in the bandwidth 2–20 keV. The third instrument was a Medium Energy (ME) Proportional Counter, which extended the energy band from 1 keV to 50 keV.

During the time of it's operation, EXOSAT has made about 1780 observations of a wide variety of objects. This includes active galactic nuclei, stellar coronae, cataclysmic variables, white dwarfs, X-ray binaries, clusters of galaxies, and supernova remnants.

ROSAT

Röntgensatellit (ROSAT) [2], was an X–ray satellite having a total energy bandwidth of 62 eV – 2.5 keV. It had four instruments on-board. The focusing X-ray Telescope (XRT) had a mirror assembly of grazing incidence four-fold nested Wolter I configuration. This was sensitive to X-rays between 0.1 to 2 keV. XRT had three focal plane instruments – two Position Sensitive Proportional Counters (PSPC) and one High Resolution Imager (HRI).

The lifespan of ROSAT was over eight years. In this period an X-ray all-sky survey catalogue of more than 150,000 objects were obtained. Other scientific studies include morphology of supernova remnants and clusters of galaxies, detection of shadowing of diffuse X-ray emission by molecular clouds, pulsations from *Geminga*, isolated neutron stars etc. ROSAT is also credited with the discovery of X-ray emission from comets.

Compton Gamma-Ray Observatory (CGRO)

CGRO was the first satellite having the capability to observe objects in an energy range of 6 orders of magnitude from 20 keV to 10 GeV. It had four payloads: The Burst and Transient Source Experiment (BATSE) (an all sky monitor: 20-1000 keV), the Oriented Scintillation Spectrometer Experiment (OSSE) (0.05-10 MeV energy range), the Compton Telescope (Comptel) (0.8-30 MeV) and the Energetic Gamma Ray Experiment Telescope (EGRET) (30 MeV-10 GeV).

The duration of CGRO life was over 9 years. The main scientific cases [61] credited with CGRO include the discovery of an isotropic distribution of the Gamma-ray burst events, mapping the Milky Way using the ^{26}Al Gamma-ray line, discovery of Blazar Active Galactic Nuclei as primary source of the highest energy cosmic Gamma-rays, discovery of the *Bursting Pulsar*.

ASCA

The Advanced Satellite for Cosmology and Astrophysics, ASCA, was the first Japanese satellite to use CCD detectors for X-ray astronomy [14]. There were four X-ray telescopes each composed of 120 nested gold-coated aluminum foil surfaces. On the focal plane of this

telescope, there were a Gas Imaging Spectrometer (GIS; 0.8-12 keV), two Imaging Gas Scintillation Proportional Counters (IGSPC), a Solid-state Imaging Spectrometer (SIS; 0.4-12 keV) and two CCD arrays of four 420 × 422 square pixel chips. These instruments provided a total observational energy range from 0.4–12 keV.

ASCA made 7 and half years of scientific observations [85], which include the discovery of broad Fe X-ray lines from AGN probing the strong gravity near the central engine, lower than solar Fe abundance in the coronae of active stars, spectroscopy of interacting binaries, non-thermal X-rays from SN 1006 (a site of Cosmic Ray acceleration), abundances of heavy elements in clusters of galaxies which were found consistent with type II supernova origin.

Rossi X-ray Timing Explorer (RXTE)

The 'Rossi' X-ray Timing Explorer (RXTE) is a satellite that was dedicated to the observation of the timing properties of celestial X-ray sources in a broad energy band from 2–250 keV [83]. There were three instruments on-board RXTE. The All–Sky Monitor(ASM) was equipped with proportional counters with an energy range from 2-12 keV. The Proportional Counter Array (PCA) was an array of five proportional counters, with 2-60 keV energy range. The High Energy X-ray Timing Experiment (HEXTE), which had an energy band of 15-250 keV, consisted of two clusters each containing four phoswich scintillation detectors.

RXTE has performed key important observations of the time variability from black holes, neutron stars, X-ray pulsars and X-ray bursts. This mission along with BeppoSAX, have opened a new era in the study of the celestial sources, that of the broad band observations.

Beppo SAX

The SAX (Satellite per Astronomia X) satellite is the first X-ray mission with a scientific payload covering more than three decades of energy - from 0.1 to 700 keV [76]. BeppoSAX contained five science instruments:

– Low Energy Concentrator Spectrometer (LECS): 0.1-10 keV, with a low energy Gas Scintillator Proportional Counter (GSPC) in the telescope focus;

– Medium Energy Concentrator Spectrometer (MECS): 1.3-10 keV, with three telescopes and three identical GSPCs in the focus of the telescope;

– A High Pressure Gas Scintillation Proportional Counter (HPGSPC): 4-120 keV;

– A Phoswich Detector System (PDS): 15-200 keV [35];

– Two Wide Field Cameras (WFC): 2 proportional counters with coded masks operating in the 2 to 30 keV range;

– A Gamma Ray Burst Monitor: 40-700 keV, with 4 CsI(Na) scintillator detector units.

BeppoSAX was the first satellite that discovered the X–ray afterglow emission from Gamma Ray Bursts (GRB) [18]. From its capability to promptly and accurately locate

GRBs, and from this discovery, it was possible in 1997 1997 to solve the mystery of the origin of GRBs. Now we know that they are at cosmological distances.

BeppoSAX was also capable of monitoring large regions of the sky with a resolution of 5' in the range 2-30 keV to study long term variability of sources, and to perform accurate broad band spectral studies of galactic and extra galactic sources [18]. Figure 1.3 shows the X–ray afterglow of the GRB 970228.

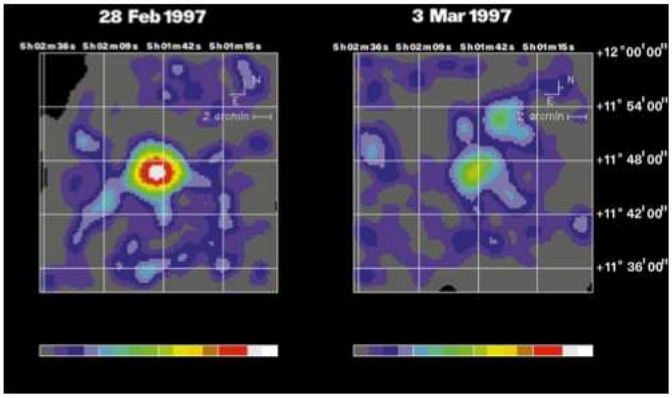

Figure 1.3: False-colour images of the source SAX J0501+1146, as detected in the error box of GRB970228 with Beppo-SAX Medium Energy Concentrator Spectrometer (2-10keV) during the first and second Target of Opportunity observations [18].

Chandra X-ray Observatory

Chandra is considered to be one of the Great Observatories still in orbit. It was earlier known as AXAF, the Advanced X-ray Astrophysics Facility [100]. It consists of a single Wolter Type 1 grazing incidence iridium-coated imaging telescope. On the focal plane, lies an Advanced CCD Imaging Spectrometer (ACIS) (0.2–10 keV) and a High Resolution Camera (HRC). ACIS consists of 10 CCD chips and provides images as well as spectral information of the observed object. HRC has two micro-channel plate components and gets images over the range of 0.1–10 keV. The High Energy Transmission Grating Spectrometer (HETGS) works over 0.4–10 keV and has a spectral resolution of 60–1000. The Low Energy Transmission Grating Spectrometer (LETGS) has a range of 0.09–3 keV and a resolution of 40–2000 [102].

The field of X-ray astronomy has greatly advanced thanks to Chandra. It has made a number of images of many objects in the X–ray energy band with unprecedented energy resolution (2“). The images include supernova remnants, galaxies, the Crab nebula, X–ray afterglow of GRBs, etc.

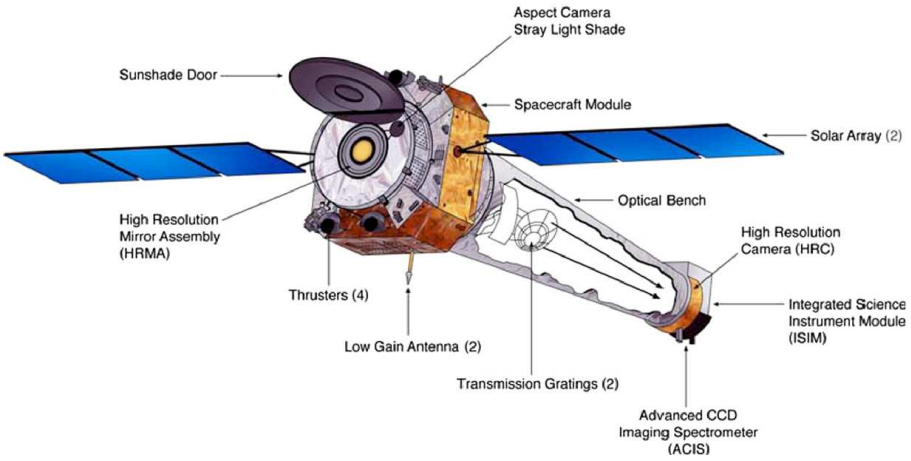

Figure 1.4: Annotated illustration of CXO. [101]

XMM–Newton

The X-ray Multi-Mirror Mission - Newton [4], was originally known as the High Throughput X-ray Spectroscopy Mission. It consists of three co-aligned Wolter Type I grazing incidence gold-coated imaging X-ray telescopes, each with 58 nested reflectors. On the focal plane there are three European Photon Imaging Cameras (EPIC). XMM–Newton has an energy range from 0.1–15 keV. This mission is providing the most accurate spectra so far obtained in this passband. While Chandra is the best mission so far for imaging, XMM-Newton is the best mission for spectroscopy in 0.1–10 keV.

INTEGRAL

The INTErnational Gamma-Ray Astrophysics Laboratory (INTEGRAL) [78], is a dedicated mission to study high energy phenomenons in the Universe. There are three payloads in this satellite, including two Gamma ray instruments.

- Imager on-Board the INTEGRAL Satellite (IBIS):
  The energy range of this instrument is from 15 keV (hard X-rays) to 10 MeV (Gamma rays). The main features of IBIS can be found in [71] and in the IBIS observers manual [15]. IBIS is composed of two direct–view detectors (one behind the other) surrounded by a coded mask plus a collimator. The first detector behind the mask is the Integral Soft Gamma–Ray Imager (ISGRI). ISGRI is composed of 16384 Cadmium–Telluride (CdTe) solid–state detectors with a cross section of 4×4 mm^2 and a thickness of 2 mm. ISGRI has an active area of 2621 cm^2. Behind ISGRI is located another detector, the PIxellated Cesium–Iodide Telescope (PICsIT), composed of 4096 Cesium–Iodide (CsI) scintillator crystals with a cross section of 9×9 mm^2 and a thickness of 30 mm. PICsIT has an active area of 2994

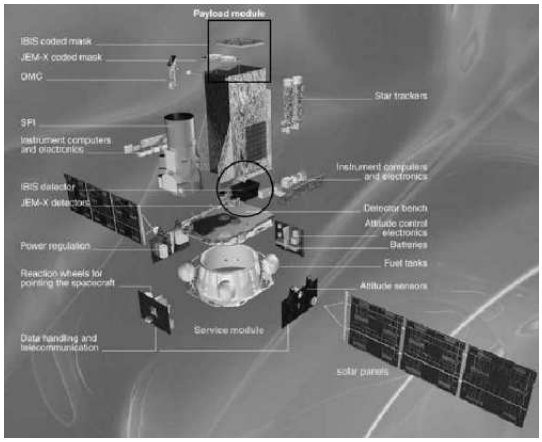

Figure 1.5: This figure shows the IBIS coded mask (in the *square*) and the IBIS detector (in the *circle*) [71].

cm^2 and covers the energy band from 175 keV up to 10 MeV.

- SPectrometer for INTEGRAL (SPI):
  SPI [29] has, in the detector plane, 19 germanium crystals positioned hexagonally, which provides an energy resolution of 2 keV at 1 MeV. Above this there is a coded mask of tungsten tiles, which also has an hexagonal structure. The operational bandwidth of energy is from 20 keV to 8 MeV.
- The Joint European X-ray Monitor (JEM-X):
  This instrument operates in the energy range 3–35 keV. It consists of a high pressure gas chamber surrounded by a coded aperture mask [65].

INTEGRAL is performing a sky survey at hard X-ray energies iin addition to the study of peculiar X-ray sources. With INTEGRAL, the space distribution of the 511 keV annihilation line has been measured for the first time.

Swift

Swift is the first satellite dedicated to the Gamma Ray Burst science [42, 41]. It has three instruments on-board. Burst Alert Telescope (BAT) (energy range: 15–150 keV) is responsible for detecting the gamma ray bursts and then promptly locate their position coordinates, which are then send to the ground–based telescopes for further observations. BAT is composed of a coded aperture mask combined with a CdZnTe detector.

The X-ray Telescope (XRT) (energy range of 0.2 – 10 keV) uses a Wolter Type I X-ray telescope with 12 nested mirrors. There is a Metal Oxide Silicon (MOS) charge-coupled device (CCD) at the focal plane of the mirrors. XRT gives more precise coordinates of

the GRB (error within 2 arcseconds radius). Using the CCD, this telescope can perform imaging as well as spectral analysis of the afterglow.

NuSTAR

The Nuclear Spectroscopic Telescope Array (NuSTAR) (see Fig. 1.6) is the last launched X-ray mission (June 2012). It has onboard a focusing telescope which pushed the limits of the focusing optics beyond 10–12 keV to 79 keV [53]. The high effective area of NuSTAR (see Fig. 1.7, *left*) is well suited (see its sensitivity in Fig. 1.7, *right*) for studying objects such as black holes, supernovae, and extremely active galaxies.

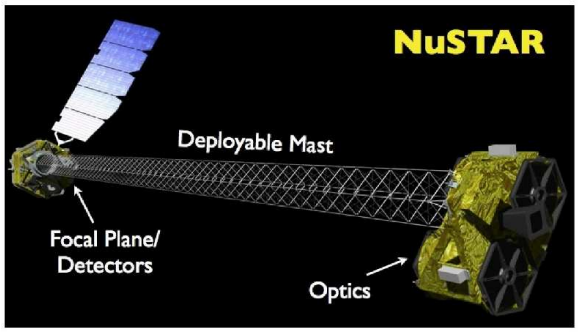

Figure 1.6: The deployable mast, which firmly positions detectors in the focal plane of the optics.

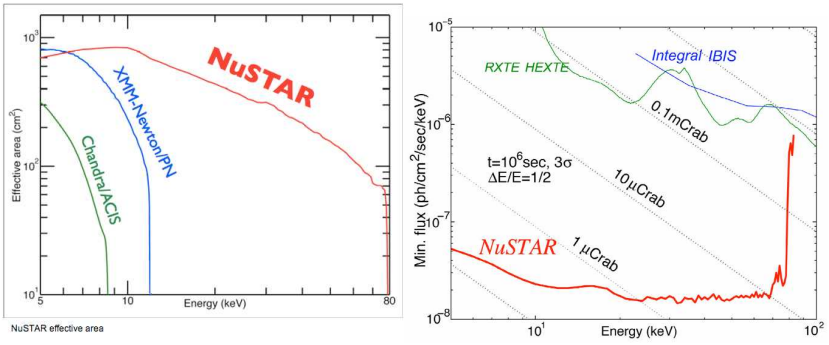

Figure 1.7: *Left*: NuSTAR efective area compared with the currently active X–ray instruments [53]. *Right*: The sensitivity of different instruments with respect to that of NuSTAR. *Credit: Daniel Stern (JPL / Caltech)*

The focusing optics consists of 133 concentric Wolter type I (with conical approximation) grazing incidence shells (see Fig. 1.9). These shells are coated with alternating

atomically thin layers of a high-density and low-density material, enabling reflectivity up to 79 keV. The inner shells (89) of *NuSTAR*are coated with alternating atomically thin layers of Pt and SiC materials, while the outer 44 shells are coated with W and Si [53].

Four 32 × 32 pixel Cadmium-Zinc-Tellurium (CdZnTe) detectors, surrounded by a CsI anti- coincidence shield are positioned on the focal plane, at a distance of 10 meters from the optics. The Optics and the detectors are held in position by a deployable mast (see Figure 1.6).

A significant part of the *NuSTAR* core program time will be devoted to sensitive studies of extragalactic and Galactic surveys, which will supplement the extended surveys beyond 20 keV already performed [9, 19] or planned to be continued with the ESA INTEGRAL observatory [103], and with the NASA *Swift* satellite [42].

Table 1.1: Significant High–energy missions launched between 1969 and 1995.

Satellite	**Duration**	**On–board HE Instrument(s)**	**Energy range**
Vela Satellites (5A, 5B)	May 1969 – June 1979	Scintillation X-ray detector All-Sky Monitor (ASM)	3-12 keV
		Gamma Ray detectors	150-750 keV
Uhuru (SAS 1)	Dec. 1970 – March 1973	Two sets of proportional counters all sky survey	2-20 keV
Small Astronomy Satellite (SAS)– 2	Nov. 1972 – June 1973	32-level wire spark-chamber	20 MeV - 1 GeV
COS-B	Aug 1975 – April 1982	proportional counter	2-12 keV
		Magnetic-core, wire-matrix, spark chamber Gamma Ray detectors	30 MeV-5 GeV
HEAO-1	Aug. 1977 – Jan. 1979	proportional counter	0.15-60 keV
		Modulation Collimator (MC)	0.9-13.3 keV
		scintillator detectors	15 keV-10 MeV
Einstein Observatory (HEAO-2)	Nov. 1978 – April 1982	Imaging Proportional Counter (IPC) Wolter Type I grazing incidence telescope	0.1-4 keV
		High Resolution Imager (HRI)	0.15-3.0 keV
		Monitor Proportional Counter (MPC)	1.5 - 20 keV
EXOSAT	May 26, 1983 – April 9, 1986	Wolter Type I grazing incidence	0.05-2 keV
		Gas Scintillation (GS) Proportional Counter	2-20 keV
		Medium Energy (ME) Proportional Counter	1-50keV
ROSAT	1 June 1990 - Feb. 1999	Wide Field Camera with its own mirror system	62-206 eV
		Proportional Counter and High Resolution Imager (HRI)	0.1-2.5 keV
Compton Gamma-Ray Observatory (CGRO)	5 April 1991 – June 2000	Burst and Transient Source Experiment (BATSE)	20-1000 keV
		Oriented Scintillation Spectrometer Experiment (OSSE)	0.05-10 MeV
		Compton Telescope (Comptel)	0.8-30 MeV
		Energetic Gamma Ray Experiment Telescope (EGRET)	30 MeV-10 GeV
ASCA	Feb. 20, 1993 – June 1979	120 nested gold-coated aluminium foil surfaces	0.4 - 12 keV
Rossi X-ray Timing Explorer	Dec. 1995 - Jan. 2012	All-Sky Monitor (ASM)	2-10 keV
		Proportional Counter Array (PCA)	2-60 keV
		High Energy X-ray Timing Experiment (HEXTE)	15-250 keV

Table 1.2: Significant High–energy missions launched between 1995 and November 2013.

Satellite	Duration	On–board HE Instrument(s)	Energy range
BeppoSAX	30 April 1996 – April 2002	Low Energy Concentrator Spectrometer (LECS)	0.1-10 keV
		Medium Energy Concentrator Spectrometer (MECS)	1.3-10 keV
		High pressure Gas Scintillator Proportional Counter (HPGSPC)	4-120 keV
		Phoswich Detection System (PDS)	15-200 keV
		Wide Field Camera	2-30 keV
		Gamma Ray Burst Monitor	40-700 keV
Chandra X-ray Observatory (AXAF)	23 July 1999 -	A single Wolter Type 1 grazing incidence iridium-coated imaging telescope	0.1-10 keV
XMM – Newton	Dec. 1999 –	Three co-aligned Wolter Type I grazing incidence gold-coated imaging X-ray telescopes	0.1-15 keV
INTEGRAL	Oct. 2002 –	SPectrometer on INTEGRAL: SPI	18 keV - 8 MeV
		Imager on Board the INTEGRAL Satellite: IBIS (coded-aperture)	15 keV - 10 MeV
		Joint European X-ray Monitor: JEM-X	3 - 35 keV
Swift	Nov. 2004 –	Burst Alert Telescope (BAT) coded aperture mask	15-150 keV
		X-ray telescope (XRT)	0.3 - 10 keV
NuSTAR	June 13, 2012	two co-aligned grazing incidence telescopes. 10-meter focal length.	6 - 79 keV

1.4 Hard X–ray focusing technique

'Einstein', EXOSAT, ROSAT, ASCA, Chandra, BeppoSAX, XMM–Newton and Swift employed total external reflection technique for focusing X–rays. Chandra mirrors are able to focus up to 10 keV photons. By employing a different technique known as supermirror optics, NuSTAR has extended this limit to 79 keV by changing the coating material over the co–aligned grazing incidence shells. The other techniques of focusing hard X–/soft Gamma–rays is by the diffracting optics in Laue configuration. In this case it is possible to extend the energy range of focusing photons beyond 80 keV, with a very good sensitivity.

1.4.1 Total reflection optics

This method has been largely employed for focusing photons up to 10 keV. When the grazing incidence angle is lower than a critical angle θ_c, the materials with a high atomic number, are very good X–ray reflectors. This is possible because the real part of the refraction index for X–rays, (n_r) in the material, is lower than that in vacuum $(n_r = 1-\delta)$. It can be shown that the critical angle θ_c, is given by:

$$\theta_c = \sqrt{2\delta} \tag{1.29}$$

In order to minimise the coma aberrations and to decrease the optics focal length, special geometrical configurations like that of Wolter I mirror configuration, are adopted. Wolter I mirror geometry is formed by two coaxial and confocal mirrors, one with the shape of a paraboloid and the other with the shape of a hyperboloid (see Figure 1.8).

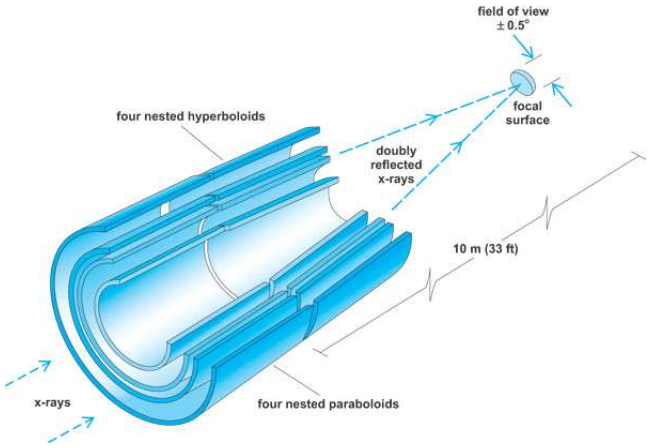

Figure 1.8: The nested mirror configuration showing the Wolter I geometry. *Image courtesy of Raytheon Optical Systems.*

The coating on these mirrors and the focal length decides the limit of energy band that can be focused for a fixed dimension of Wolter I configuration. In the case of Chandra,

the mirrors were Iridium coated The focal length was of 10 meters and its high energy threshold is 10 keV.

In order to extend the maximum energy limit of the photons that can be focused, and thus a better sensitivity than the direct-viewing telescopes, new technologies have to be adopted.

1.4.2 Supermirrors

The supermirrors [55] are composed of piled–up bi–layers with graded spacing (*multilayers*). NuSTAR, even with the same focal length as Chandra, is able to focus the photons upto an energy of 79 keV due to the type of coating over the mirrors. (see Section 1.3). Each bi–layer is composed of a high density diffracting layer, that behaves like a diffracting Bragg plane, and a low density layer that behaves as a spacer.

Figure 1.9 shows one of the two optical units onboard NuSTAR, which is made of 133 nested mirrors in order to focus X–rays in the energy range from 3 keV to 79 keV.

Figure 1.9: The image showing 133 nested cylindrical mirror shells of one of the two optical units onboard NuSTAR.

The X–ray reflection occurs at each interface of a high Z material. Constructive interferences can be produced when waves get scattered by different interfaces. This is achieved by efficiently selecting the by-layer thickness profile.

For going beyond 80–100 keV range, a much more challenging technique is required.

1.4.3 Diffracting optics

A diffracting optics exploit the principle of Bragg diffraction [11, 12] with crystals to focus hard X–rays and soft Gamma–rays [33]. When crystals are arranged properly, it can focus incoming photons to a point, which is just like the focusing of visible light by an optical lens. Laue lenses work on this principle, with the crystals being arranged such that the photons are deviated in the transmission geometry of the crystals.

A Laue lens with narrow energy passband has been already built and its functionality has been demonstrated in a balloon flight experiment as part of the CLAIRE project [52].

As I will demonstrate in this thesis, the Laue lenses appear to be the best solution to efficiently focus high energy X–rays (>80–100 keV).

1.4.3.1 CLAIRE project

CLAIRE project was a development project for a proposed satellite mission called MAX [96]. CLAIRE was the first R&D balloon experiment to demonstrate that a prototype Laue lens can work under space conditions, measuring its performance by observing an astrophysical target.

CLAIRE's narrow passband lens consisted of 556 crystals mounted on eight rings of a 45 cm diameter Titanium frame. The Germanium–rich $Ge_{1-x}Si_x$ crystals (x $\approx$ 0.02) were arranged such that they concentrated photons of energy 170 keV onto a focal spot of 1.5 cm diameter, at a distance of 279 cm behind the lens. The diffracted energy bandwidth was 3 keV around 170 keV, with a field of view of about 1.5 arcmin. At the focal plane there was a Gamma–ray detector made of 3 $\times$3 HPGe (High Purity Germanium) matrix cooled by liquid nitrogen.

CLAIRE was made to point towards the Crab Nebula for 72 minutes. Within this time, it collected 33 photons. This experiment validated the theoretical model of a Laue lens in space environment.

1.5 Purpose of the Thesis

In this thesis I will study the feasibility of a broad energy band ($> 80 - 600$ keV) focusing lens for astrophysical applications. To do that, I have been involved in two projects, HAXTEL and LAUE, supported by the Italian Space Agency ASI: the first in an advanced stage, the second just starting. Both are based on Bragg diffraction in Laue configuration. The first one with flat mosaic crystals, the second one through the development of curved crystals.

The need of focusing telescopes to overcome the sensitivity limits of the current generation of instruments is discussed in Chapter 1, along with a review of the most relevant missions already flown or still operational.

Figure 1.10: The CLAIRE telescope at the Gap–Tallard balloon base during the 2001 balloon campaign. On the first platform, the gamma-ray lens in its two-axes gimbal. [34]

The principle of Bragg diffraction in Laue configuration by curved crystals is exploited for focusing the incoming photons. Hence, a brief introduction about the diffraction theory of X–rays by the crystals is discussed in Chapter 2. The concept of Laue lens is also introduced in the later section of the same chapter.

Concerning HAXTEL, I was involved in the development of a second prototype of a Laue lens. The assembling and testing of mosaic Cu(111) crystals tiles in a ring configuration with the technique approached in HAXTEL, is elaborated in Chapter 3.

With the experience gained from the HAXTEL project, the introduction of a new assembling technology and the use of bent crystals are justified and the LAUE project is motivated. Within the LAUE projects, a new gamma-ray facility is required and a lens petal is among the project goals. I worked on the design of the petal structure, along with the simulation of on–axis PSF of the petal, in the energy band of 90–300 keV. All that is explained in the 4 Chapter.

In Chapter 5, I am discussing about simulation of the lens made with curved crystals. The on–axis performances of this lens along with various lens parameters like effective area, continuum and line sensitivity are also simulated and explained.

Finally in Chapter 6, I discuss about some of the open astronomical cases that can be settled by using the Laue lens configurations I have designed.

Chapter 2

Laue lens concept

Laue lenses principle exploit the interference between the periodic nature of the electromagnetic radiation and the periodic configuration of the atoms in a crystal. In a Laue lens, photons pass through the full crystal, using its entire volume for interacting coherently. In this chapter, the concept of Laue lens is being described, starting from the X–ray diffraction theory.

2.1 X–ray diffraction: an overview

Geometrical properties of the direct and the reciprocal lattice vectors of a crystal, define it's diffraction properties. In other words, if a crystal is having a periodic structure, it can act as a natural diffraction material for X–rays. Hence the incident waves are reflected by the parallel planes of the atoms in a crystal.

Two diffraction geometries are possible: the Bragg and Laue geometry. In the Laue or transmission geometry the incident beam enters from one side of the plate into the crystal, crosses the crystal where it can be partially absorbed and/or diffracted, and then emerges, together with the diffracted beam, from the opposite side. Whereas in the Bragg or reflection geometry, the incident beam enters the crystal where it can be diffracted and absorbed, but the diffracted beam emerges from the same side of the incident beam. Figure 2.1 illustrates this phenomenon in both reflection and transmission geometry.

The lattice periodicity of a crystal is only of few Armstrongs, a length comparable with the X–ray wavelengths. The first scientist who demonstrated that a crystal behaves like a diffraction grating for X–rays, was Max Von Laue. William Henry Bragg and his son designed new experiments [11, 12] and worked out crystal models that improved the knowledge of both X–rays and crystal structure.

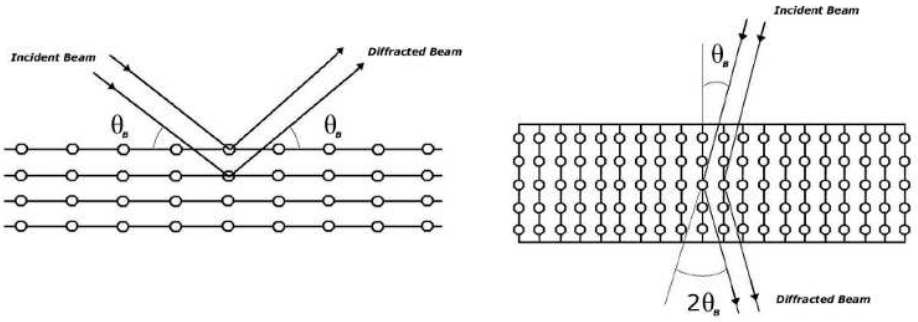

Figure 2.1: The Bragg condition for constructive interference of a gamma-ray photon beam with the atoms of a given crystalline plane. *Left panel*: Bragg diffraction in reflection configuration (Bragg geometry). *Right panel*: Bragg diffraction in transmission configuration (Laue geometry). [34]

2.1.1 The basic model

The set of all the periodic points identified by linear combinations of the principal vectors with integer coefficients are called the direct lattice or simply the lattice. The lattice is a mathematical construction that extends in an infinite three-dimensional space. The Fourier transform of the direct lattice is called the reciprocal lattice.

The X–rays scattered by different atoms in a crystal make different optical paths to reach a point in the space, where they can interfere. The phenomenon of diffraction takes place if this interference is constructive. For this to happen, the optical path difference should be an integer multiple of wavelength. This condition is expressed by Max Von Laue [97, 98] as:

$$\mathbf{k}_o - \mathbf{k}_d = \mathbf{g} \tag{2.1}$$

where $\mathbf{k}_o$ and $\mathbf{k}_d$ are the wave vectors of the incident and diffracted beams and $\mathbf{g}$ is a reciprocal lattice vector. An equivalent equation was given by Bragg [11, 12] as:

$$n\lambda = 2d_{hkl} \sin\theta_B \tag{2.2}$$

where, d_{hkl} is the distance between the lattice planes with Miller indexes hkl, θ_B is the scattering angle for diffraction (the Bragg angle), n is the diffraction order and λ is the wavelength of the photon. The energy E of the photon is related to it's wavelength λ by the relation:

$$E = \frac{hc}{\lambda} \tag{2.3}$$

where, $hc \approx 12.4$ keV-$\mathring{A}$. The Bragg angle θ_B is half the angle between the two wave

vectors $\mathbf{k}_o$ and $\mathbf{k}_d$. $\frac{2\pi}{d_{hkl}}$ is the magnitude of the modulus of the reciprocal lattice vector $\mathbf{g}$, which is also perpendicular to the planes. Thus the two equations, 2.1 and 2.2 are equivalent to each other.

The structure factor

The structure factor gives the efficiency of scattering of a unit cell. A unit cell is used to describe the arrangement of atoms within a crystal [3]. The structure factor, F_{hkl} is given by:

$$F_{hkl} = \sum_i f_i e^{2\pi i \mathbf{k}_o.\mathbf{r}_i} \tag{2.4}$$

where, f_i is the atomic scattering factor of the i^{th} atom of the cell, $\mathbf{k}_o$ is the incident wave–vector, and $\mathbf{r}_i$ is the position of the i^{th} atom with respect to the unit cell origin. The atomic scattering factor is the amplitude of a wave scattered by an atom divided by the amplitude of the wave scattered by an electron.

The intensity profile of the diffracted radiation

Distribution of the photons around the direction of scattering is given by the intensity profile. Knowledge of the scattering contributions from all the cells involved, is required for its calculation. Assuming a parallelepiped shape for the crystal, a good approximation of the profile can be obtained. Let $N_1\mathbf{a}_1$, $N_2\mathbf{a}_2$ and $N_3\mathbf{a}_3$ be the vectors representing the edge of this parallelepiped structure. ($\mathbf{a}_i$ are the principal vectors, while N_i is the number of cells lying on the i^{th} edge). Using this vectorial definition, the expression for diffracted beam $I_d\hat{\mathbf{k}}_d$, in the direction of the unit vector, $\hat{\mathbf{k}}_d$ is given by [105] as

$$\frac{I_d\hat{\mathbf{k}}_d}{I_o} = |F_{hkl}| \prod_{i=1}^{3} \frac{\sin^2\left[\frac{1}{2}N_i(\mathbf{k}_d - \mathbf{k}_o).\mathbf{a}_i\right]}{\sin^2\left[\frac{1}{2}(\mathbf{k}_d - \mathbf{k}_o).\mathbf{a}_i\right]}\ \hat{\mathbf{k}}_d \tag{2.5}$$

where, I_o is the intensity of the incident beam.

When equation 2.1 is satisfied, the diffracted intensity becomes maximum, which is then given by:

$$I_d = I_o|F_{hkl}|^2N^2 \tag{2.6}$$

where, $N = \prod_{i=1}^{3} N_i$ is the total number of cells of the crystal.

The absorption effect

What has been described before is valid for the ideal case of non-absorbing crystals. In the real case the absorption due to photoelectric and Compton scattering occur [3]. The absorption phenomenon results in a deviation of the photons from the direct beam which is

incoherent and depends only on material and the amount of matter crossed by the beam and not on its spatial arrangement. The "absorption" encountered due to the spatial arrangement is termed as extinction effect.

The fractional amount of intensity that passes from one beam to the other when the beams cross an infinitesimal layer of thickness, dT is expressed by the extinction coefficient σ, while the other lost fraction depends on the normal absorption coefficient per unit of length, μ.

Diffracted radiation power

The power, P_{hkl} of the diffracted radiation is obtained by integrating equation 2.5 over the cross section S. Mostly, in the experimental environments, polychromatic beam is used instead of monochromatic. Thus for obtaining the integrated intensity, I^p_{hkl} for a polychromatic beam, P_{hkl} has to be further integrated over the three coordinates of the vector δ

$$I^p_{hkl} = \int_{\delta} P_{hkl} d\delta = \int_{S,\delta} I_{hkl} ds d\delta \tag{2.7}$$

Integrated Reflectivity

Integrated reflectivity, $R_{hkl}(E)$ is the ratio of the total power reflected towards a certain direction, $P_{hkl}(E,\theta)$ and the incident power $P_0(E)$. θ is defined in the range $[\theta_{min}{:}\theta_{max}]$, where the value of $P_{hkl}(E,\theta)$ is significantly different from zero. Hence, Integrated reflectivity is the result of integration over the angular variable and is normalised to the incident power. $R_{hkl}(E)$ is given by:

$$R_{hkl}(E) = \int_{\theta_{min}}^{\theta_{max}} \frac{P_{hkl}(E,\theta)}{P_0(E)} d\theta \tag{2.8}$$

2.2 Types of crystals

Any defect in the lattice structure can deviate from the theoretical model of diffraction stated in the above sections. Hence the reflectivity is different for different types of crystals. The modelling has to be further narrowed down to the kind of lattice defect a crystal may posses.

2.2.1 Mosaic crystals

According to the model proposed by C. G. Darwin [21, 22], mosaic crystals are considered to be crystals composed of small blocks, called crystallites with a size approximately varying from 1 to 100 μm. These crystallites are assumed to be perfect. The lattice orientation of these crystallites are distributed around a main direction. In perfect crystals,

all the crystallites are assumed to be oriented along a given direction. Figure 2.2 shows the microscopic view of a mosaic crystal, showing the small crystallites.

Figure 2.2: Microscopic image of the mosaic crystal, showing the crystallites. Reprinted from [77]

A Gaussian distribution is used to describe the misalignment of the crystallites around the main direction:

$$W(\Delta) = \frac{1}{\sqrt{2\pi}\eta} e^{-\frac{\Delta^2}{2\eta^2}} \tag{2.9}$$

where Δ is the magnitude of the angular deviation from the mean and η is the standard deviation, which, physically gives the extent to which the lattice planes are misaligned with respect to the mean direction of the planes. The degree of the misalignment of the lattice planes is given by the Full Width Half Maximum (FWHM), of the Gaussian function. This quantity is called *mosaicity* or *mosaic spread* β_m of the crystal, and is given by:

$$\beta_m = 2\sqrt{2\ln 2}\eta \approx 2.35\eta \tag{2.10}$$

The two beams, transmitted and diffracted, make up a coupled dissipative system, in which one beam can transfer a fraction of its intensity to the other, because of diffraction, or it can fade because of normal absorption.

The fractional amount of intensity that is absorbed before arriving to an infinitesimal layer of thickness dT , gives secondary extinction. This extinction is equal to the sum of the ordinary absorption plus the reflection of all the crystal blocks of thickness dT, oriented in a similar way like that under consideration. In mosaic crystals, there are indeed two kinds of extinctions. Primary and secondary. The *primary extinction* is a phenomenon which refers to the photons that pass from the direct to the diffracted beam in a crystallite of thickness dT.

The effective absorption coefficient is given by:

$$\mu_\epsilon = \mu + \sigma\gamma_0 \tag{2.11}$$

where μ is the normal absorption coefficient per unit of length and $\gamma_0 = \cos\theta_0$, θ_0 being the angle between direction of the photons normal to the crystal surface. σ is the secondary extinction coefficient, which is given by:

$$\sigma(\Delta, E) = W(\Delta)Q(E)f(A) \tag{2.12}$$

where,

$$Q(E) = r_e^2 \left| \frac{F_{hkl}}{V} \right|^2 \lambda^3 \frac{1 + \cos^2(2\theta_B)}{2\sin(2\theta_B)} \tag{2.13}$$

in which r_e is the classical electron radius ($2.82 \times 10^{-5} \mathring{A}$), F_{hkl} is the structure factor, inclusive of the temperature effect (Debye–Waller's factor), V is the volume of the crystal unit cell, λ is the radiation wavelength and θ_B is the Bragg angle for that particular energy.

The function $f(A)$ in equation 2.12 is given by:

$$f(A) = \frac{B_0(2A) + |\cos 2\theta_B| B_0(2A|\cos(2\theta_B)|)}{2A(1 + \cos^2\theta_B)} \tag{2.14}$$

where, B_0 is the zero order Bessel function integrated between 0 and $2A$, in which A is given by:

$$A = \frac{\pi t_0}{\Lambda_0 \cos\theta_B} \tag{2.15}$$

Here, t_0 represents the crystallite thickness and Λ_0 is the extinction length. For symmetrical Laue case, i.e. the case where the mean lattice plane is normal to the surface of the crystals, Λ_0 is given by.

$$\Lambda_0 = \frac{\pi V \cos\theta_B}{r_e \lambda |F_{hkl}| (1 + \cos 2\theta_B)} \tag{2.16}$$

The integrated reflectivity (Equation 2.8) can be given in terms of secondary extinction coefficient and absorption coefficient as:

$$R_{hkl}(\Delta, E) = \sinh(\sigma T) \exp\left[-(\mu + \sigma\cos\theta_0) \frac{T}{\cos\theta_0} \right] \tag{2.17}$$

$$= \frac{1}{2}\left(1 - e^{-2\sigma T}\right) e^{-\mu \frac{T}{\cos\theta_0}} \tag{2.18}$$

where, θ_0 is the angle between the direction of the photons and the normal to the crystal surface, T is the thickness of the mosaic crystal and μ is the absorption coefficient corresponding to that particular energy. The factor $\frac{T}{\cos\theta_0}$ gives the distance travelled by the direct beam inside the crystal.

When the crystal has zero absorption ($\mu = 0$) and the extinction coefficient is infinity ($\sigma = \infty$), $R_{hkl}(\Delta, E)$ becomes 1/2. This shows that the maximum power that can be reflected by a mosaic crystal is half of that of the power of incident beam. i.e. the diffraction efficiency of mosaic crystals is 50%.

2.2.2 Curved crystals

There are many ways of curving a crystal. Most the methods used have been described in [7, 13, 16, 49, 68]. Curving a crystal changes the angular distribution of the incoming beam at the entrance surface and it also deforms the regular atomic spacing inside the crystal. Section 4.1 in Chapter 4 provides a description about the bent mosaic crystal (Figure 4.2) and bent perfect crystals (Figure 4.1).

The diffraction profile of a bent crystal is different from that of a perfect crystal. When a crystal is bent, the standard dynamical theory related to the perfect crystal cannot be applied. The reflectivity of such bent crystals can be simulated by using many methods, but each method has its own limitations. Some of the methods are described below.

2.2.2.1 Multi Lamellar Method

In this method, the crystal is supposed to be consisting of several layers of thin perfect crystal tiles. Each of these layers are assumed to be misaligned in such a way that they follow the curvature of the entire crystal. The dynamical theory of plane crystals, as described by Zachariasen [105], can be used to calculate the reflected and transmitted rays because each layer is assumed to be perfect and thin.

A detailed description of the method used for calculating the crystal reflectivity was given by Boeuf et al. [10] in the case of X-ray diffraction in reflection configuration, and by Sanchez del Rio [25] in reflection and transmission configuration of the crystals.

2.2.2.2 Takagi-Taupin (TT) Equations

Using TT equations [84, 86], the behavior of the electromagnetic field inside the crystal is described. Following Sanchez del Rio et. al. [25], these equations are given by:

$$\frac{\partial}{\partial s_0} D_0(\vec{r}) = -i\pi k P \Psi_H D_h(\vec{r}) \tag{2.19}$$

$$\frac{\partial}{\partial s_h} D_h(\vec{r}) = -i\pi k P \Psi_H D_0(\vec{r}) + 2\pi i \left\{ k\beta_h - \frac{\partial}{\partial s_h}\left(\vec{h}.\vec{u}(\vec{r})\right)\right\} \tag{2.20}$$

where D_0 and D_h respectively are the amplitudes of the transmitted and diffracted fields, $\hat{k}$ is the wave vector, $\vec{h}$ is the reciprocal lattice vector, $\vec{u}$ is the displacement vector of the deformation, and $\beta_h = \dfrac{|\vec{k}_h|^2 - |\vec{k}_0|^2}{2\vec{k}^2}$, $\vec{k}_h$ and $\vec{k}_0$ are the diffracted and transmitted wave vectors respectively.

The solution of these equations gives the diffracted and transmitted beams of a distorted crystal. Different methods have been adopted to solve these equations for the Laue as well as for the Bragg case [10]. Sanchez del Rio et. al.[25] has given the numerical solution of these equations using Finite Element Method(FEM).

2.2.2.3 Penning-Polder (PP) Method

In this method, put forth by Penning and Polder [73], the complete bent crystal is assumed to be made of many perfect crystal-parts misaligned with each other. Then the dynamical theory of undistorted crystal is applied to all these perfect crystal-parts. The X-ray beam is assumed to be propagating through the distorted crystal as a pseudo-plane block wave, i.e. PP method exploits the wave nature of X–rays inside the crystal. This theory also assumes that, while passing from one part of the crystal to the next, the wavefield is preserved. This method is only applicable to the Laue case due to the anomalous absorption effect on the total reflection angle.

Following the paper by Sanchez Del Rio et. al [25], the reflectivity of a symmetric crystal is given by:

$$R = \frac{\xi_{e_j}^2}{\xi_{i_j}^2 + b} \frac{b}{\xi_{i_j}^2 + b} \exp\left\{ -\frac{\mu t}{\cos(\theta_b - \pi/2)} \left[1 + \frac{b-1}{2t\beta}(\xi_{e_j} - \xi_{i_j}) + b\frac{P\ \epsilon}{\beta t} \ln \frac{\xi_{e_j}}{\xi_{i_j}} \right] \right\} \quad (2.21)$$

Where ξ_i represents the ratio of amplitudes of the transmitted and diffracted plane wave components, the subscripts i and e represents the entrance and exit surface respectively. b is the asymmetry factor, μ is the absorption coefficient of the crystal material, t is the optical depth of the beam inside the crystal, P is the polarization factor and ϵ is given by:

$$\epsilon = \frac{\Im_m(\Psi_H)}{\Im_m(\Psi_0)} \quad (2.22)$$

where Ψ_H is the Fourier component of the electrical susceptibility Ψ_0. For an elastically isotropic crystal, the strain gradient, β is given by:

$$\beta = \frac{b-1}{P\ \rho\ \Psi_H} \left[1 + (\cos\theta_b - 1)\frac{1+\nu}{2} \right] \quad (2.23)$$

where ρ is the curvature radius and ν is the Poisson ratio of the material.

2.2.2.4 Malgrange's extension of PP theory

The Malgrange treatment is an extension of the Penning-Polder method. It is valid for bent crystals having large and homogenous curvature radius. In this theory the strain gradient β describes the distortion of the diffraction planes and is given by:

$$\beta = \frac{\Omega}{T_o(\delta/2)} \quad (2.24)$$

where Ω is the total bending angle. It corresponds to the FWHM of the angular distortion distribution of the lattice planes, in case of quasi-mosaic crystals. T_o is the thickness of the crystals and δ is the Darwin's width.

Above a critical value, β_c, of the strain gradient given by $\beta_c = \frac{\pi}{2\Lambda_0}$, where Λ_0 is the extinction length (Eqn. 2.16), the intensity of the diffracted wave decreases because of the creation of a new wavefield. For a uniform curvature C_p of the lattice planes across the crystal thickness and with the condition that the value of the strain gradient β is larger than the critical value β_c, the peak reflectivity, R_{peak} of the curved crystal is given by:

$$R_{peak} = \left[1 - \exp\left(-\frac{\pi^2 d_{hkl}}{C_p \Lambda_0^2}\right)\right]\left[\exp\left(-\frac{\mu\Omega}{C_p \cos\theta_b}\right)\right] \tag{2.25}$$

where $C_p = \frac{\Omega}{T_o}$, is the curvature of the lattice planes assumed to be uniform across the crystal thickness, d_{hkl} is the spacing of the lattice planes (hkl), μ is the absorption coefficient at a given energy and θ_b is the Bragg angle. The extinction length Λ_0 is given by Equation 2.16. Equation 2.25 has been used to simulate the reflectivity and thus the performance of the Laue lens using bent crystals in this thesis.

2.2.3 Crystal thickness

Simulations were performed using the Malgrange equations to define the best thickness for different crystal materials. According to Malgrange's theory, in a curved crystal the reflectivity value is related to the extinction length Λ_0 (Eqn. 2.25 and Eqn. 2.16) that depends on the diffracted energy and crystal material. Taking the derivative of Equation 2.25 and equating the result to zero, we get the condition

Using the Malgrange theory for bent crystals, the extinction length was determined for potentially suitable materials. In Figure 2.3, it is shown the variation of the extinction length Λ_0 of bent crystals as a function of the energy for Si(111) and Ge(111), for different values of the internal curvature.

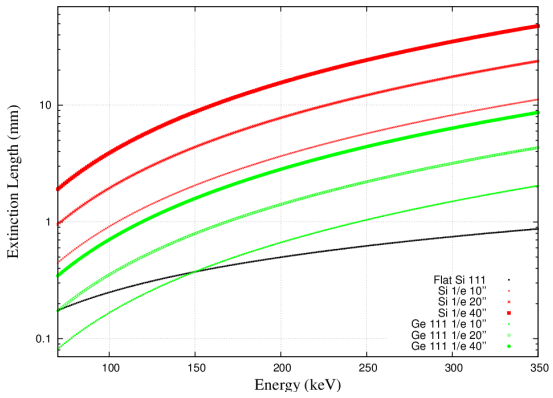

Figure 2.3: Extintion length vs. energy for bent Silicon (red line) and Germanium (green) compared with that of flat Silicon (black) [90].

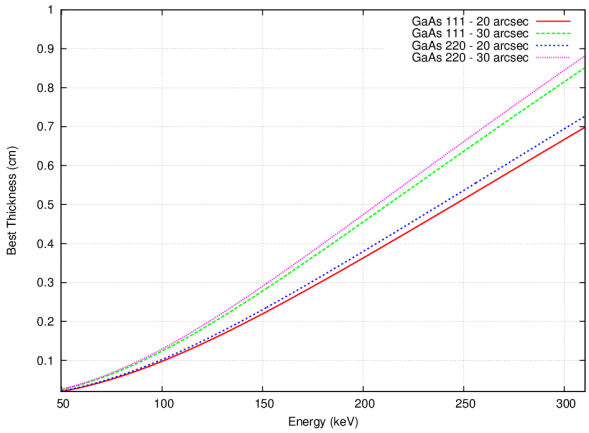

Figure 2.4: Best thickness as function of the energy for crystals made of Gallium Arsenide with different angular spread (20 and 30 arcsec) [90].

Unfortunately bent crystals of Si(111) cannot be used for LAUE project. Indeed bent Si(111) with, e.g., an angular spread of 10 arcsec, shows an extinction length of $\sim$ 1 mm and 3.8 mm at 100 and 200 keV, respectively. Given that the thickness requested for getting a good reflection efficiency requires a few extinction lengths, it results that the thickness requested for Si(111) ranges from 3 to 12 mm, going from 100 keV to 200 keV, respectively. Unfortunately curved crystals of Si(111) with such thickness are not attainable due to the limitation of the current bending technology.

The smaller extinction length of curved Ge(111) makes the required thickness (about 2 mm) feasible.

The relation between the thickness and the energy for bent mosaic GaAs has also been reported in Figure 2.4. Both (111) and (220) planes of GaAs, with 20 and 30 arcsec, are compared. Tiles made of bent GaAs, with an angular spread of 20 arcsec, can be used at low energies ($<$ 150 keV), where a thickness of 2 mm is more than satisfactory.

2.3 Concept of Laue lens

By orienting and positioning the mosaic or curved crystals in a proper way, it is possible to deviate the incoming photons to a focal spot. This is the main idea behind a Laue lens. Figure 2.5 illustrates this concept in the case of flat crystal tiles. A part of incoming photons gets reflected towards the focal spot, whereas other part either gets absorbed or transmitted.

The orientation of the crystals (and hence their lattice planes) has an important role in this process of concentrating the photons to a spot. The crystals has to be oriented on a frame, which is a section of a sphere (a spherical cup), with radius R_s, so that the

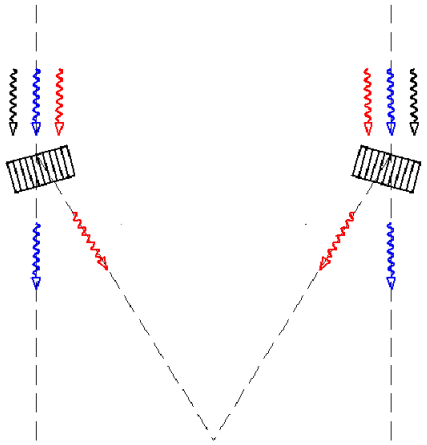

Figure 2.5: Diffraction of photons by properly oriented crystals (in this illustration, flat crystals are used) can be exploited to concentrate the photons to a focal spot. Here the case of Laue diffraction is shown. Only part of the photons get diffracted (shown in *red*). The other parts eirther get transmitted (*blue*) or gets absorbed (*black*).

lattice planes of all the crystals are perpendicular to the spherical surface. (see Figure 2.6). Henceforth this spherical cup will be called as *lens*. With this geometry, the photons get concentrated at a distance $f(= R_s/2)$. The distance between the surface of the spherical frame and this point is the *focal length* of the lens.

Let r_i be the distance from the center of the lens to the center of the i^{th} crystal on the lens. From the Bragg's equation, (Eqn. 2.2), the relation between the radius r_i and the corresponding energy (E_i) of the photons that the i^{th} crystal will reflect can be established.

From Figure 2.6, the angle θ_B is given by

$$\theta_B = \frac{1}{2} \arctan\left(\frac{f}{r}\right) \tag{2.26}$$

Substituting the value of θ_b in Equation 2.2 and then using Equation 2.3,

$$E = \frac{hc\ f}{d_{hkl}\ r} \tag{2.27}$$

Equation 2.27 shows that higher energy photons get reflected at the lower radius of the lens, while crystals placed at higher radius reflect photons with lower energies. This is illustrated in Figure 2.7.

When crystals are arranged around the lens optical axis at constant r, *ring–configuration* is obtained. When crystals are arranged according to a uniformly varying value of r,

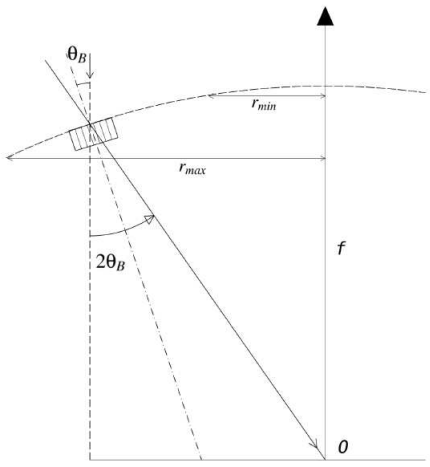

Figure 2.6: The proper orientation of the crystal, and hence it's lattice plane is important in concentrating the photons to a focal spot.

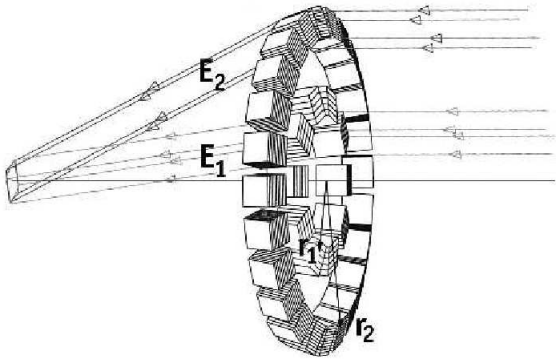

Figure 2.7: Figure illustrating the energy vs radius relation in the case of a lens made with flat crystal tiles. At lower radius (r_1) of the lens, higher energy (E_1) photons gets reflected, while at the higher radius,(r_2) reflection of photons with lower energies (E_2) takes place. Reprinted from [34].

Archimedes spiral configuration is achieved. For the ring–configuration, if all the crystals are assumed to have the same diffracting planes, the energy of the diffracted photon will be centered on E, for all the crystals on a ring. With the same assumption, for an Archimedes spiral configuration, the reflected energy, E will be continuously varying from one crystal to the other.

2.3.1 Energy passband of a lens

One of the important aspect of the Laue lens is to concentrate photons of broad energy band.

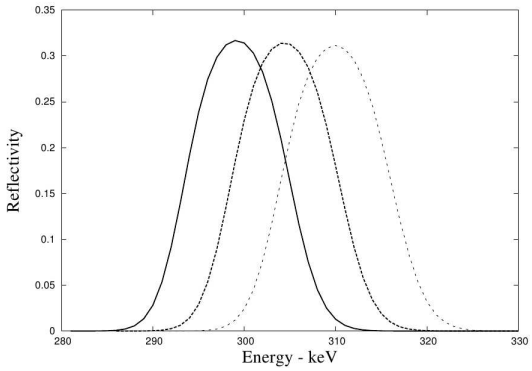

Figure 2.8: An example of an overlapping reflectivity profile of three contiguous crystals (in case of Archimedes configuration) or of three contiguous rings (in case of ring–configuration). This overlapping criteria has to be satisfied in order to get a smooth continuous energy band for the complete lens.

From Equation 2.27, the maximum energy, E_{max} and minimum energy, E_{min} of the photons that can be reflected by the lens is given by:

$$E_{max} = \frac{hc\ f}{d_{hkl}\ r_{min}} \tag{2.28}$$

$$E_{min} = \frac{hc\ f}{d_{hkl}\ r_{max}} \tag{2.29}$$

For this the source is assumed to be on–axis. The continuity of the energy band from E_{min} to E_{max} also depends on the energy band of each crystal. For a smooth continuity, in the ring–configuration, the energy band of each ring should overlap each other. For the Archimedes spiral case, the energy band of each crystal should overlap the energy band of the proceeding crystal. This is illustrated in Figure 2.8.

The energy band of photons that can be reflected by each crystal depends on the mosaicity (for a mosaic crystal) or on the quasi–mosaicity (in case of bent perfect crystal). The Full Width Half Maximum (FWHM) of the energy band (Figure 2.8) of each crystal is called the *acceptance angle*.

Chapter 3

HAXTEL project

This Chapter deals with the second prototype of the HAXTEL project, dedicated to build a focusing optics with 6 meter focal length. A comparison of the resulting output with the simulation is made. The improvement of this prototype with the first one is also discussed.

3.1 Introduction

HAXTEL was the first project supported by Italian Space Agency (ASI) for focusing high energy photons by exploiting the Laue diffraction from crystals. The adopted lens-assembling technique is suited only for lenses with short focal–length (<10 m). The crystals used (flat tiles of 15×15 mm^2 cross section) were made of Cu (111) in mosaic configuration provided by the Institute Laue Langevin (ILL) in Grenoble, France. The lens-assembling required several steps with a resulting cumulative error budget of a few arcmin.

The lens assembly made use of the LARIX–A facility. Two prototypes [36, 94] were built with a focal length of 6 meters. The Cu(111) crystals were arranged on the frame in a ring configuration so as to focus photons with centroid energy of 100 keV.

In this chapter I describe the methodology adopted for building the second prototype and its result.

3.2 Effect of divergence

A Laue lens for astrophysical observations is built taking into account that the incoming rays are parallel. But in laboratory, it is hard to collimate a beam given the finite space available. Indeed our beam is divergent in nature.

The reflectivity, R is given by the ratio of power of the beam diffracted from the crystal, P_d, to the incident power of the beam P_0. Both P_d and P_0 are functions of several parameters.

$$R(T_0, t_0, \beta, \theta, \theta_B) = \frac{P_d(T_0, t_0, \beta, \theta, \theta_B)}{P_0(T_0, t_0, \beta, \theta, \theta_B)} \tag{3.1}$$

$$= \frac{I_d(T_0, t_0, \beta, \theta, \theta_B)}{I_0(T_0, t_0, \beta, \theta, \theta_B)} \tag{3.2}$$

where T_0 is the crystal thickness, t_0 is the crystallite thickness, β is the mosaicity of the crystal, θ is the angle between the pencil beam incident on the crystal and the reflecting lattice plane and θ_B is the Bragg angle. Equation 3.2 is valid in the case of symmetrical reflection (our case). I_d and I_0 are the corresponding diffracted and incident intensities of the photon beam.

If C is the number of reflected photons from the crystal area A in a given time Δt, C can be written as:

$$C(T_0, t_0, \beta, \theta, \theta_B) = R(T_0, t_0, \beta, \theta, \theta_B) \times I_0 \times Area \times \Delta t \tag{3.3}$$

where I_0 is the incident beam intensity (ph cm^{-2} s^{-1}).

Consider a crystal which has been illuminated by a divergent beam (Fig. 3.1). Let dr be the size of infinitesimally small ring of the beam incident on the crystal and let its radius be r_ϕ. The area of the shaded region is given by $dr \times (r_\phi \times d\phi)$.

$$r_\phi = \frac{r_0}{\cos\phi} \tag{3.4}$$

hence,

$$dr_\phi = \frac{dr_0}{\cos\phi} \tag{3.5}$$

where $r_0 = D\ \theta$ with D being the distance of the crystal from the source. This implies $dr_0 = D\ d\theta$.

Substituting these values, $dr_\phi = \frac{D\ d\theta}{\cos\phi}$. Taking these values and integrating over ϕ and θ, the number of reflected photons is given by

$$C(T_0, t_0, \beta, \theta, \theta_B) = 2 \int_{\phi=0}^{\pi} \int_{\theta=\theta_B-\alpha}^{\theta=\theta_B+\alpha} I_0\ R(T_0, t_0, \beta, \theta, \theta_B) \frac{D^2}{\cos^2\phi}\ \theta\ d\theta\ d\phi \times \Delta t \tag{3.6}$$

where α is given by $\frac{l/2}{D}$, l being the length of one side of the crystal.

3.3 Crystal properties and tile selection

The tiles used for building the prototype are mosaic crystals made of Copper with a cross section of 15×15 mm^2 and 3 mm thick. The lattice planes used for the diffraction are those related to the Miller indices (111).

Mosaic crystals are mainly described by mosaicity β, crystallite size t_0 and effective thickness T. The mosaicity is an intrinsic property of the single tile and in principle is

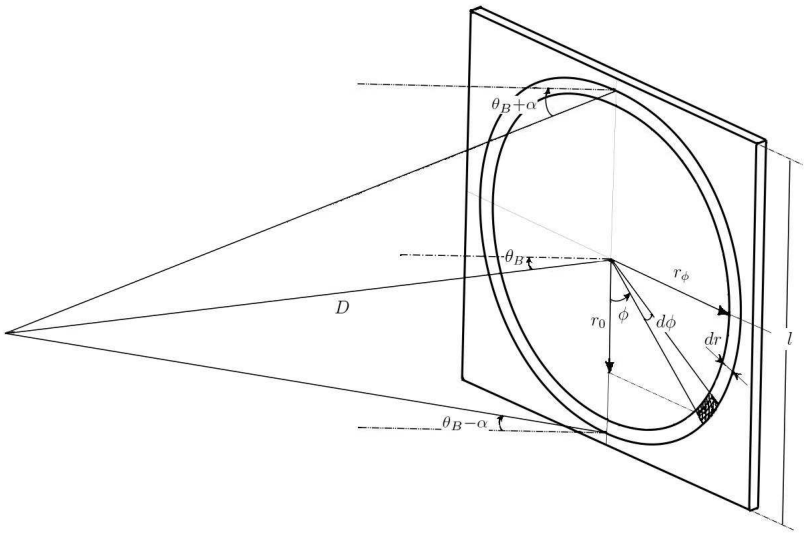

Figure 3.1: Figure showing the divergent beam illuminating a flat crystal. The reflecting planes are assumed to be parallel to the top and bottom surface of this crystal.

the same for all crystals coming from the same ingot. However the effect of the cutting process can give rise to different mosaicities. The best crystallite size that provide the best reflectivity should be at most of the order of ten of μm. Unfortunately also Cu (111) micro crystals beyond 200 micron have been reported [5].

We estimated the parameters of each crystal tile by using the measured rocking curve and comparing it with the expected reflectivity function (see Refs. [105, 34] and references therein), after taking into account the beam divergence.

Indeed, due to the beam divergence, the crystal is hit on its surface with different Bragg angles and this affects the response function which is broader than that expected as a result of the crystal mosaicity. If one ignores the correction for the divergence effect, mosaicity values higher than 6 arcmin and crystallite sizes from 200 to 400 μm are derived. By correcting for the divergence effect, significant lower parameter values are obtained (μ = 2.0–3.0 arcmin; t_0 = 30–70 micron).

The divergence–corrected results were also tested with an experimental procedure. For a subset of crystal tiles, lower and lower beam divergence values, obtained by decreasing the beam size from 10×10 mm^2 to 2×2 mm^2, were obtained and the corresponding reflectivity measured. Without taking into account the correction for divergence, we derived the gross mosaicity (called *equivalent mosaicity*) dependence on beam divergence which is shown

in Fig. 3.2.

As can be clearly seen, as the divergence converges to zero (beam size approaching to ~ 0), the equivalent mosaicity reaches the crystal mosaicity. With this method, for the subset of 3 chosen crystals (No. 2, 8, 17), we estimated a crystal mosaicity of 2.57, 2.55 and 2.68 arcmin, respectively, These values are in good agreement with that estimated with the divergence corrected fitting procedure (2.72, 2.48 and 2.84 arcmin).

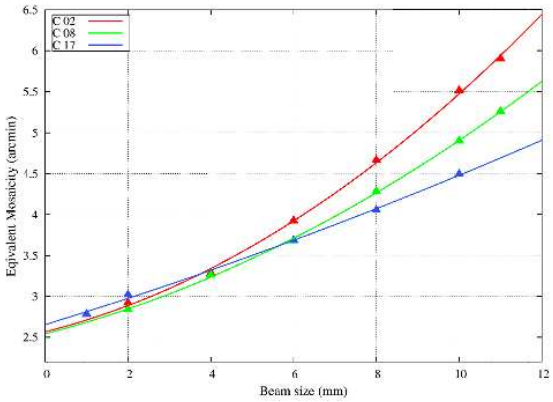

Figure 3.2: The *equivalent mosaicity* as a function of the beam size for a subset of crystal. Superimposed to the experimental data, a polynomial function was used to fit and extrapolate the real value of the mosaicity, at beam size equal to zero.

3.4 The Lens assembly technique and its development facility

Details of the lens assembling steps have already been reported [36, 64, 30]. In short, the adopted lens assembling technique is based on the use of a counter-mask provided with holes, two for each crystal tile. Each tile is placed on the counter-mask by means of two pins, steadily glued to the tile, that are inserted in the counter-mask holes.

In the case of the developed prototype model, the hole axis is set parallel to that of the lens axis. This choice has been made to illuminate the entire lens with the available polychromatic hard X-ray source placed at 6 m far from the lens.

Once all the crystals are positioned on the counter-mask, a carbon fiber frame is placed above the counter-mask/crystal structure and glued to the entire set of crystals. The lens frame, along with the crystals, is thus separated from the counter-mask.

The lens assembly apparatus is installed in the section A of the LArge Italian X-ray Facility (LARIX) located in the Physics Department of Ferrara. In addition to a set of devices employed for the specific project, the facility includes an X-ray generator with a fine focus of 0.4 mm radius with a maximum voltage of 150 kV and a maximum power of $\sim$ 200 W. The photons coming out from the X-ray tube are directed towards a collimator aperture which can be remotely adjusted in two orthogonal directions for beam size optimization. The lens building phase and performance test are performed by means of two detectors: an X-ray imaging detector with spatial resolution of 300 μm and a cooled HPGe spectrometer with 800 eV spectral resolution. Both are located on a rail and can be moved back and forth along the beam axis. They are used to collect direct photons and those diffracted from the crystal tiles.

3.5 Improvements with the new prototype

After the development of the first prototype described in Ref. [36], new improvements and tests have been performed in terms of assembling technology and of knowledge of the error budget introduced by each single step of the entire assembly process. A description of the improvements and changes is the subject of a patent which is being submitted.

Figure 3.3 shows the assembled prototype (*top*) and the carbon fiber support (*bottom*).

3.6 Lens testing and results

Once the assembled lens is separated from the counter-mask, for its testing the lens is positioned on a support of the LARIX facility located at half way (about 6 m) between gamma-ray source and focal plane detectors. These can be remotely translated back and forth along the beam axis for finding the best focusing position and for getting, out of focus, the image position of each crystal.

To avoid direct radiation to arrive on the focal plane detector, the entire inner region of the lens frame is covered by a lead layer 3 mm thick. The left panel of Fig. 3.4 shows the first light of the developed prototype when the polychromatic beam irradiates the entire lens.

With Monte Carlo techniques, and accounting for the divergence of the beam as well as the mosaicity of the crystals, the PSF, for an ideal lens with diffraction from perfectly aligned crystals, was derived. The comparison between the expected PSF and that obtained with the lens prototype is shown in Fig. 3.4 (right panel). The dark circular region shows the expected PSF.

Instead Fig. 3.5 shows the cumulative distribution of the number of photons collected along the radial distance from the focal point. As can be seen, while the expected half power radius (HPR), i.e. the radius within which 50% photons are collected, is 9 mm, the measured HPR was 17.4 mm for the first prototype [36], and 13.9 mm for the second

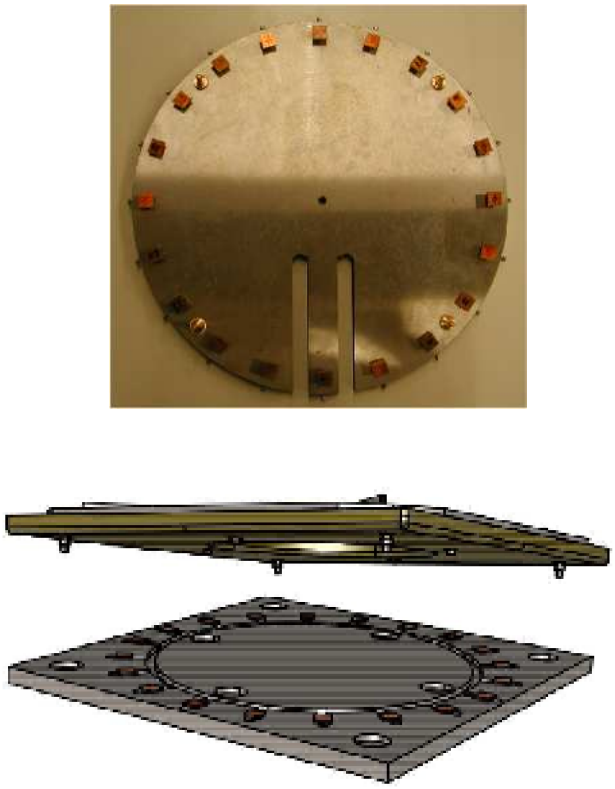

Figure 3.3: The counter-mask (*top*) with the 20 crystals placed, and the carbon fiber support (*bottom*).

prototype. There is an improvement of about 41% with respect to the first prototype, considering the theoretical value of the radius(9 mm) as the target. Thus this represents a significant improvement with respect to the first one. It can be also seen that, at the radius (16.00 mm) at which the saturation occurs for the expected cumulative distribution, the fraction of collected photons is around 0.7, with respect to the first prototype in which the fraction was less then 60%.

The spectral analysis of the focused beam was also performed and the results are presented in Fig. 3.6. The lens prototype was designed for giving a spectral peak at 100 keV at the focal point. In the left panel it is shown the spectrum obtained collecting only the photons coming in the central region of the focus, while in the right panel, it is shown the spectrum of all the photons reflected by the lens and collected on the focal plane. In both cases the exposure time was 1000 seconds. As can be seen, in the central region the peak is at 98.89 keV. The centroid of the spectrum of the central region achieves an

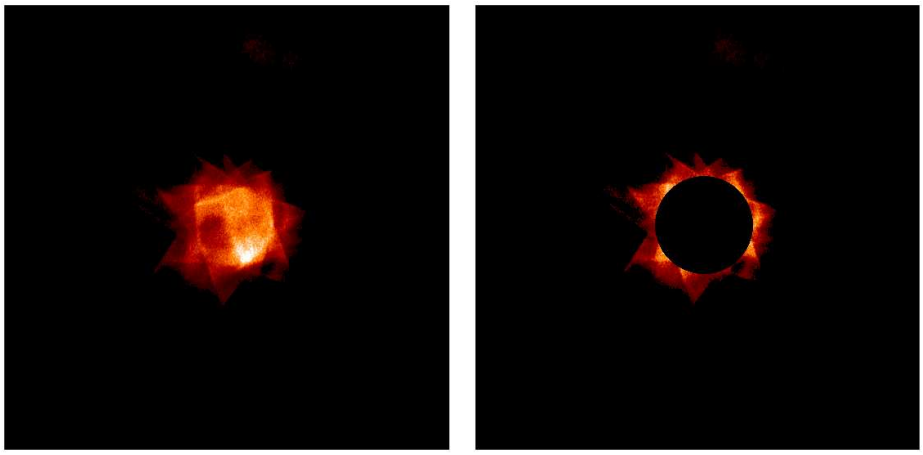

Figure 3.4: *Left panel*: Point spread function obtained with the developed prototype. *Right panel*: Difference between the prototype PSF and the spot expected from Monte Carlo simulations assuming diffraction images from perfectly aligned crystals.

intensity level 0.8 times that of the peak spectrum of all reflected photons.

Also a thorough spectral analysis was performed for each single crystal, in order to estimate the misalignment distribution in terms of centroid energy diffracted from each crystal tile. The results are reported in Table 3.6 in which, along with the peak energy and the FWHM of the spectrum diffracted by each crystal, the angular deviation of each crystal from the theoretical one is also evaluated.

By shielding all the lens crystals but one, and measuring the barycenter coordinate of each diffracted spot, also the angular misalignment was determined for each lens crystal. Figure 3.8 shows the deviation occurred for each crystal, from their expected perfect position. For the total set of tiles, this deviation is within 6 arcmin (for the first prototype it was 15 arcmin).

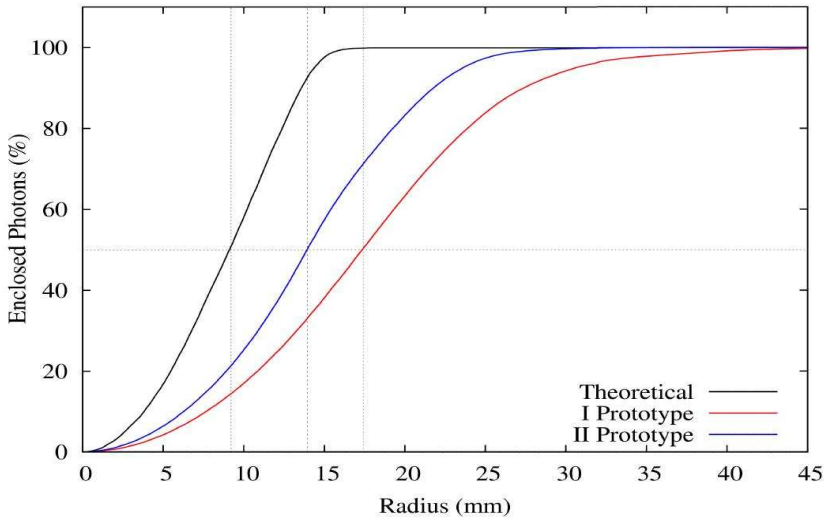

Figure 3.5: Cumulative distribution of the focused photons along the radial distance from the focal point. *Black line* corresponds to the expected distribution in the case of a perfect alignment of the crystals. The *red line* shows the photon distribution obtained in the first prototype ([36]) while the *blue line* shows photon distribution for the second prototype.

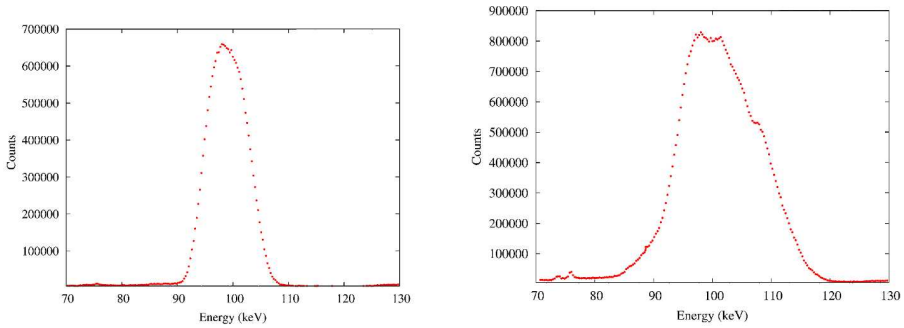

Figure 3.6: *Left panel*: Spectrum of the total photons reflected on the focus. *Right panel*: Spectrum of the total photons reflected by the lens in the region in and around the focus, in the focal plane.

3.7 Conclusion

The performance of a focusing lens made of 20 crystals, assembled by in the LARIX facility of the University of Ferrara has been discussed.

Table 3.1: Measured peak energy, FWHM and angular deviation for each of the crystals with respect to the diffracted energy of the lens.

Crystal Number	Peak Energy (keV)	FWHM (keV)	$\Delta\theta$ (arcmin)	Crystal Number	Peak Energy (keV)	FWHM (keV)	$\Delta\theta$ (arcmin)
1	102.31	6.53	-3.54	13	96.88	5.39	2.08
2	98.37	5.01	0.53	14	103.70	6.83	-4.99
3	101.47	5.65	-2.67	16	104.66	6.15	-5.99
4	104.45	7.13	-5.76	17	103.92	5.94	-5.22
5	97.09	4.50	1.87	18	105.27	6.15	-6.62
6	99.29	5.31	-0.41	20	99.79	6.67	-0.93
8	103.10	6.33	-4.36	21	103.81	5.17	-5.10
9	104.49	6.31	-5.81	23	104.52	7.50	-5.84
11	96.42	5.12	2.53	27	94.12	6.78	4.95
12	98.60	5.33	0.29	28	95.27	7.08	3.76

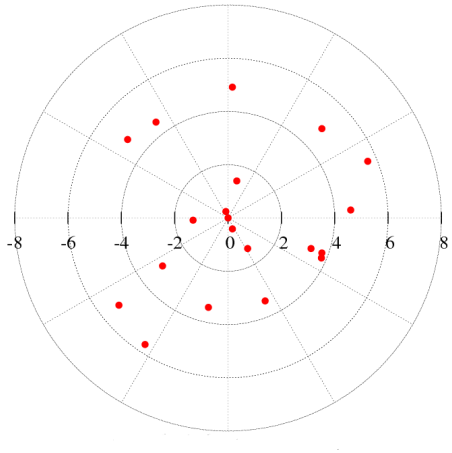

Figure 3.7: Angular deviation of each crystal on the lens with respect to the perfect alignment.

Compared to the first prototype, the performance in terms of imaging capability has been improved. The maximum angular deviation of the crystal tiles from their nominal ones has been decreased from 15 arcmin (for the first

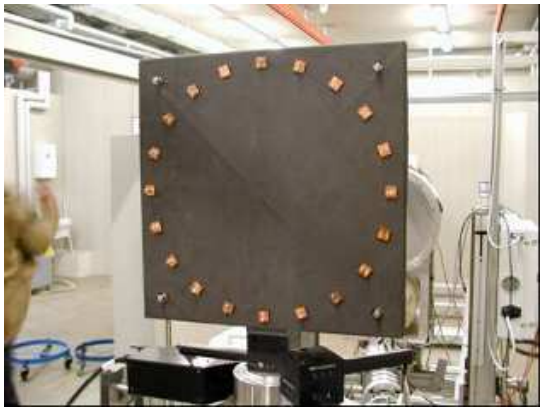

Figure 3.8: The Laue lens 2^{nd} prototype.

prototype) to 6 arcmin.

The contribution of each step to the overall error budget has been evaluated. The alignment of the lattice planes with the gamma-ray beam axis has been performed with a precision better than 30 arcsec. The pin-holder alignment with the beam axis has been estimated to show a similar precision. The holes of the pin-holder are drilled parallel to the beam axis with an uncertainty of less than 20 arcsec. The same tolerance is in the direction of the counter-mask holes. Considering the 6 arcmin of mismatch between real and expected positioning of the crystals, we attribute this mismatch mainly to the mechanical insertion of the pins in the counter-mask and to the successive separation process of the entire lens from the counter-mask.

In order to improve further the lens PSF, the only way we see is that of adopting a different assembling technique, in which each crystal tile is directly glued on the lens frame under a gamma-ray beam control. This is the goal of the LAUE project supported by the Italian Space Agency ASI, for the production of a lens petal prototype with 20 m focal length with an accuracy in the crystal orientation better than 10 arcsec.

Chapter 4

Modelling and simulation of the Petal with results

From the experience acquired from the HAXTEL project, we move on to the development of an advanced lens assembling technology that will allow to accurately build Laue lenses for space astrophysics. The initial stage being to build a petal. Modeling the lens and simulating its output is a significant process before the lens is being made. In this Chapter I describe the overall process associated with modeling the petal structure and then the results of the simulation of the petal output PSF. Later on this output is qualitatively analyzed.

4.1 Material selection and crystal geometry

The HAXTEL project utilised Cu(111) mosaic crystals. The mosaicity of this crystal configuration is 2.5 to 3.5 arcmin, which is also the minimum achievable angular spread of the lens. In the Laue project, as the photons has to be focused at a distance of 20 meters from the petal, and for an efficient concentration of the photons, the angular spread must be much smaller than 1 arcmin. Decreasing the focal spot area increases the signal to noise ratio. The bent crystal, when compared to their mosaic counterpart, has high efficiency and low mosaicity. i.e., curved crystals have high diffraction efficiency and a better capability of concentrating the signal collected over a large area into a small focal spot. Thus, for the first time, a Laue lens petal completely made of bent crystals is being assembled.

Bent crystals of Ge(111) and GaAs(220) have been selected for the LAUE project, both in transmission configuration. One of them, (GaAs), has a mosaic structure with about 25 arcsec mosaicity, while the other, (Ge), is a perfect crystal that has been bent. The bending technology adopted for Ge is the surface grooving [49], while that adopted for

GaAs is a lapping process [68, 13]. The selected tiles will be provided respectively by the "Laboratorio Sensori e Semiconduttori" (LSS) of Ferrara and by the "Istituto Materiali per Elettronica e Magnetismo" (IMEM) of Parma (Italy). A description of the material's properties is given in the Table 4.1.

The expected reflectivity and the custom radius of each specimen has been investigated and measured. (see Ref. [62]). While GaAs has a mosaic structure, Ge(111) shows a quasi-mosaic structure.

Table 4.1: Properties of the selected materials to be used as elements for the LAUE project.

Properties	GaAs	Ge
Chosen lattice planes	(220)	(111)
Crystal structure	Mosaic, Curved	Quasi-mosaic, Curved
Cross-section (mm^2)	30×10	30×10
Thickness (mm)	2	2
Mosaicity FWHM (arcsec)	25	4.12
External Curvature Radius (m)	40	40

From the dynamical theory of diffraction of bent crystals, it results that the bending of a perfect crystal creates a curvature of the lattice planes (111) of Ge, with a ratio between the internal curvature and external curvature radii of 2.6. This gives rise to a quasi-mosaic configuration of the bent crystal (see Fig. 4.1). This effect is not valid for all lattice planes. For example, if the diffracting planes in transmission configuration are (220), the quasi-mosaicity is not created.

The advantage of bent perfect crystals is that their reflectivity exceeds the theoretical limit of 50%, valid for flat perfect crystals.

The focusing capability is also better when the crystal is bent [50]. When a mosaic crystal is bent, the mean crystallite Gaussian distribution is expected to continuously change along the crystal (Fig. 4.2). Experimental tests confirm the expectations [62].

4.1.1 Crystal thickness

Simulations based on crystal geometry were performed using the Malgrange equations to define the best thickness for each specimen. According to Malgrange's theory, in a flat crystal the reflectivity value is related to the extinction length Λ_0 (e.g., Ref. [34]) that depends on the diffracted energy and crystal material.

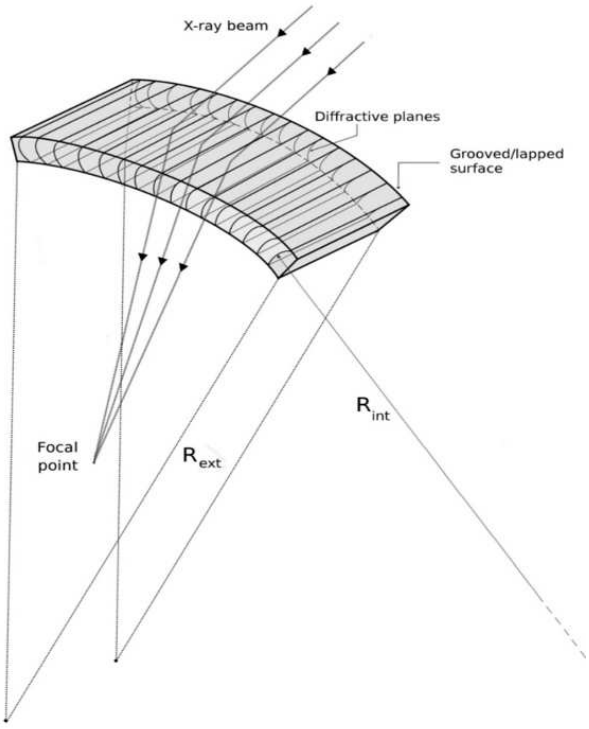

Figure 4.1: Quasi-mosaic crystal principle. The FWHM in this case depends upon the internal curvature of the atomic planes caused by the bending of the crystal.

Using the Malgrange theory for bent crystals, the extinction length was determined for potentially suitable materials. In Figure 2.3 (Chapter 2), it is shown the variation of the extinction length Λ_0^b of bent crystals as a function of the energy for Si(111) and Ge(111), for different values of the internal curvature.

Unfortunately bent crystals of Si(111) cannot be used for LAUE project. Indeed bent Si(111) with, e.g., an angular spread of 10 arcsec, shows an extinction length of $\sim$ 1 mm and 3.8 mm at 100 and 200 keV, respectively. Given that the expected thickness for getting a good reflection efficiency requires a few extinction lengths, it results that the thickness required for Si(111) ranges from 3 to 12 mm, going from 100 keV to 200 keV, respectively. Unfortunately curved crystals of Si(111) with such thickness are not attainable due to the limitation of the current bending technology.

The smaller extinction length of curved Ge(111) makes the required thickness (about 2 mm) feasible.

The relation between the thickness and the energy for bent mosaic GaAs has also been reported in Figure 2.4. Both (111) and (220) planes of GaAs, with 20 and 30 arcsec, are compared. Tiles made of bent GaAs will be used at low energies ($<$ 150 keV), where a

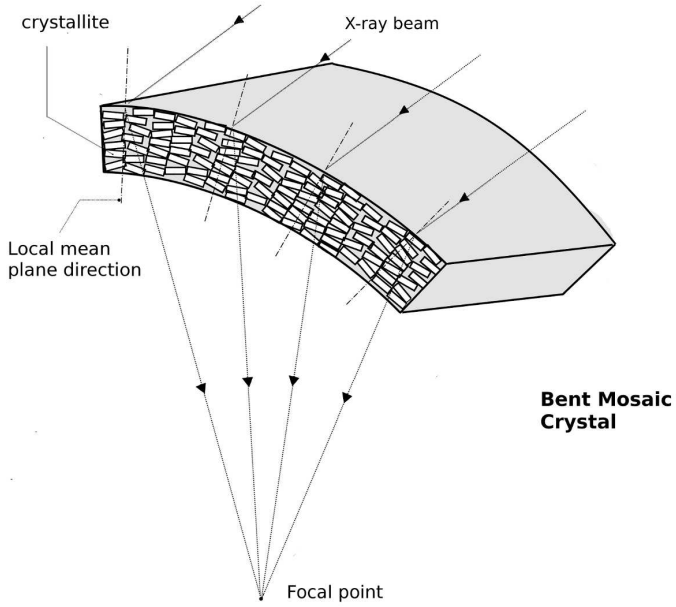

Figure 4.2: Bent crystal principle in the Mosaic configuration. The FWHM of the reflectivity of these crystals depends upon the mosaicity of the crystals.

thickness of 2 mm is more than satisfactory, with an angular spread of 20 arcsec.

4.2 Modelling the petal structure

The petal structure is modelled in such a way as to diffract photons in the energy band of 90 keV – 300 keV. The crystals will be positioned and glued to the frame so as to focus the diffracted beam at a distance of 20 meters.

The petal frame, on which the crystals have to be glued, is designed with respect to various factors or constraints related to the LARIX facility. These are:

- **Radius R_{pl} of the beamline**
  The beamline has an inner radius of 30 cm. Hence the complete petal structure should be designed in such a way that it fits perfectly within the dimensions of the beamline.
- **Angle θ subtended by the petal WRT the center of the lens**
  The complete lens is meant to be composed of 20 petals, which implies that each petal will subtend an angle of 18 degrees with respect to the center of the lens.
- **Focal length f of the lens/petal**

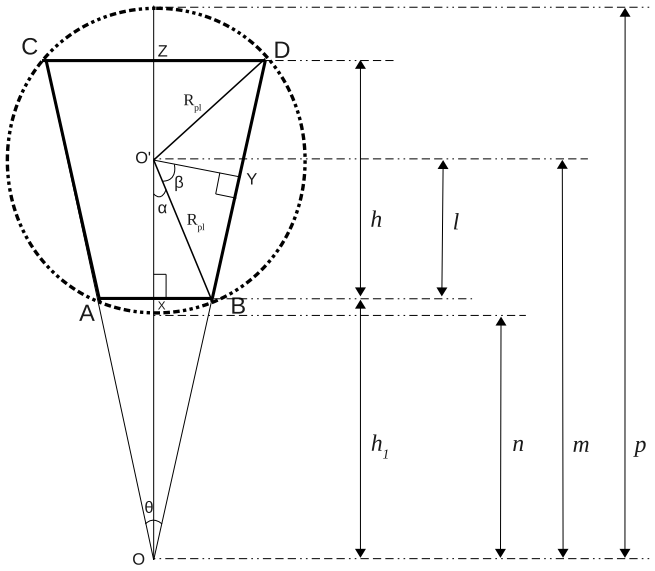

Figure 4.3: Diagram illustrating the design of the petal structure, $ABCD$. The circle (shown by the *dotted* lines) represents the beamline which has a diameter of 60 cm.

The diffracted photons should focus on the detectors at the focal plane which is at a distance of 20 meters from the petal/lens structure.

- **Maximum energy E_{max} to be diffracted**
  The maximum energy limit of the source, in the LARIX facility, is 320 keV. Hence I have restricted the maximum energy to be diffracted by the petal to 300 keV.

- **Maximum radius R_{max} of the petal**
  The horizontal dimension of the LARIX facility is $\approx$ 2 meters. Setting a limit of 1 meter for the maximum radius R_{max} of the petal will be well enough.

These are the conditions that has to be met and to be optimised for designing the petal frame.

In Figure 4.3, the design of the petal structure is illustrated. The trapezoid, $ABCD$ represents the petal and the circle (shown by the *dotted* lines) represents the beamline which has an inner diameter of 60 cm. Other symbols are described below.

- OC, OD represents the maximum radius, R_{max} of the petal structure;
- OA, OB is the minimum radius, R_{min};

- $AB(= a)$ is the smallest arc of the petal, which is parallel to $CD(= b)$;
- $O'B = O'D = R_{pl}$, the inner radius of the beamline. R_{pl} is taken to be equal to 28 cm, instead of 30 cm, for the calculations;
- h is the height of the petal structure;
- n is the minimum distance of the beamline from the lens axis,(O);
- m is the distance from the lens axis,(O) to the middle of the beamline;
- p is the maximum distance of the beamline from the lens axis;
- h_1 is the minimum distance of the lens petal from the lens axis.

From the equation,

$$R_{min} = \frac{hc \times f}{d_{hkl} E_{max}} \tag{4.1}$$

the minimum radius, R_{min}, required to diffract the maximum energy, E_{max} can be found. In the above equation, hc = 12.398 Å and d_{hkl} is the spacing of lattice planes (hkl).
From R_{min},

$$h_1 = R_{min} \cos(\theta/2)$$
$$\overline{XB} = R_{min} \sin(\theta/2)$$

which gives,

$$\overline{AB} = a = 2 \times \overline{XB} \tag{4.2}$$

$$\alpha = \arcsin\left(\frac{\overline{XB}}{R_{pl}}\right)$$
$$\measuredangle O'BO = \pi - [\alpha + \theta/2]$$
$$\measuredangle O'BY = \pi - \measuredangle O'BO = \alpha + \theta/2$$
$$\beta = \pi/2 - [\alpha + \theta/2]$$
$$\overline{BY} = R_{pl} \sin\beta$$

Hence,

$$R_{max} = R_{min} + 2\overline{BY} \tag{4.3}$$
$$E_{min} = \frac{hc \times f}{d_{hkl} R_{max}} \tag{4.4}$$

Also,

$$b = 2\overline{ZD} = 2R_{max}\sin(\theta/2) \tag{4.5}$$

$$h = \frac{\overline{ZD}}{\tan(\theta/2)} - h_1 \tag{4.6}$$

$$m = R_{min} + l \tag{4.7}$$

$$n = m - R_{pl} \tag{4.8}$$

$$p = m + R_{pl} \tag{4.9}$$

where $l = \sqrt{R_{pl}^2 - \overline{XB}^2}$

The dimensions of the petal frame, to get a passband with upper threshold of 300 keV, depend also upon the material of the crystal tile used (depends upon d_{hkl} of the crystal material). Table 4.2 shows the dimensions of the petal frame corresponding to the crystal material used for designing it. The dimensions of each frame is well within the constraints (including R_{max} and E_{max}), mentioned before.

Table 4.2: Dimensions of the petal structure designed with respect to the crystal material used. Here the diameter of the beamline is taken to be 56 cm and the angle subtended by the petal is 18 degrees.

Crystal material	d_{hkl} (Å)	R_{min} (cm)	R_{max} (cm)	E_{min} (keV)	E_{max} (keV)	a (cm)	b (cm)	h (cm)	n (cm)	m (cm)	p (cm)
Ge(111)	3.267	25.30	78.82	96.32	300	7.91	24.66	52.85	25.02	53.02	81.02
GaAs(220)	1.998	41.35	93.14	133.19	300	12.93	29.14	51.15	40.59	68.59	96.59
Ge(220)	2.000	41.32	93.12	133.14	300	12.93	29.13	51.15	40.57	68.57	96.57
Si(111)	3.135	26.36	79.77	99.12	300	8.24	24.96	52.75	26.05	54.05	82.05
Si(220)	1.92	43.05	94.62	136.47	300	13.46	29.60	50.94	42.22	70.22	98.22

The crystals that will be used for building the petal in LARIX facility will be Ge(111) and GaAs(220). Accordingly, the design of the frame should be made with one of these material configurations. The petal frame designed on the basis of these two materials is given in Table 4.3. This table also provides the information about the maximum and minimum energy that can be diffracted with one material when placed within the dimensions of the petal frame designed WRT the other material.

Both these materials will be used to build the petal. Hence the frame designed WRT one material has to accommodate the other material, optimising the required conditions and also to provide diffraction within the energy band of 90 – 300 keV.

Table 4.3: Dimensions of the petal designed WRT Ge(111) and GaAs(220). This also shows the corresponding energy band that can be obtained when one material is placed within the dimensions of the frame designed WRT the other material.

Frame	R_{min}	R_{max}	Ge(111)		GaAs(220)	
	(cm)	(cm)	E_{min}	E_{max}	E_{min}	E_{max}
Ge(111)	25.30	78.82	96.32	300	157.38	490.19
GaAs(220)	41.35	93.14	81.51	183.60	133.19	300.00

From Table 4.2, it is seen that petal frame designed with Ge(111) satisfies the requirement of the energy passband. Using Equation 4.1, the radius, R_{min}, corresponding to 300 keV for GaAs(220) is 41.35 cm. Using trial and error method, by putting the maximum energy equal to 267 keV, the petal frame designed on the basis of Ge(111) crystal configuration, gives an optimized result. This is given in Table 4.4.

Table 4.4 also gives the detailed description of the design of the petal frame and the corresponding energy band each crystal material will be diffracting. Ge(111) crystal tiles will be diffracting photons of energy passband 90 – 267 keV and GaAs(220) crystal tiles will be diffracting photons within a passband of 148 – 304 keV. That makes the complete passband of the petal from 90 – 304 keV.

The petal frame has the role of support for the crystals of the complete lens. The crystals are properly aligned and placed in the correct position, then glued and attached to the petal frame. As well as the hexapod system, the petal frame (see Fig. 4.4) has been provided by DTM - Technologies (Modena). Its total thickness (2.3 mm) is realized with a superposition of 10 layers of carbon fibre. To allow the injection of the glue, the frame is drilled at the level of the central position of each crystal tile.

Fig.4.5 illustrates the petal structure and also the respective position of each crystal tile. Table 4.4 shows different parameters of this petal.

Ring-by-ring parameters of the petal structure that is being build in the LARIX facility is given in Table 4.5.

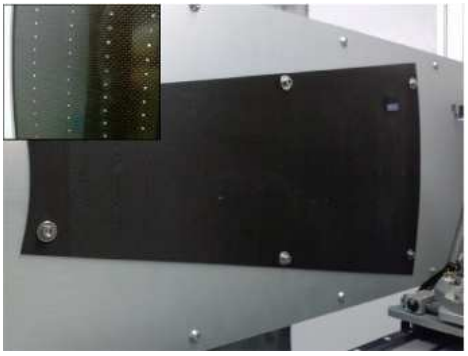

Figure 4.4: The petal frame used as a support for the Laue lens. The small box shows a portion of the petal with the holes used to inject the adhesive from the back side.

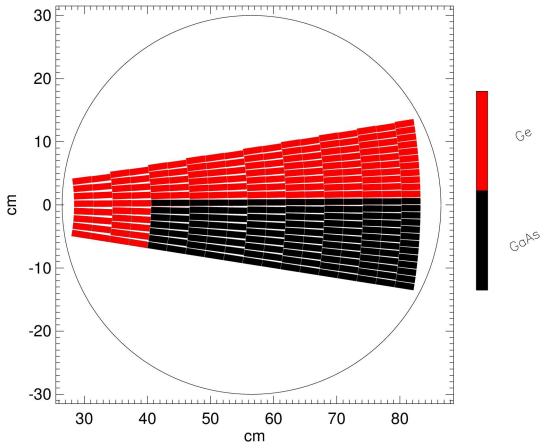

Figure 4.5: An illustration of the petal structure (that is being build in the LARIX facility) and the position of each crystal tile on it.

4.3 Modelling the petal PSF

The Point Spread Function (PSF) gives the spatial distribution of the reflected photons in the focal plane when a point source at infinity is incident on the lens or petal.

The output PSF has been simulated taking into account all types of misalignment and distortion effects. The output of the lens is formed by the beams reflected from all the crystals positioned on the lens. Thus, for a good output, a precise positioning of each

Table 4.4: Parameters of the petal that is being build in the LARIX facility.

Parameter	Value		
	section of GaAs(220)	section of Ge(111)	Entire petal
Focal length	20 meters	20 meters	20 meters
Energy range	148 - 304 keV	90 - 267 keV	90 - 304 keV
No. of rings	14	18	18
Minimum radius	40.66 cm	28.40 cm	28.40 cm
Maximum radius	83.47 cm	83.47 cm	83.47 cm
No. of crystal tiles	119	155	274
Crystal dimension	30mm × 10mm × 2mm	30mm × 10mm × 2mm	30mm × 10mm × 2mm
Crystal mass (total)	2.5 g × 119 = 297.5 g	2.07 g × 155 = 320.85 g	618.35 g

crystal tile on the lens is crucial. A slight deviation or misalignment in placing the crystal from the nominal position creates a distortion in the PSF.
The other factor which effects the PSF is the distortion in the curvature of the crystals. The petal will be made of GaAs(220) and Ge(111) crystals curved with a radius of 40 meter. Any deviation from this curvature radius, will also distort the PSF. The lens petal that has been simulated, is separately made up of Ge(111) and GaAs(220) crystal tiles, with an energy band from ≈90 keV to ≈300 keV.

4.3.1 Factors affecting the PSF of the lens

Two main factors, that affect the PSF considerably, have been considered for simulation.

4.3.1.1 Misalignment in the positioning of the crystal

Each crystal tile is positioned on the lens petal frame with an orientation such that the image of the beam reflected by the crystal is formed on the lens focus, where there is the position sensitive focal plane detector. This methodology is used because the final aim of the lens is to concentrate all the photons in a point. A precise robot is used for the process of crystal positioning. Once the crystal is correctly positioned, it is glued on the lens petal frame.

When a crystal is having a misalignment from its proper position, the image of that crystal on the detector will have a deviation. In Fig.4.6, let (x_0, y_0) be the center of the image formed by the reflection of rays from a crystal, which is perfectly positioned on the lens petal frame without any misalignment. (x_1, y_1) is the position of the center of the image formed by a crystal having a misalignment of Θ arcsec with respect to its

Table 4.5: Ring-by-ring parameters of the petals structure that is being build at the LARIX facility.

Ring	Mean radius	GaAs(220)		Ge(111)	
No.	(cm)	No. of crystal tiles	Mean energy (keV)	No. of crystal tiles	Mean energy (keV)
1	81.97	11	151.23	11	92.55
2	78.91	11	157.10	11	96.14
3	75.85	10	163.44	10	100.02
4	72.79	10	170.31	10	104.23
5	69.72	10	177.79	10	108.81
6	66.66	9	185.96	9	113.81
7	63.60	9	194.91	9	119.29
8	60.54	8	204.77	8	125.32
9	57.47	8	215.69	8	132.00
10	54.41	7	227.83	7	139.43
11	51.53	7	241.42	7	147.75
12	48.28	7	256.73	7	157.12
13	45.25	6	274.12	6	167.76
14	42.16	6	294.04	6	179.95
15	39.09	–	–	10	194.06
16	36.03	–	–	10	210.56
17	32.96	–	–	8	230.13
18	29.90	–	–	8	253.72

proper positioning. Crystals $C1$ and $C2$ are perfectly positioned. Crystal $C3$ is having a misalignment of Θ arcsec. The center of its image is formed on the detector at (x_1, y_1). The deviation of the center of the image from (x_0, y_0) to (x_1, y_1) is shown on the right side of Fig.4.6. For a given misalignment of Θ arcsec, Λ is given by:

$$\Lambda = f\ \Theta \tag{4.10}$$

where f (= 20 meters) is the focal length of the lens petal.

The angle α (see Fig. 4.6, *right*) is expected to have a uniform distribution. That is, there is a uniform probability of having the point (x_1, y_1) over the locus of the circle with center at (x_0, y_0) and a radius of Λ.

The expected misalignment, Θ, is of the order of few arcsec. The effects of this mis-

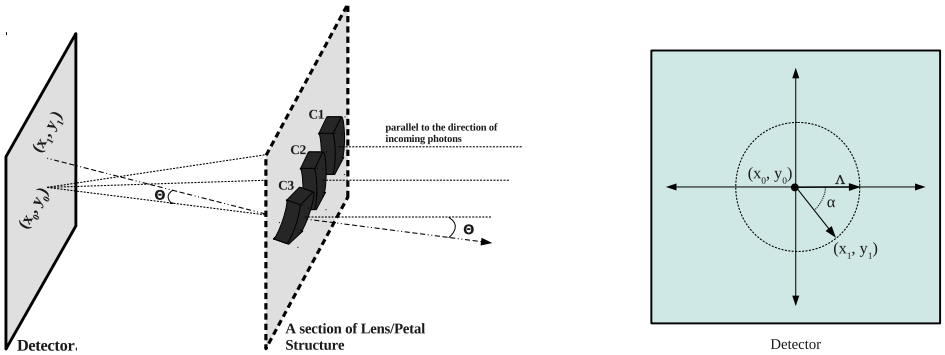

Figure 4.6: Misalignment in the positioning of the crystals on the lens petal frame deviates the PSF. $Left$ figure illustrates this effect. (x_0, y_0) is the position on the detector where the center of the image formed by the reflection of rays through a perfectly positioned crystal falls. When there is a misalignment of Θ arcsec in the positioning, the center of the image is formed at (x_1, y_1). The figure on the *right* shows the focal plane (where there is the detector) with these positions. The amplitude Λ and angle α is described in section 4.3.1.1.

alignment have been incorporated in the code, with a uniform distribution. For example, given a misalignment of 30 arcsec, all the crystals forming the lens petal will have a misalignment in their positioning in the range (-30, 30) arcsec with uniform distribution.

4.3.1.2 Distortion in the curvature radius

Before placing a single crystal tile on the frame, the curvature radius of each crystal is measured at the small LARIX facility. The deviation, if any, of the curvature radius from its expected value is measured. Ge(111) crystals have a secondary curvature which is related to its primary one. Figure 4.7 clearly illustrates the effect of radial distortion (R_{dist}) on the PSF. The width of the PSF is equal for a symmetrical deviation of the curvature radius from its expected value. That is, if R_p is the expected value of the curvature radius, and ΔR is the distortion from the expected value, the width of the PSF is equal for a curvature radius of $R_p + \Delta R$ or $R_p - \Delta R$.

As Ge(111) and GaAs(220) crystals have different geometry, the methodology used for the calculation of the effect of radial distortion is also different.

Case of GaAs(220): Mosaic crystals

From the Fig.4.8, R_p is the expected curvature radius, f is the focal length corresponding to R_p. $R_d = R_p + \Delta R$, ΔR being the distortion in curvature radius. f_d is the focal length

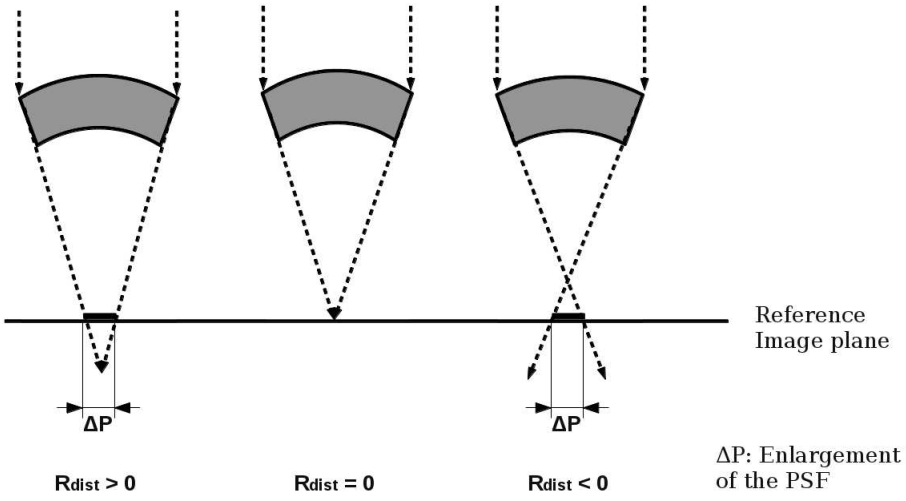

Figure 4.7: The effect of radial distortion (R_{dist}) on the PSF of the lens.

corresponding to R_d.
At f, the width W of the PSF is related to the mosaicity θ_{mos} of the crystal. (For GaAs(220) the mosaicity is 25 $arcsec$). Thus, $W = \theta_{mos} f$. At f_d, the width W_{fd} is given by $W_{fd} = \theta_{mos} f_d$.
W_d is the width of this image on the focal plane detector located at f. W_d can be derived as follows.

From Figure 4.8,

$$dim_t = \frac{dim_0 - W_{fd}}{2}$$
$$\alpha = \frac{dim_t}{f_d}$$
$$\Delta f = |f_d - f|$$
$$\Delta W = \Delta f \alpha$$
$$W_d = W_{fd} + 2\Delta W$$

Case of Ge(111): Quasi-mosaic crystals

From the Fig.4.9, R_p is the expected primary curvature radius, f is the focal length corresponding to R_p. $R_s = 2.56R_p$, is the secondary curvature radius corresponding to R_p. $R_d = R_p + \Delta R$, ΔR being the distortion in curvature radius. f_d is the focal length corresponding to R_d. $R_{sd} = 2.56R_d$, is the secondary curvature radius corresponding to R_d.

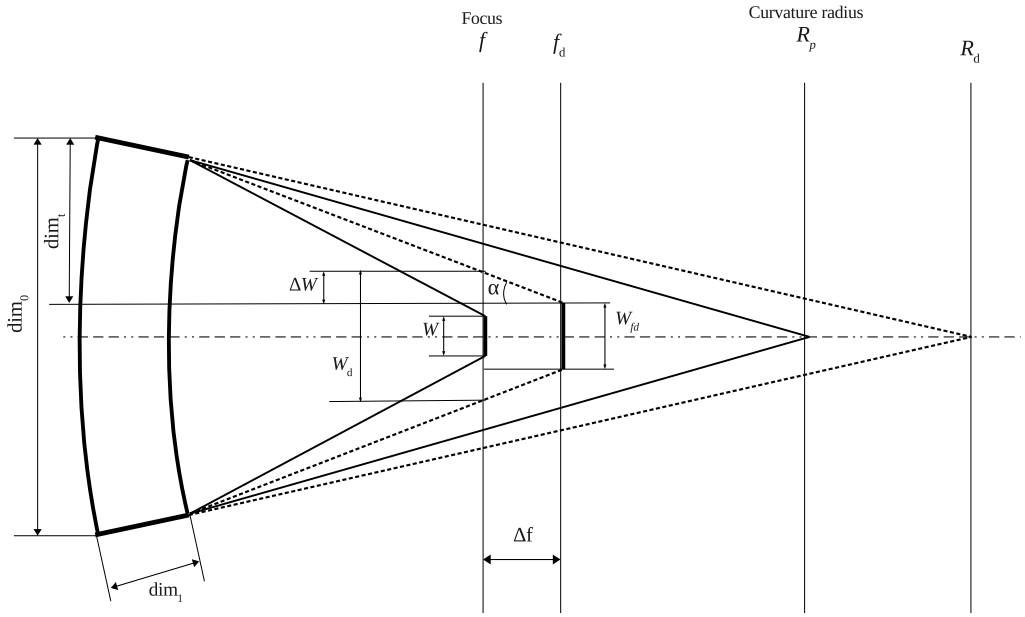

Figure 4.8: Diagram illustrating the effect of radial distortion of bent GaAs(220) crystal on the width of the PSF.

At f, the width W of the PSF is given by the angle β of the secondary curvature:

$$\beta = \frac{dim_1}{R_s}$$
$$W = f\beta$$

Similarly at f_d, the width W_{fd} is given by $W_{fd} = \beta_d f_d$. Where $\beta_d = \frac{dim_1}{R_{sd}}$. W_d is the width of this image that is formed on the detector on the focal plane at f. This can be derived as follows.

From Figure 4.9,

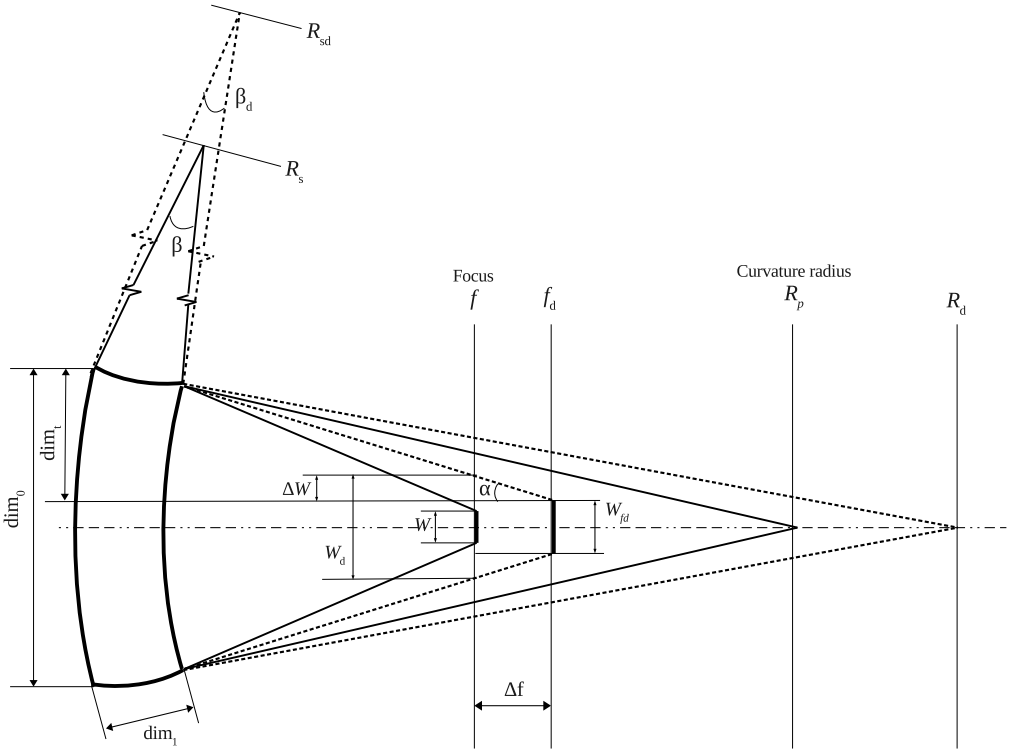

Figure 4.9: Diagram illustrating the effect of radial distortion of bent Ge(111) crystal on the width of the PSF.

$$dim_t = \frac{dim_0 - W_{fd}}{2}$$
$$\alpha = \frac{dim_t}{f_d}$$
$$\Delta f = |f_d - f|$$
$$\Delta W = \Delta f \alpha$$
$$W_d = W_{fd} + 2\Delta W$$

For the statistical approach in the code, the same methodology used for the misalignment effect has been adopted also for the radial distortion. The range of radial distortion is assumed to be uniformly distributed over all the crystals. For example, for a maximum radial distortion of 6 meters, the code incorporates this effect with a uniform distribution of the deviation of the radius in the range [0, 6) meters from the expected curvature radius of 40 meters.

4.3.1.3 Divergence of the beam

A Laue lens for astrophysical observations is built assuming that the incoming X-rays are parallel and paraxial. However, in laboratory, it is not possible to achieve this beam configuration given the finite distance between source and lens, and to the finite dimension of the source that has a radius of 0.4 mm. In order to minimize the beam divergence, a Tungsten bar 20 mm thick with a hole of 3 mm diameter and a lead bar 50 mm thick with a hole if 1 mm diameter are placed at the exit window of the X-ray source. The output beam, at a distance of 24.38 m, is further collimated with a second lead bar, which has in its center a Tungsten slit 20 mm thick with variable aperture S_w. After passing through this slit, the beam is incident on the crystal tile, which then diffracts and forms an image on the focal plane at a distance 20 meter from the crystal tile. The dependence of the FWHM of the PSF on the slit width S_w is plotted in Fig. 4.10.

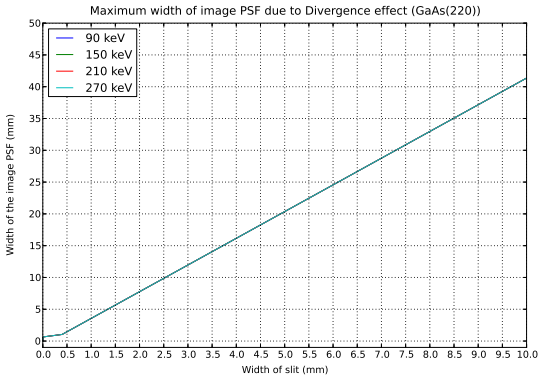

Figure 4.10: The effect of the divergence with the varying slit width (on the $x - axis$) on the FWHM of the image PSF.

4.4 Procedure followed in the code

The PSF of a lens is obtained from combining the reflectivity of each crystal used to build the lens/petal. This is the starting point of the simulation. The reflectivity profile of Ge(111) and GaAs(220) is calculated for an energy band from 80 keV to 600 keV. The next stage is the inclusion of different factors that deviate the PSF from its ideal behaviour. These are the misalignment in the positioning of the crystal and also the distortion in its curvature radius. These factors, including the input parameters are described in the following sections.

4.4.1 Reflectivity of the crystal

The reflectivity of a crystal depends on the energy of the beam as well as on the Bragg angle. The reflectivity of GaAs(220) as well as Ge(111) is calculated using Equations 2.18 and 2.25 respectively. Figure 4.11 shows the peak reflectivity of Ge(111) and GaAs(220) from 50 keV to 600 keV. Both crystals have a thickness of 2 mm.

This peak reflectivity is used to calculate the number of photons diffracted by the crystals in each ring of the lens or petal.

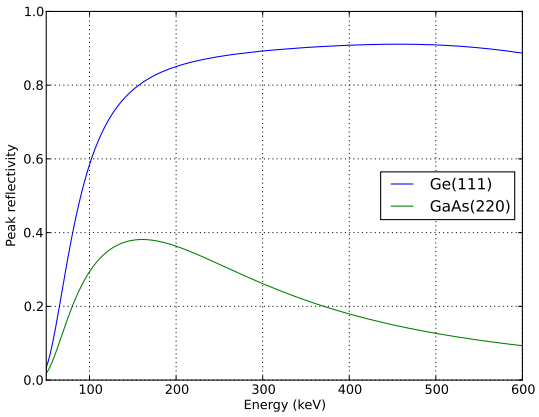

Figure 4.11: Peak reflectivity profile of Ge(111) and GaAs(220) with respect to energy (in keV).

4.4.2 Input parameters of the code

- Source: 10^6 photons/sec/area/keV;
- Focal length: 20 meters;
- Crystal dimension: 30 mm × 10 mm × 2 mm (*length* × *breadth* × *thickness*);
- Detector pixel size: 0.2 mm × 0.2 mm.

The selected thickness of 2 mm is the value which has been accepted for the tile thickness given that it is the maximum value of the crystal thickness that can be bend with the adopted technologies. The nominal value of the curvature radius of the crystal tiles is taken to be 40 meters.

4.5 Simulated output PSF of the Petal

The lens petal is made up of either Ge(111) or GaAs(220) crystal tiles. The energy band is from 90 keV to 300 keV. The same criteria adopted for simulating the PSF of the entire lens are also adopted for the petal. The difference being the energy band and the azimuth angle subtended by the petal to the center of the lens.

Fig.4.12 illustrates the position and angle of the lens petal and the corresponding PSF. The angle θ subtended by the lens petal gives a characteristic shape to the image.

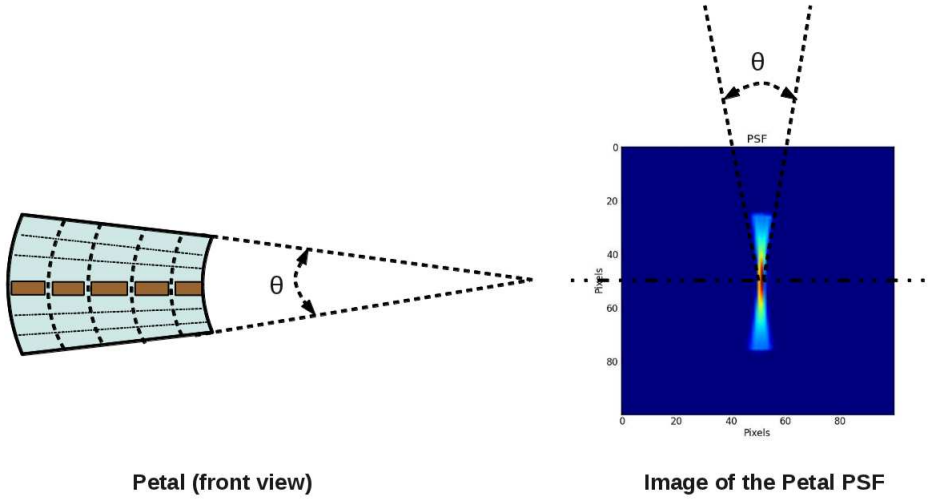

Figure 4.12: The angle θ subtended by the petal, $left$, results in an image, which will also subtend the same angle θ as shown on the $right$.

4.5.1 Petal made with GaAs(220)

This simulation of the petal (Fig.4.13, Fig.4.14, Fig.4.15 and Fig.4.16) consists of GaAs(220) as the crystal tiles. The energy band is from 89 keV to 308 keV. Ring-by-ring details of the petal have been given in Table.4.6. Different parameters of the petal and their corresponding values are given in Table.4.7.

Left panel of Fig.4.13, Fig.4.14, Fig.4.15 and Fig.4.16 shows the image of the PSF, while the right panel shows its 3D plot.

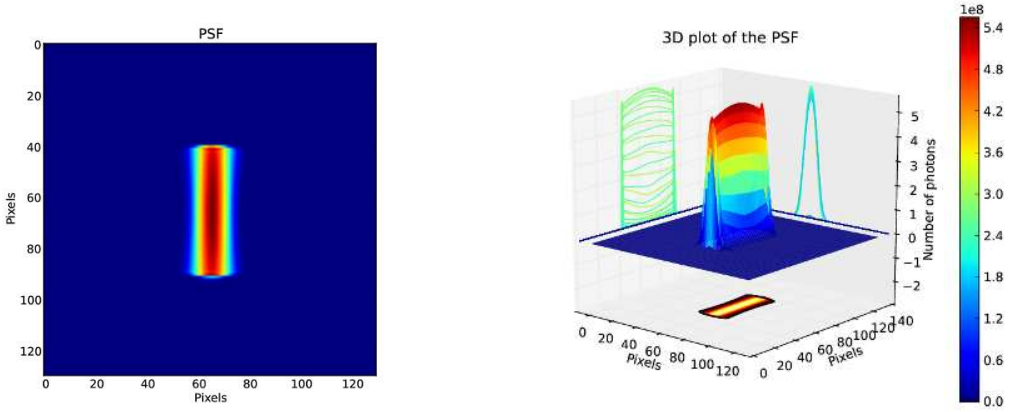

Figure 4.13: PSF of the petal made with GaAs(220) without any misalignment error in the positioning of the crystal tiles with no radial distortion.

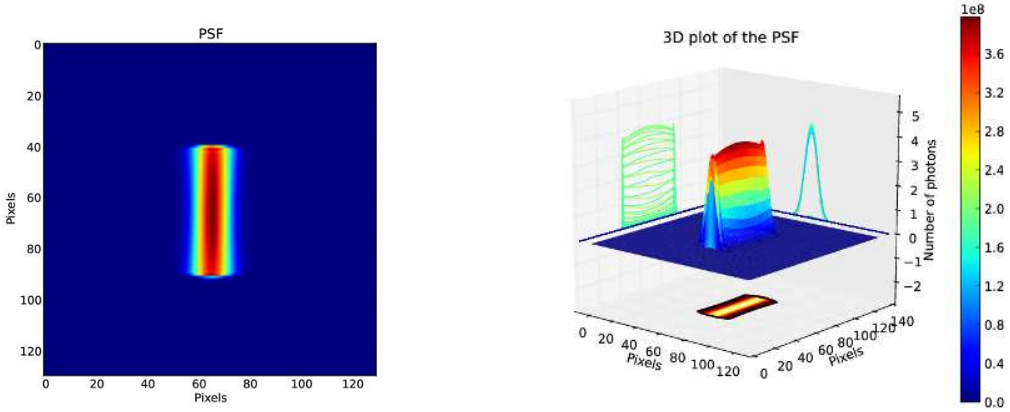

Figure 4.14: PSF of the petal made with GaAs(220) without any misalignment error in the positioning of the crystal tiles, with a radial distortion of 6 meters from the required 40 meters.

4.5.2 Petal made with Ge(111)

This simulation (Fig. 4.17, Fig. 4.18, Fig. 4.19 and Fig. 4.20), assumes a petal made of crystal tiles of Ge(111). Ring-by-ring details of the petal have been given in Table 4.8.

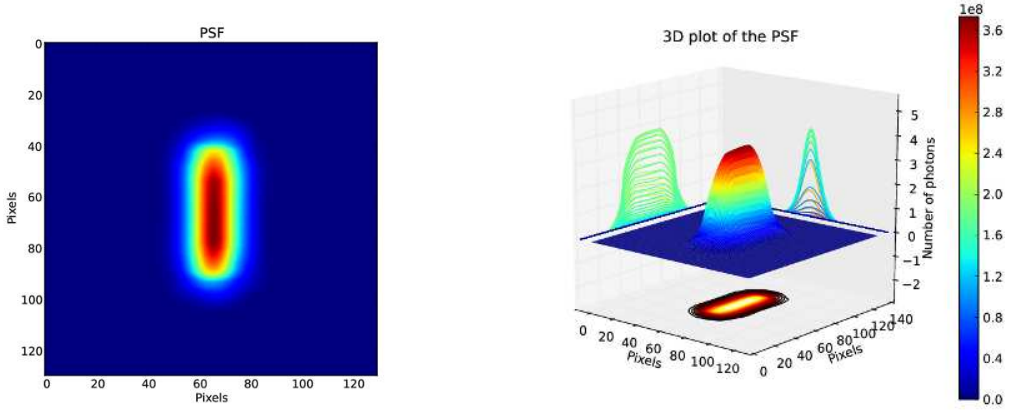

Figure 4.15: PSF of the petal made with GaAs(220) with a maximum misalignment of 30 arcsec in the positioning of the crystal tiles, with no radial distortion.

The different parameters and their corresponding values are given in Table 4.9.

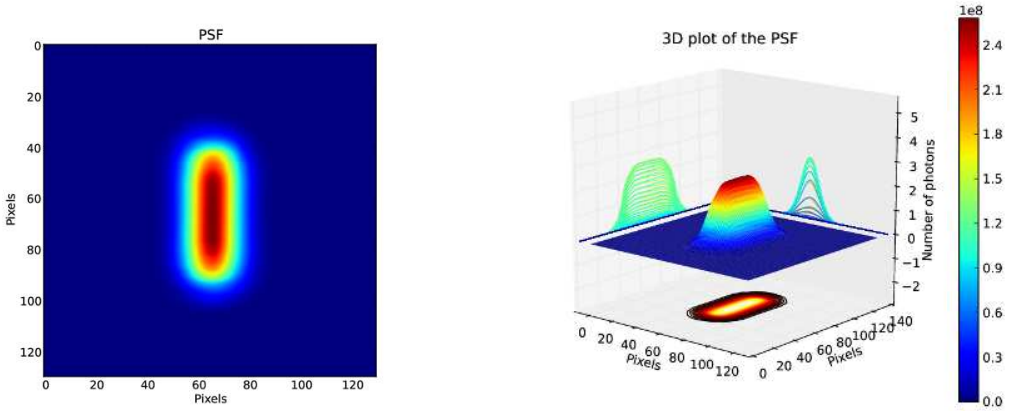

Figure 4.16: PSF of the petal made with GaAs(220) with a maximum misalignment of 30 arcsec in the positioning of the crystal tiles, and a maximum radial distortion of 6 meters from the required 40 meters.

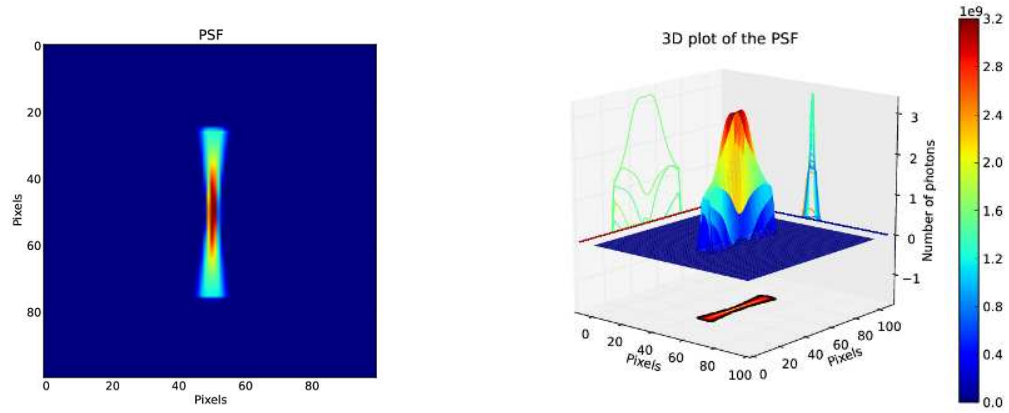

Figure 4.17: PSF of the petal made with Ge(111) without any misalignment errors and also without any radial distortion.

Table 4.6: Ring-by-ring analysis of the petal made by GaAs(220) crystal tiles.

Ring	Radius (cm)	No. of crystal tiles	Min. Energy (keV)	Max. Energy (keV)	Energy range (keV)
1	41.71	13	287.100	308.518	21.418
2	44.71	14	268.462	287.099	18.637
3	47.71	14	252.096	268.460	16.364
4	50.71	15	237.610	252.094	14.484
5	53.71	16	224.699	237.609	12.909
6	56.71	17	213.119	224.698	11.579
7	59.71	18	202.674	213.118	10.443
8	62.71	19	193.205	202.673	9.467
9	65.71	20	184.581	193.204	8.622
10	68.71	21	176.694	184.580	7.885
11	71.71	22	169.454	176.693	7.239
12	74.71	23	162.783	169.453	6.669
13	77.71	24	156.618	162.782	6.164
14	80.71	25	150.903	156.617	5.714
15	83.71	26	145.590	150.902	5.311
16	86.71	27	140.639	145.589	4.950
17	89.71	28	136.013	140.637	4.624
18	92.71	29	131.682	136.012	4.329
19	95.71	30	127.618	131.681	4.062
20	98.71	31	123.798	127.617	3.819
21	101.71	31	120.199	123.796	3.597
22	104.71	32	116.804	120.198	3.393
23	107.71	33	113.595	116.803	3.207
24	110.71	34	110.558	113.594	3.035
25	113.71	35	107.680	110.557	2.877
26	116.71	36	104.947	107.678	2.731
27	119.71	37	102.349	104.946	2.596
28	122.71	38	99.877	102.348	2.470
29	125.71	39	97.522	99.876	2.354
30	128.71	40	95.275	97.521	2.245
31	131.71	41	93.130	95.274	2.144
32	134.71	42	91.078	93.128	2.049
33	137.71	43	89.116	91.077	1.961

Table 4.7: Parameters of the petal made by GaAs(220) crystal tiles.

Parameter	Value
Focal length	20 meters
Energy range	89 - 308 keV
Subtended angle	18
No. of rings	33
Minimum radius	41.71 cm
Maximum radius	137.71 cm
No. of crystal tiles	913
Crystal material	GaAs(220)
Crystal dimension	30mm × 10mm × 2mm
Crystal mass (total)	2.5g × 913 = 2282.5 g

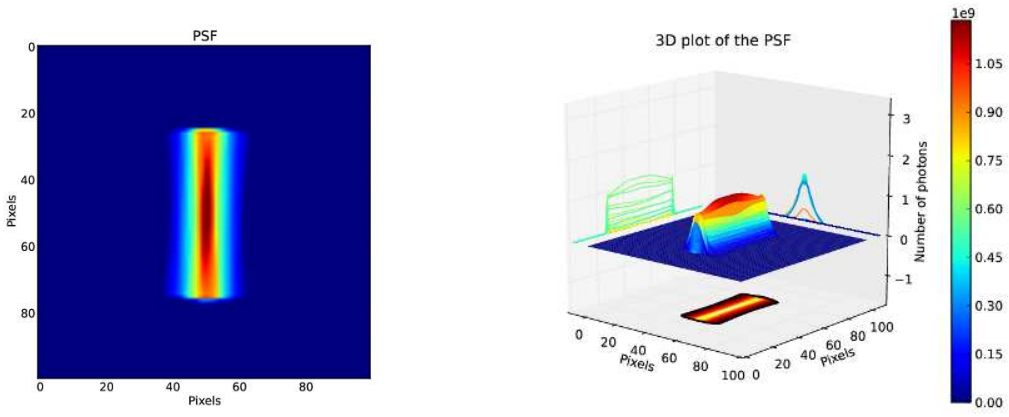

Figure 4.18: PSF of the petal made with Ge(111) without any misalignment errors but with a maximum radial distortion of 6 meters.

Table 4.8: Ring-by-ring parameters of the petal made by Ge(111) crystal tiles.

Ring	Radius (cm)	No. of crystal tiles	Min. Energy (keV)	Max. Energy (keV)	Energy range (keV)
1	27.673	8	260.222	290.047	29.825
2	30.673	9	235.958	260.221	24.263
3	33.673	10	215.833	235.957	20.124
4	36.673	11	198.871	215.833	16.961
5	39.673	12	184.381	198.871	14.489
6	42.673	13	171.859	184.381	12.521
7	45.673	14	160.930	171.859	10.928
8	48.673	15	151.308	160.929	9.621
9	51.673	16	142.771	151.307	8.535
10	54.673	17	135.146	142.770	7.624
11	57.673	18	128.295	135.146	6.850
12	60.673	19	122.104	128.294	6.189
13	63.673	20	116.484	122.104	5.619
14	66.673	20	111.358	116.483	5.125
15	69.673	21	106.664	111.357	4.693
16	72.673	22	102.350	106.663	4.313
17	75.673	23	98.3718	102.349	3.977
18	78.673	24	94.6909	98.371	3.680
19	81.673	25	91.2755	94.690	3.414
20	84.673	26	88.0979	91.274	3.176

Table 4.9: Parameters of the petal made by Ge(111) crystal tiles.

Parameter	Value
Focal length	20 meters
Energy range	88 - 290 keV
Subtended angle	18
No. of rings	20
Minimum radius	27.67 cm
Maximum radius	84.67 cm
No. of crystal tiles	343
Crystal material	Ge(111)
Crystal dimension	30 mm × 10 mm × 2 mm
Crystal mass (total)	2.07 gm × 343 = 710 gm

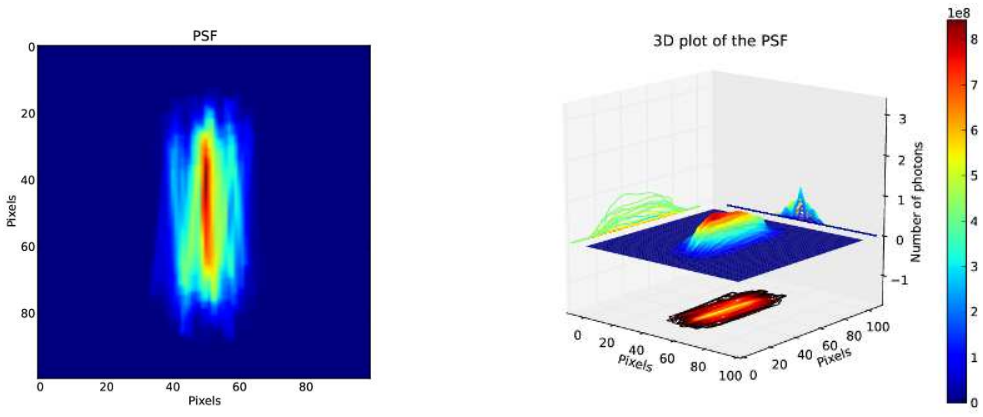

Figure 4.19: PSF of the petal made with Ge(111) with a maximum misalignment of 30 arcsec and without any radial distortion.

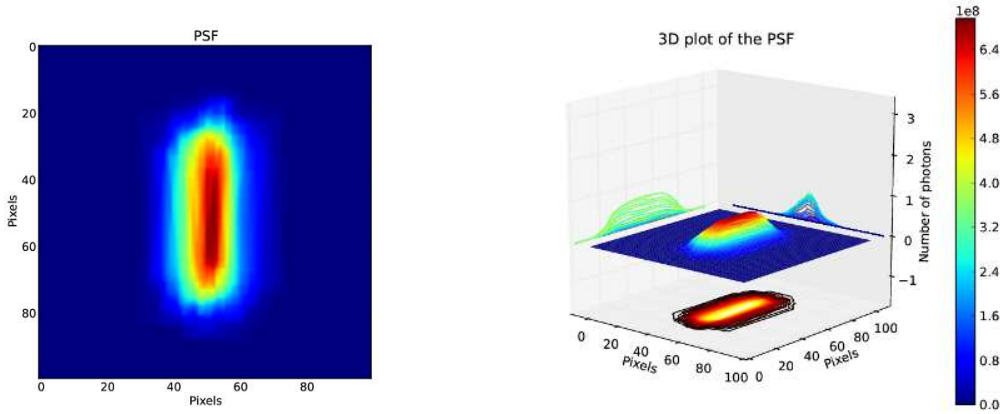

Figure 4.20: PSF of the petal made with Ge(111) with a maximum misalignment of 30 arcsec and with a maximum radial distortion of 6 meters.

4.6 Quantitative analysis of the simulated petal

This section deals with the analysis of the simulated petal made either with GaAs(220) or with Ge(111) crystal tiles. This analysis is significant for quantitatively and qualitatively comparing different outputs of the simulation.

4.6.1 Full Width at Half Maximum (FWHM) profile

Any misalignment in the positioning of the crystal on the petal frame and also any distortion in the curvature radius will affect the Full Width Half Maximum (FWHM) of the PSF. Figure 4.22 and 4.23 show the behaviour of FWHM of the PSF of the simulated petals described in section 4.5.1 and 4.5.2, as a function of the radial distortion. The radial distortion is plotted in the $x - axis$. Each value on the $x - axis$ corresponds to the maximum value of the uniformly distributed radial distortion. Each line in the plot corresponds to different misalignments in the positioning of the crystal tile.

The FWHM value of the petal PSF is obtained from the profile created by the histogram. Taking the photon counts over a horizontal section in the middle of the PSF forms this histogram profile. This is illustrated in Fig.4.21.

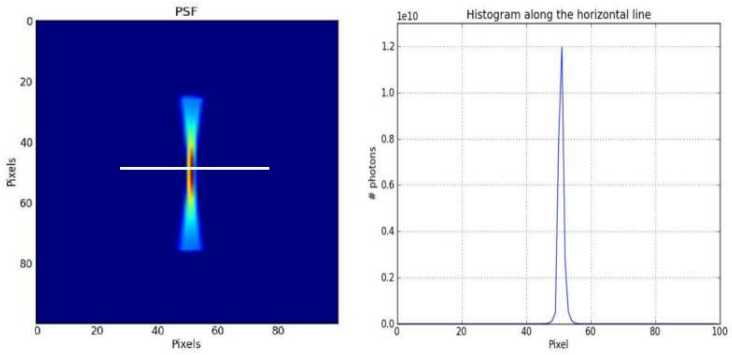

Figure 4.21: The curve on the *right* panel is obtained by taking into account the photons over the horizontal white line shown in the *left* panel. FWHM of this profile is then calculated and compared with the similar profiles for all PSFs.

As can be seen from Fig.4.22 and Fig.4.23, the FWHM of the PSF increases with the misalignment value as well as with the radial distortion. When there is no misalignment and no radial distortion, that is, when the lens is build perfectly without any errors, the FWHM is 2.76 mm in the case of the petal made with GaAs(220) and 0.56 mm in the case of Ge(111).

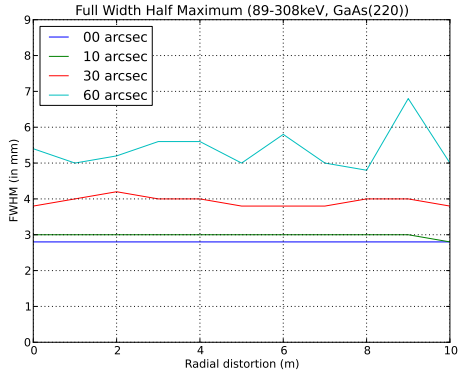

Figure 4.22: FWHM profile of the petal made with GaAs(220) for different values of the crystal misalignment and radial distortion. The values in the *legend* show maximum misalignment (in arcsec) in the positioning of crystals.

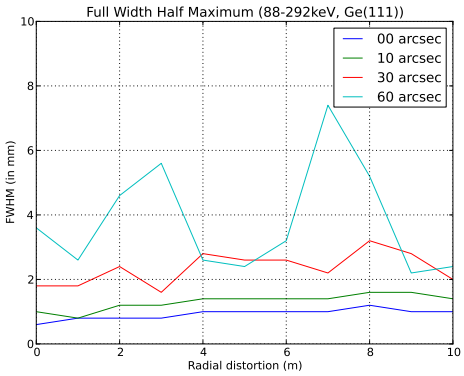

Figure 4.23: FWHM profile of the petal made with Ge(111) for different values of the crystal misalignment and radial distortion. The values in the *legend* show maximum misalignment (in arcsec) in the positioning of crystals.

4.6.2 Peak intensity profile

Any misalignment in the positioning of the crystal on the lens petal frame and also any distortion in the curvature radius will also affect the peak intensity of the PSF. This effect is plotted in Fig.4.24 and Fig.4.25. The peak intensity, as expected, gets reduced with the increase in misalignment of the crystal and radial distortion. The peak intensity of a perfect petal made of GaAs(220) without any misalignment or radial distortion gets reduced to 47% for a maximum misalignment of 30 arcsec and a maximum radial distortion of 6 meters. For a petal made with Ge(111) the corresponding value is 16%. This is also

evident from Fig.4.13, Fig.4.16, Fig.4.17 and Fig.4.20.

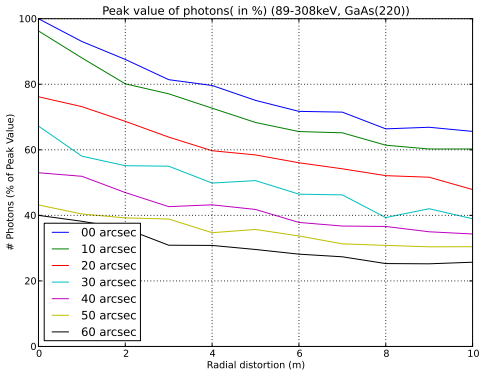

Figure 4.24: Peak intensity profile of the petal made with GaAs(220) for different values of crystal misalignment and radial distortion. The values in the *legend* give maximum misalignment (in arcsec) in the positioning of crystals.

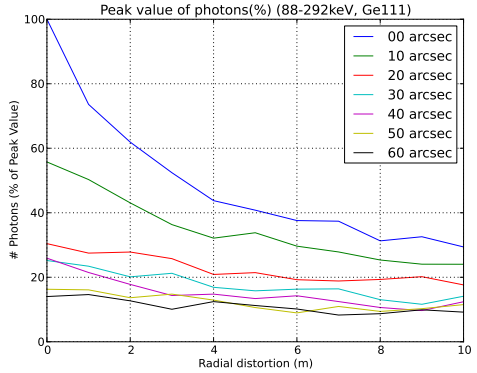

Figure 4.25: Peak intensity profile of the petal made with Ge(111) for different values of crystal misalignment and radial distortion. The values in the *legend* give maximum misalignment (in arcsec) in the crystal positioning.

4.7 Conclusion

The crystals that are used for the lens petal under construction, are a combination of bent perfect crystals of Ge(111) and bent mosaic crystals of GaAs(220). The quasi–mosaicity of Ge(111) is 4 arcsec, while the GaAs mosaicity is about 25 arcsec. The advantage of bent crystals is their better focusing capabilities. The crystal cross section has been chosen to be 30×10 mm^2, with the longer side radially placed on the lens frame. The main advantages of the rectangular shape, together with the radial disposition, concerns the focusing effect provided by bent crystals, which only acts in the radial direction. In such a way, a shorter width provides a smaller defocusing factor, being proportional to the tile size. On the other hand, a bigger radial dimension allows to decrease the total number of crystals, reducing the error budget potentially caused by each crystal misalignment contribution. The thickness t of the crystal tiles is 2 mm for both crystal materials. The thickness value is imposed by the current status of the bending technology adopted for bending Ge and GaAs.

The petal frame is designed in such a way that the passband of energy diffracted by the lens petal is from 90 to 300 keV. The dimensions of the petal frame is such that it will fit perfectly within the cross section of the beamline. The PSF for the petal has been simulated. The main factors that effect the PSF are the misalignment in the positioning of the crystal tile on the petal frame and the distortion in the curvature radius of the crystal tile from the required radius of 40 meters. Both these factors has been taken into account for the simulation.

It has been found that radial distortion causes a smooth enlarging of the PSF. This is evident from Fig.4.14 and Fig.4.18. On the other hand, misalignment effect also causes an enlargement of the PSF, but in an uneven way. This can be seen from Fig.4.15 and Fig.4.19. Thus, both these factors enlarge the FWHM of the PSF. The peak intensity is also affected by these distortions. There is a drastic decrease in the peak intensity of the PSF with the increase in both misalignment in the positioning of the crystal tiles and the distortion in curvature radius.

Chapter 5

Modelling and simulation of the Lens with results

This Chapter deals with the simulation of the entire lens by extending the algorithm developed for the petal. Here I will also discuss about the quantitative as well as qualitative analysis of the lens.

5.1 Introduction

The method to simulate the PSF of the petal is extended to model the entire lens. The simulation consists of lens separately made with GaAs(220) and Ge(111) crystal tiles.

As described in Chapter 4, the main type of errors that has been incorporated in the code are the misalignment in the positioning of the crystal tiles on the lens frame and also the radial distortion from the required curvature radius of 40 meters, that the crystal tile may show.

5.2 Simulating the entire Laue lens

The simulation of the entire Laue lens provides the PSF for on–axis photons. It takes into account
– the ideal case (Without any distortions and misalignment)
– different values of misalignment (in arcsec) in the positioning of the crystal tile on the lens frame and radial distortions (in meters) from the required curvature radius of 40 meters.

This will hep us in determining the acceptable level of distortion to get a reasonable PSF.

5.2.1 Lens made with GaAs(220)

A lens made only of GaAs(220) crystal tiles has been simulated. Ring-by-ring details of the lens have been given in Table 5.1. The lens parameters and their corresponding values are given in Table 5.2.

Table 5.1: Ring-by-ring features of the lens made by GaAs(220) crystal tiles.

Ring	Radius (cm)	No. of crystal tiles	Min. Energy (keV)	Max. Energy (keV)	Energy range (keV)
1	20.710	130	558.547	645.769	87.222
2	23.710	148	492.082	558.546	66.463
3	26.710	167	439.753	492.081	52.327
4	29.710	186	397.484	439.752	42.267
5	32.710	205	362.628	397.483	34.854
6	35.710	224	333.393	362.627	29.234
7	38.710	243	308.520	333.392	24.872
8	41.710	262	287.100	308.518	21.418
9	44.710	280	268.462	287.099	18.637
10	47.710	299	252.096	268.460	16.364
11	50.710	318	237.610	252.094	14.484
12	53.710	337	224.699	237.609	12.909
13	56.710	356	213.119	224.698	11.579
14	59.710	375	202.674	213.118	10.443
15	62.710	394	193.205	202.673	9.467
16	65.710	412	184.581	193.204	8.622
17	68.710	431	176.694	184.580	7.885
18	71.710	450	169.454	176.693	7.239
19	74.710	469	162.783	169.453	6.669
20	77.710	488	156.618	162.782	6.164
21	80.710	507	150.903	156.617	5.714
22	83.710	525	145.590	150.902	5.311
23	86.710	544	140.639	145.589	4.950
24	89.710	563	136.013	140.637	4.624
25	92.710	582	131.682	136.012	4.329
26	95.710	601	127.618	131.681	4.062
27	98.710	620	123.798	127.617	3.819
28	101.710	639	120.199	123.796	3.597
29	104.710	657	116.804	120.198	3.393
30	107.710	676	113.595	116.803	3.207
31	110.710	695	110.558	113.594	3.035
32	113.710	714	107.680	110.557	2.877

33	116.710	733	104.947	107.678	2.731
34	119.710	752	102.349	104.946	2.596
35	122.710	771	99.877	102.348	2.470
36	125.710	789	97.522	99.876	2.354
37	128.710	808	95.275	97.521	2.245
38	131.710	827	93.130	95.274	2.144
39	134.710	846	91.078	93.128	2.049
40	137.710	865	89.116	91.077	1.961
41	140.710	884	87.236	89.114	1.878
42	143.710	902	85.433	87.235	1.801
43	146.710	921	83.704	85.432	1.728
44	149.710	940	82.043	83.703	1.659
45	152.710	959	80.447	82.042	1.594

Table 5.2: Parameters of the lens made by GaAs(220) crystal tiles.

Parameter	Value
Energy range	80 - 600 keV
Focal length	20 meters
No. of rings	45
Minimum radius	20.71 cm
Maximum radius	152.71 cm
No. of crystal tiles	24494
Crystal material	GaAs(220)
Crystal dimension	30 mm $\times$ 10 mm $\times$ 2 mm
Crystal mass (total)	2.5 g $\times$ 24494 = 61.235 kg

The simulation results are shown in Fig. 5.1, Fig. 5.2, Fig. 5.3 and Fig. 5.4. The energy band is from 80 keV to 600 keV. The *left* panels show the image of the PSF and the *right* panel show its 3D plot.

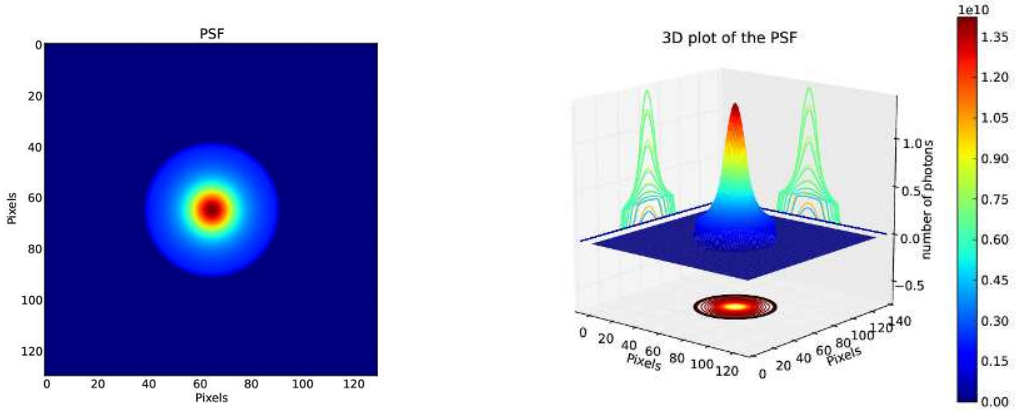

Figure 5.1: PSF of the lens made with GaAs(220) without any misalignment errors and also with no radial distortion.

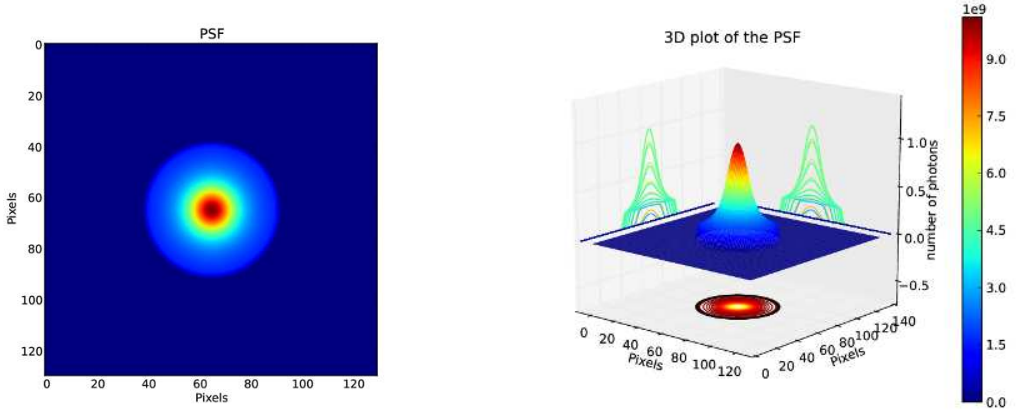

Figure 5.2: PSF of the lens made with GaAs(220) without any misalignment errors but with a maximum radial distortion of 6 meters.

5.2.2 Lens made with Ge(111)

Ring-by-ring details of the lens are given in Table 5.3. Different parameters and their corresponding values are given in Table 5.4.

The simulation results are shown in Fig. 5.5, Fig. 5.6, Fig. 5.7 and Fig. 5.8. The

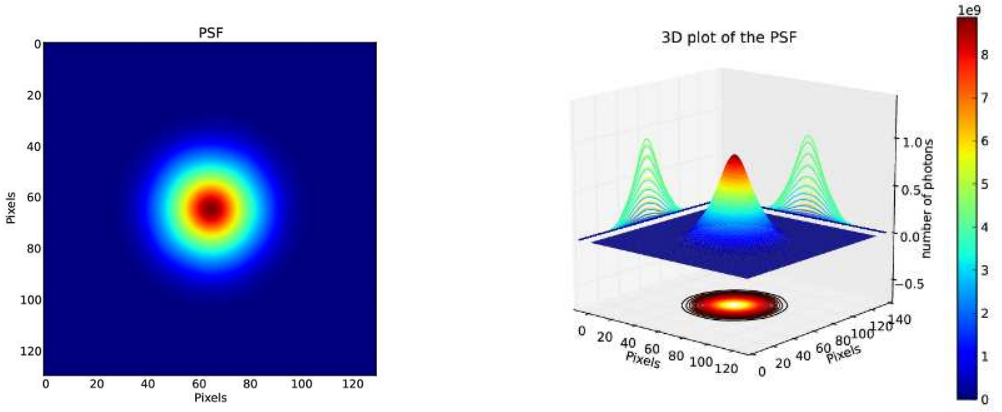

Figure 5.3: PSF of the lens made with GaAs(220) with a maximum misalignment of 30 arcsec and with no radial distortion.

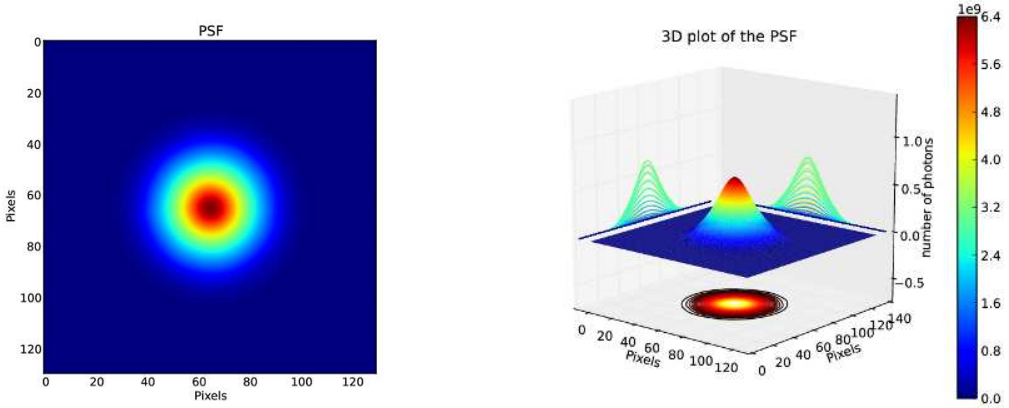

Figure 5.4: PSF of the lens made with GaAs(220) with a maximum misalignment of 30 arcsec and with a maximum radial distortion of 6 meters.

energy band is from 80 keV to 600 keV. The *left* panels show the image of the PSF, while the *right* panels show the 3D plot.

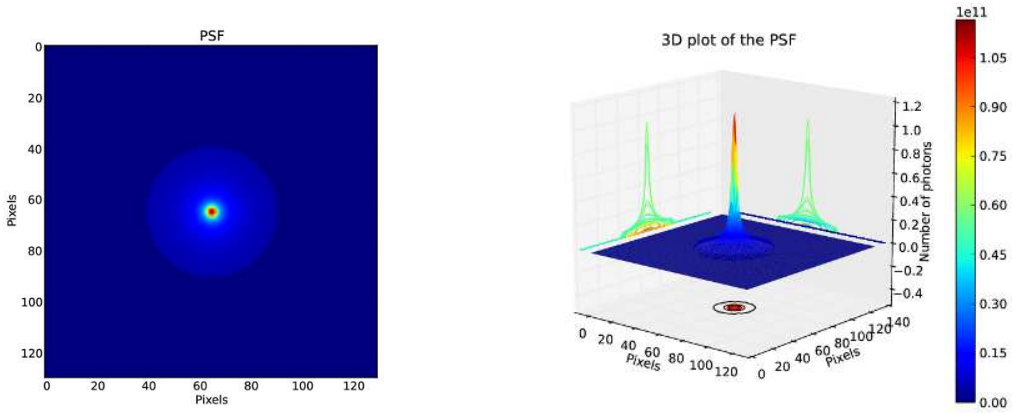

Figure 5.5: PSF of the lens made with Ge(111) without any misalignment errors and also with no radial distortion.

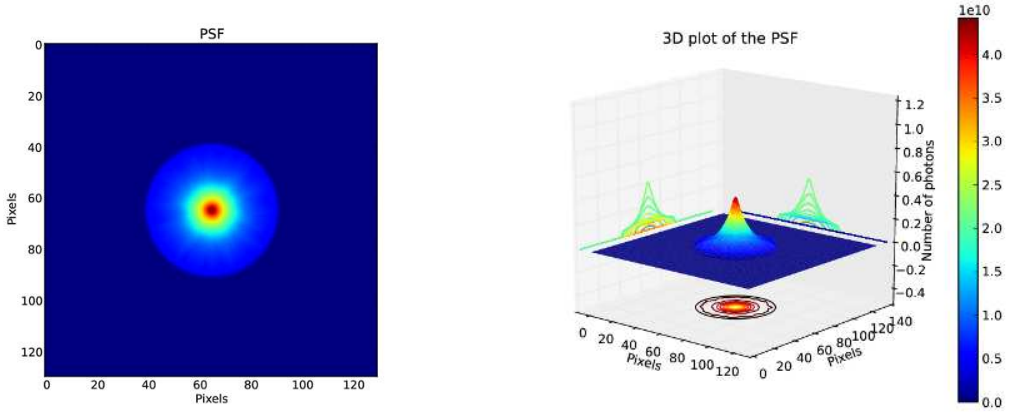

Figure 5.6: PSF of the lens made with Ge(111) without any misalignment errors but with a maximum radial distortion of 6 *meters*.

Table 5.3: Ring-by-ring analysis of the lens made by Ge(111) crystal tiles.

Ring	Radius (cm)	No. of crystal tiles	Min. Energy (keV)	Max. Energy (keV)	Energy range (keV)
1	12.673	79	535.609	679.409	143.799
2	15.673	98	442.047	535.608	93.560
3	18.673	117	376.312	442.047	65.734
4	21.673	136	327.596	376.311	48.714
5	24.673	155	290.048	327.596	37.547
6	27.673	173	260.222	290.047	29.825
7	30.673	192	235.958	260.221	24.263
8	33.673	211	215.833	235.957	20.124
9	36.673	230	198.871	215.833	16.961
10	39.673	249	184.381	198.871	14.489
11	42.673	268	171.859	184.381	12.521
12	45.673	286	160.930	171.859	10.928
13	48.673	305	151.308	160.929	9.621
14	51.673	324	142.771	151.307	8.535
15	54.673	343	135.146	142.770	7.624
16	57.673	362	128.295	135.146	6.850
17	60.673	381	122.104	128.294	6.189
18	63.673	400	116.484	122.104	5.619
19	66.673	418	111.358	116.483	5.125
20	69.673	437	106.664	111.357	4.693
21	72.673	456	102.350	106.663	4.313
22	75.673	475	98.371	102.349	3.977
23	78.673	494	94.690	98.371	3.680
24	81.673	513	91.275	94.690	3.414
25	84.673	532	88.097	91.274	3.176
26	87.673	550	85.134	88.097	2.963
27	90.673	569	82.363	85.133	2.770
28	93.673	588	79.767	82.362	2.595

Table 5.4: Parameters of the lens made by Ge(111) crystal tiles.

Parameter	Value
Focal length	20 meters
Energy range	80 - 600 keV
Subtended angle	18
No. of Rings	28
Minimum radius	12.67 cm
Maximum radius	93.67 cm
No. of crystal tiles	9341
Crystal material	Ge(111)
Crystal dimension	30 mm × 10 mm × 2 mm
Crystal mass (total)	2.07 g × 9341 = 19.335 kg

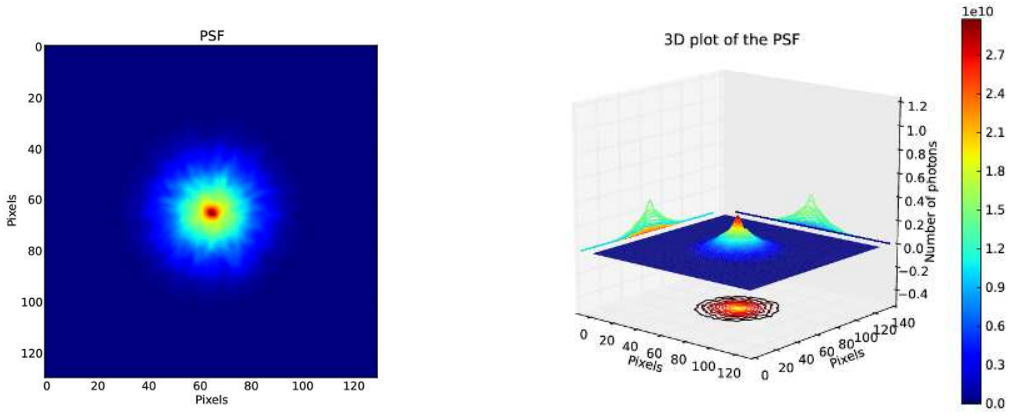

Figure 5.7: PSF of the lens made with Ge(111) with a maximum misalignment of 30 *arcsec* and without any radial distortion.

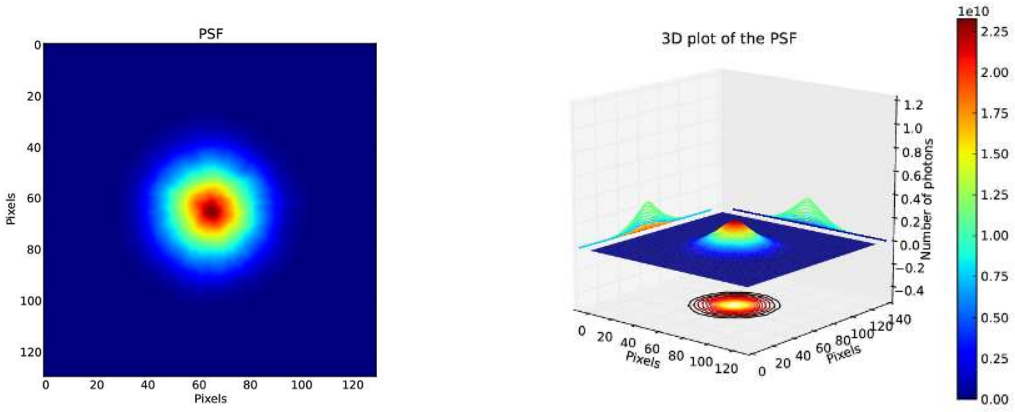

Figure 5.8: PSF of the lens made with Ge(111) with a maximum misalignment of 30 *arcsec* and with a maximum radial distortion of 6 *meters*.

5.3 Quantitative analysis of the simulation results

This section deals with the quantitative analysis of the results obtained from the simulations and their consequences. In particular we discuss the radial profile of the enclosed photons, the effective area, the continuum sensitivity and the line sensitivity of the entire lens.

5.3.1 Full Width at Half Maximum (FWHM) of the PSF

Any misalignment in the positioning of the crystal on the lens frame and also any distortion in the curvature radius affects the Full Width Half Maximum (FWHM) of the PSF. Figures 5.9 and 5.10 show the FWHM profiles of the simulated lens which was described in section 5.2.1 and 5.2.2. The radial distortion is plotted in the $x - axis$. Each value (in meters) on the $x - axis$ corresponds to the maximum value of the uniformly distributed radial distortion, $[0, x)$ meters, from the ideal radius of 40 meters. Each line in the plot represents the corresponding value of maximum misalignment in the positioning of the crystal tile (shown in the *legend box* of the plot).

As can be seen from Fig.5.9 and Fig.5.10, the FWHM of the PSF increases with the misalignment value as well as with the radial distortion. When there is no misalignment and no radial distortion, that is, when the lens is build perfectly without any errors, the FWHM is 3.4 mm in the case of the petal made with GaAs(220) and 0.6 mm for Ge(111) as the crystal tile.

5.3.2 Peak intensity profile

Any misalignment in the positioning of the crystal on the lens frame and also any distortion in the curvature radius from the required value of 40 meters will also affect the peak intensity of the PSF. This effect is plotted in Fig.5.11 and Fig.5.12. The peak intensity, as expected, gets reduced with the increase of the crystal misalignment and radial distortion. With respect to a perfect lens made of GaAs(220) without any misalignment or radial distortion, the peak intensity gets reduced to 45% for a maximum misalignment of 30 arcsec and a maximum radial distortion of 6 meters. The corresponding peak intensity reduction of a lens made with Ge(111) is about 80%. This is also evident from Fig.5.1, Fig.5.4, Fig.5.5 and Fig.5.8.

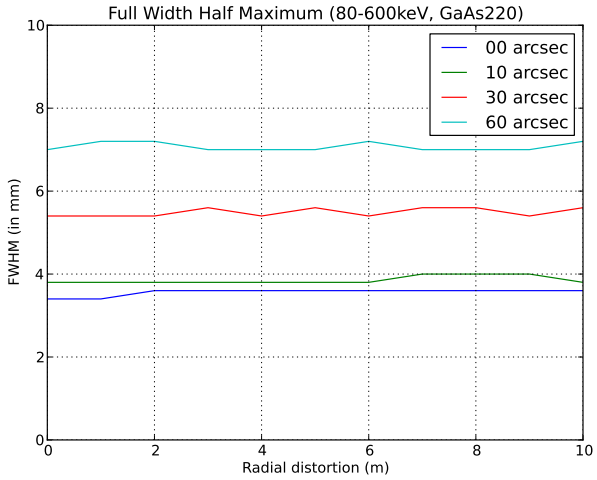

Figure 5.9: FWHM profile of the lens made with GaAs(220) for different values of crystal misalignment and radial distortion. The values in the *legend* show the maximum misalignment in the crystal positioning.

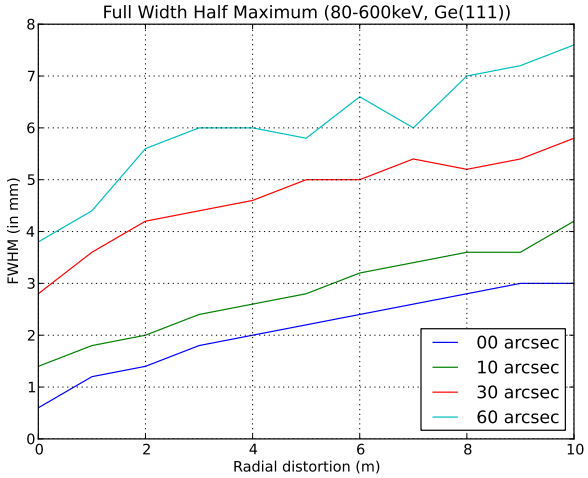

Figure 5.10: FWHM profile of the lens made with Ge(111) for different values of crystal misalignment and radial distortion. The values in the *legend* shows maximum misalignment (in *arcsec*) in the positioning of crystals.

5.3.3 Radial profile

The PSF radial profile is obtained by calculating the total photons radially enclosed outwards from the focal point of the PSF. The PSF profile of the lens made of GaAs(220)

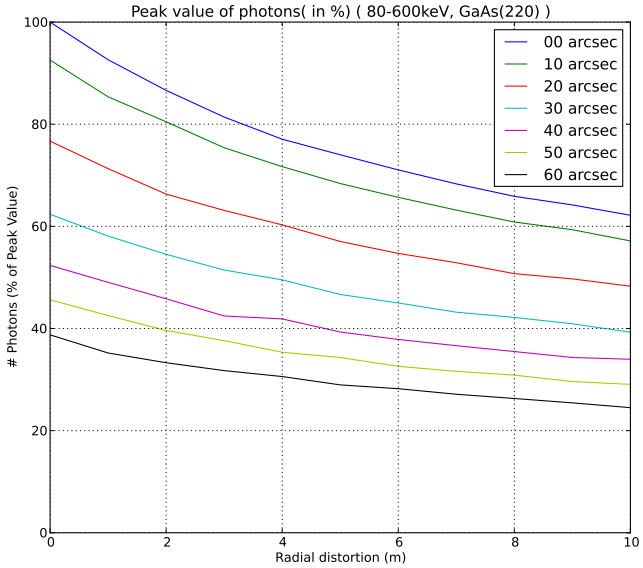

Figure 5.11: Peak intensity profile of the petal made with GaAs(220) for different values of crystal misalignment and radial distortion. The values in the *legend* shows maximum misalignment (in *arcsec*) in the crystal positioning.

or Ge(111) with perfect alignment of the crystal tiles and no radial distortion is shown in Figure 5.13.

As can be seen from Figure 5.13, the PSF if not a proper 'Gaussian', but has a 'trapezoidal' shape at the bottom. The normalised radial profile obtained is plotted in Figure 5.14. Corresponding values of the radius (in both pixels and in mm) for the enclosed % of the photons is given in the Table.5.5. The pixel dimension is 200 μm $\times$ 200 μm.

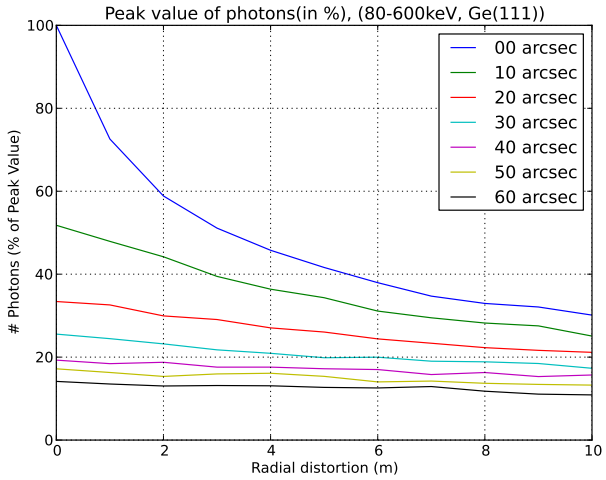

Figure 5.12: Peak intensity profile of the petal made with Ge(111) for different values of crystal misalignments and radial distortion. The values in the *legend* shows maximum misalignment (in *arcsec*) in the positioning of crystals.

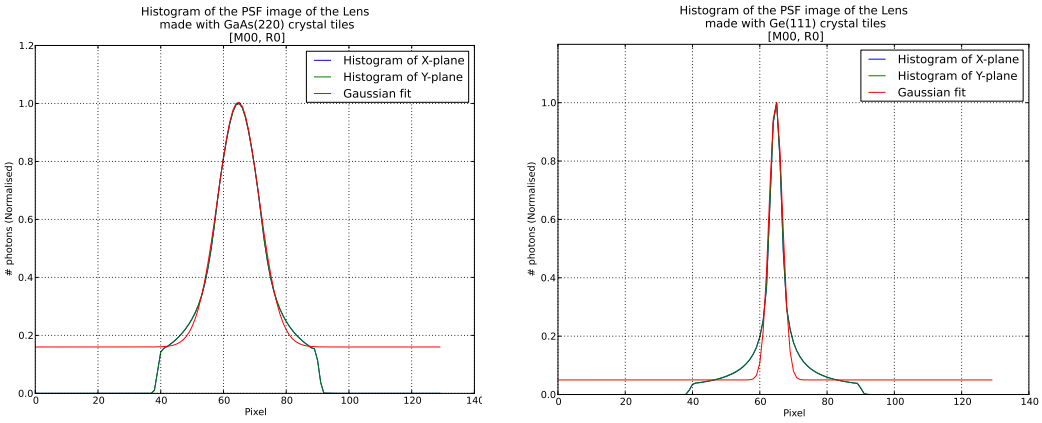

Figure 5.13: PSF profile of the lens made of crystal tiles of GaAs(220) (*left* panel) and Ge(111) (*right* panel). A perfect positioning of the crystal tiles and no radial distortions are assumed.

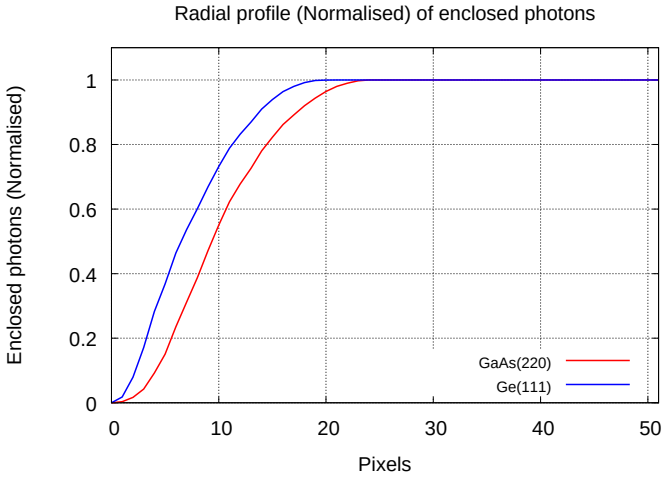

Figure 5.14: Normalised radial profile of the lens made with perfect positioning of the crystal tiles, having no radial distortions.

Table 5.5: Radial distribution of the enclosed photons of the lens made by the perfect positioning of the crystal tiles without any radial distortion.

Enclosed photons (%)	Radius			
	Lens with Ge(111)		Lens with GaAs(220)	
	(pixels)	(mm)	(pixels)	(mm)
10	3	0.6	5	1.0
20	4	0.8	6	1.2
30	5	1.0	7	1.4
40	6	1.2	9	1.8
50	7	1.4	10	2.0
60	8	1.6	11	2.2
70	10	2.0	13	2.6
80	12	2.4	15	3.0
90	14	2.8	18	3.6
100	20	4.0	24	4.8

5.3.4 Effective area

The effective area at an energy E is defined as the product of the geometrical area of the optics times its reflection efficiency at the same energy E. In the case of Laue lenses made of crystals, the effective area is the product of the geometric area of the crystals that reflect photons in a narrow energy interval ΔE around E $\left(E - \frac{\Delta E}{2} \leq E \leq E + \frac{\Delta E}{2}\right)$ times the mean reflection efficiency in this energy interval.

In our case, if the entire energy range (90-600 keV) of the lens is sub–divided into 10 equal bins (in logarithmic scale), the total geometric area in a given energy bin, GA^{bin}_{total}, is the total cross section of the crystals that reflect photons in the energy range of the bin.

For example, if E^{bin}_{min} and E^{bin}_{max} are respectively the minimum and maximum energy of a given bin, then the total geometric area GA^{bin}_{total}, in this energy bin is given by:

$$GA^{bin}_{total} = \pi(R^2_{max} - R^2_{min}) \tag{5.1}$$

where,

$$R_{max} = \frac{hcf}{d_{hkl}E^{bin}_{min}}$$
$$R_{min} = \frac{hcf}{d_{hkl}E^{bin}_{max}}$$

If $N_c(\Delta E)$ is the number of crystal tiles that reflect photons in a given energy bin, and $xtal_{area}$ is the surface area ($dim[0] \times dim[1]$) of a single crystal tile, then Eqn.5.1 can also be written as

$$GA^{bin}_{total} = N_c(\Delta E) \times xtal_{area} \tag{5.2}$$

Hence, in this method, the total geometric area GA^{bin}_{total}, does not depend upon the thickness as well as the mosaicity of the crystal tile.

The effective area $Area^{bin}_{eff}$, in a given energy bin is given by:

$$Area^{bin}_{eff} = GA^{bin}_{total} \times \overline{R_{bin}} \tag{5.3}$$

where $\overline{R_{bin}}$ is the mean reflectivity in that bin.

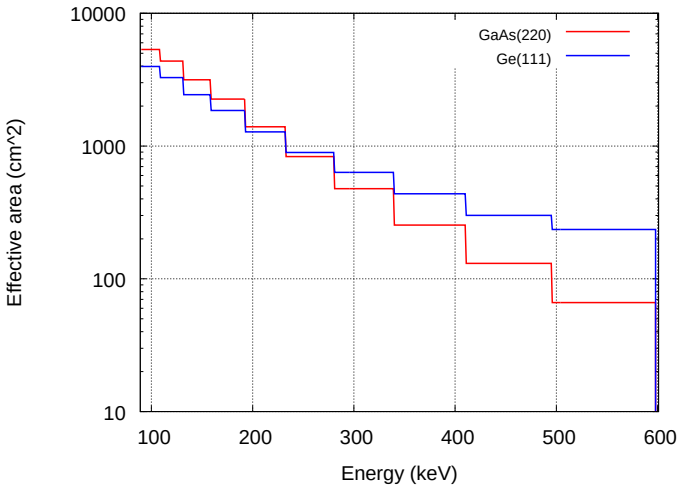

Figure 5.15: Effective area of the lens made of either GaAs(220) or Ge(111) crystal tiles calculated for 10 bins of logarithmically equal width.

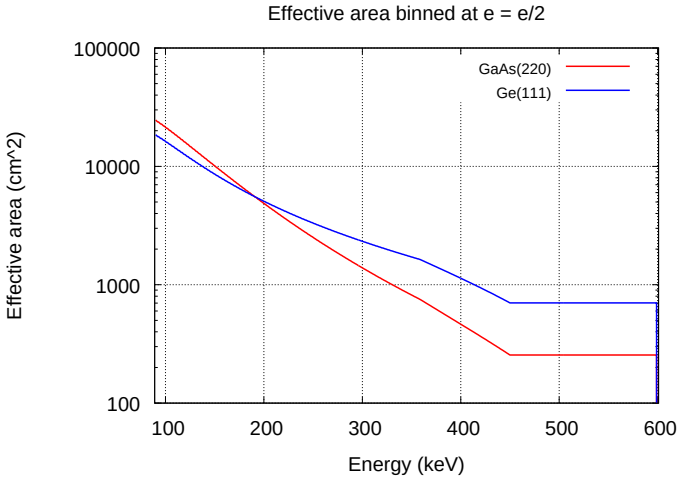

Figure 5.16: Effective area of the lens made of GaAs(220) as well as Ge(111) crystal tiles calculated for $\Delta E = E/2$.

Fig.5.15 and Fig.5.16 shows the effective area calculated as per Eqn.5.3. The large values of effective area at lower energies and smaller values at higher energies is due to the large difference in the number of crystal tiles corresponding to those energies. For example, the number of Ge(111) crystal tiles corresponding to lowest energy bin (in case of ΔE sub–divided into logarithmic 10 equal bins) are around 2092, but there are only

68 Ge(111) crystal tiles corresponding to the highest energy bin. For lens made with GaAs(220) crystal tiles there are 5580 tiles for the lowest energy range and 182 tiles for the highest energy range.

Table 5.6: The values of different parameters for each energy bin for the lens made with GaAs(220) crystal tiles.

Energy range (keV)	R_{max} (cm)	R_{min} (cm)	ΔR (cm)	GA^{bin}_{total} (cm^2)	$\overline{R_{bin}}$	$Area^{bin}_{eff}$ (cm^2)
90 – 109	137.84	113.81	24.02	18996.45	0.28872	5484.69
109 – 132	113.81	93.98	19.83	12946.36	0.34599	4479.33
132 – 159	93.98	78.02	15.95	8624.19	0.37574	3240.46
159 – 193	78.02	64.27	13.74	6144.92	0.37728	2318.37
193 – 233	64.27	53.24	11.03	4074.24	0.35183	1433.44
233 – 281	53.24	44.14	9.09	2782.81	0.30695	854.20
281 – 340	44.14	36.48	7.66	1940.78	0.25230	489.66
340 – 411	36.48	30.18	6.30	1320.26	0.19743	260.66
411 – 496	30.18	25.01	5.17	896.98	0.14918	133.82
496 – 599	25.01	20.71	4.30	617.78	0.10980	67.83

Table 5.6 and 5.7, respectively for GaAs(220) and Ge(111), give the values of different parameters that have been derived for the effective area calculation shown in Fig.5.15.

5.3.5 Continuum Sensitivity

Sensitivity of a telescope is defined as the minimum intensity, I_s^{min} which can be "detected" in an observation time T_{obs}.

For a focusing telescope, if the total noise measured is only due to the background along with the source, the sensitivity, $I_{ft}^{min}(E)$ is given by Eqn. 1.14 as:

$$I_{ft}^{min}(E) = n_\sigma \frac{\sqrt{B(E)}\sqrt{A_d}}{\eta_d f_\epsilon A_{eff}\sqrt{\Delta E}\sqrt{T_{obs}}}$$

where,

- n_σ is the number of σ, which gives a corresponding confidence level. (For e.g., 3σ corresponds to a confidence level of 99.7%);

Table 5.7: The values of different parameters for each energy bin for the lens made with Ge(111) crystal tiles.

Energy range (keV)	R_{max} (cm)	R_{min} (cm)	ΔR (cm)	GA^{bin}_{total} (cm^2)	$\overline{R_{bin}}$	$Area^{bin}_{eff}$ (cm^2)
90 – 109	84.35	69.64	14.70	7113.75	0.57394	4082.90
109 – 132	69.64	57.51	12.13	4848.13	0.69485	3368.75
132 – 159	57.51	47.74	9.76	3229.57	0.77453	2501.40
159 – 193	47.74	39.33	8.41	2301.14	0.82582	1900.32
193 – 233	39.33	32.58	6.75	1525.71	0.85862	1310.01
233 – 281	32.58	27.01	5.56	1042.1	0.87979	916.83
281 – 340	27.01	22.32	4.68	726.78	0.89458	650.16
340 – 411	22.32	18.47	3.85	494.4	0.90532	447.60
411 – 496	18.47	15.30	3.16	335.89	0.91055	305.85
496 – 599	15.30	12.67	2.63	231.34	0.90075	208.38

- $B(E)$ is the intensity of the measured background spectrum (in $counts/s/cm^2/keV$) at the energy E;
- η_d is the efficiency of the position sensitive detector;
- $A_d(= \pi R^2_{spot})$ is the part of the detector area which is covered by the incoming photons within a radius of R_{spot};
- ΔE is the energy band around E;
- T_{obs} is the observation time;
- f_ϵ is the fraction of photons that is focused on the detector area A_d;
- A_{eff} is the mean effective area in the energy band ; $\left(E - \frac{\Delta E}{2} \leq E \leq E + \frac{\Delta E}{2}\right)$ of the telescope optics, given by the product of the geometrical area of the optics in the same energy interval, times the reflection efficiency in the same energy band.

5.3.5.1 Variations with radial profile

A_d and f_ϵ are obtained from the radial profile data (See Fig.5.14 and Table 5.5) of the PSF. Hence these values also depend upon the offset angle of the source direction with respect to the axis of the telescope. For a given value of A_d, the continuum sensitivity (Eqn.1.14) of a focusing telescope becomes better for larger values of f_ϵ.

In Fig.5.17 and Fig.5.18 the effect of A_d and f_ϵ over the continuum sensitivity are plotted, respectively for lens made with GaAs(220) and Ge(111) crystal tiles. The values of R_{spot} and corresponding f_ϵ is as given in Table 5.5.

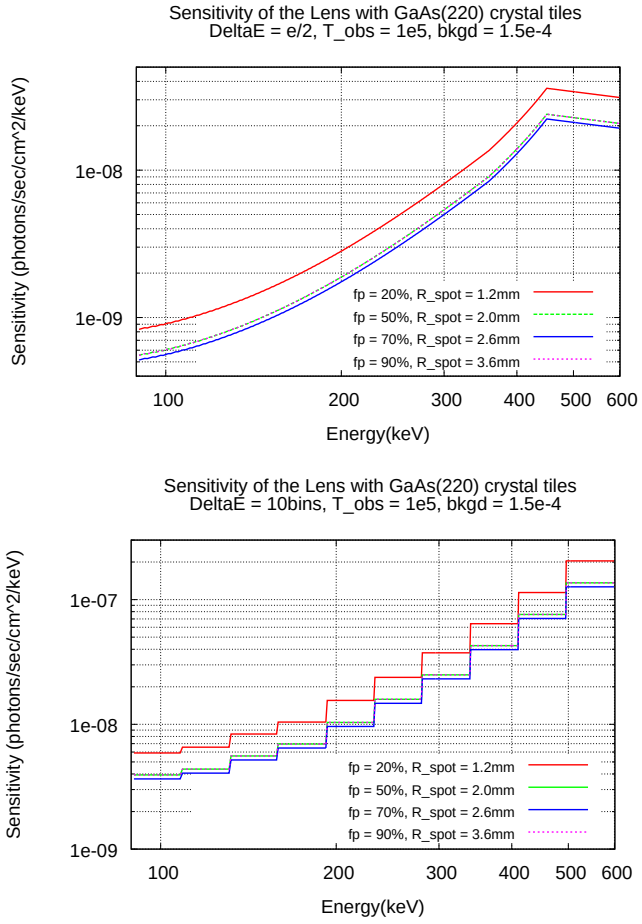

Figure 5.17: 3σ continuum sensitivity for an observation time of 10^5 seconds of the Lens made with GaAs(220) crystal tiles for various spot radii and corresponding fractions of enclosed photons (see Fig.5.14 and Table 5.5). *Top* panel: $\Delta E = E/2$ and *bottom* panel: $\Delta E = 10$ bins.

5.3.5.2 Impact of background on the lens sensitivity

Background noise is a strong factor deciding the level of continuum sensitivity. The background (in counts/s/cm^2/keV) measured by two different instruments on-board INTEGRAL satellite - the Integral Soft Gamma-Ray Imager (ISGRI) and SPectrometer for INTEGRAL (SPI) – has been assumed to analyse its effect on continuum sensitivity.

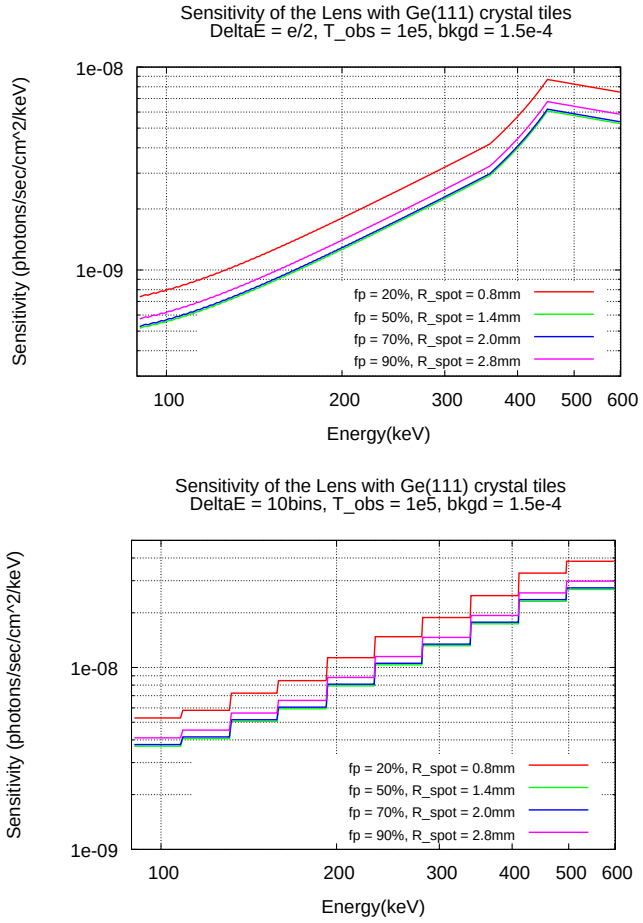

Figure 5.18: 3σ continuum sensitivity for an observation time of 10^5 seconds of the Lens made with Ge(111) crystal tiles for various spot radii and corresponding fractions of enclosed photons (see Fig.5.14 and Table 5.5). *Top* panel: $\Delta E = E/2$ and *bottom* panel: $\Delta E = 10$ bins.

ISGRI is a tungsten coded-aperture mask instrument made of CdTe (Cadmium Telluride) pixels, with about 2600 cm^2 of geometric area, which detects low energy Gamma rays in the energy band 15 keV - 10 MeV. SPI is made up of 19 hexagonal high purity germanium detectors and has an energy range of 18 keV - 8 MeV with total detection area of 500 cm^2. Also SPI has a hexagonal coded aperture mask. In addition, to reduce the background noise level, the detectors are almost completely shielded from the bottom up to the coded mask.

The background of these two instruments along with a constant background level of 1.5×10^{-4} $counts/s/cm^2/keV$ are plotted in Fig.5.19. For all further calculations,

the constant value of the background is assumed. The effect of the background on the continuum sensitivity is plotted in Fig.5.20, in the case of lens made with GaAs(220) crystal tiles and in Fig.5.21, in the case of lens made with Ge(111) crystal tiles .

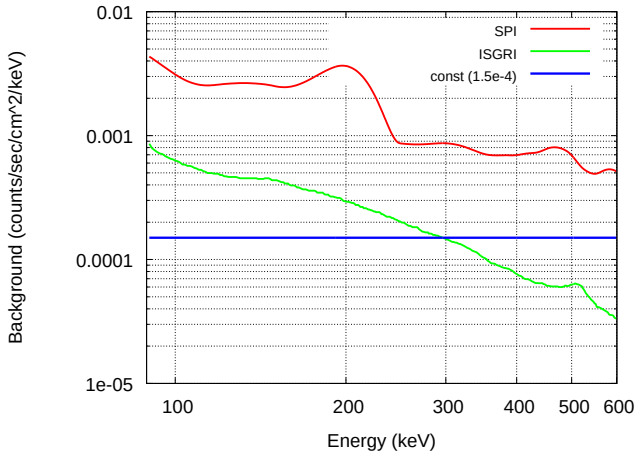

Figure 5.19: The background data that has been considered in calculating the lens continuum sensitivity shown in Fig.5.20 and Fig.5.21

5.3.5.3 Dependence of lens sensitivity on observation time

The continuum sensitivity is inversely proportional to the square root of the observation time, T_{obs} (Eqn. 1.14). Hence larger the observation time, better the value of sensitivity. Fig.5.22 shows the dependence of lens sensitivity on observation time (10^5 sec and 10^6 sec), in the case of $\Delta E = E/2$. Fig.5.23 corresponds to the same same dependence in the case of 10 bins equally logarithmically spaced.

From Table 5.8 and Table 5.9, it is seen that at 100 keV, the simulated lens (with both GaAs(220) as well as Ge(111)) is 4 orders of magnitude better than ISGRI as well as SPI at $\Delta E = E/2$. The data of ISGRI and SPI is taken from the reference [15] and [29] respectively. At about 511 keV, for a lens made with GaAs(220), the continuous sensitivity is 2 orders of magnitude better than ISGRI and 3 orders of magnitude better than SPI. At the same energy, for a lens made with Ge(111), the continuous sensitivity is 3 orders of magnitude better than ISGRI as well as SPI.

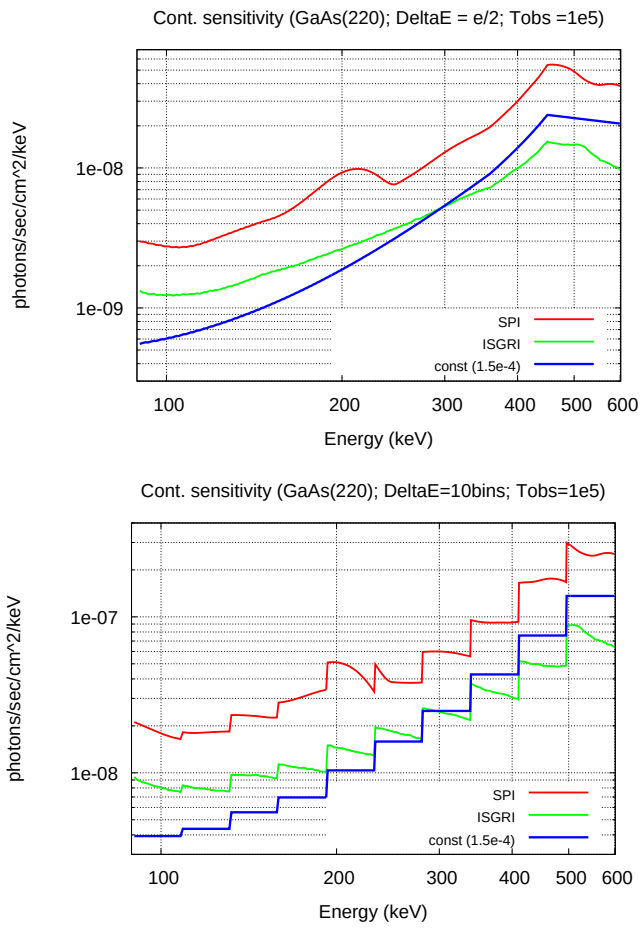

Figure 5.20: 3σ continuum sensitivity of a lens made with GaAs(220) crystal tiles for the various backgrounds levels shown in Fig.5.19. $\Delta E = E/2$ (*top* panel) and $\Delta E = 10$ bins (*bottom* panel). Observation time $= 10^5$ sec and R_{spot} = Half Power Radius (HPR).

5.3.6 Sensitivity to narrow emission lines

The sensitivity to narrow emission lines is derived by superposing the continuum source level to the emission line. In the case of a focusing telescope, if the source continuum level can be accurately determined, the minimum detectable intensity I_L^{min} (in $photons/s/cm^2$), of a line is given by Eqn. 1.25 as:

$$I_L^{min}(E_L) = 1.31 n_\sigma \frac{\sqrt{[2B(E_L)A_d + I_c(E_L)\eta_d f_\epsilon A_{eff}]\Delta E}}{\eta_d f_\epsilon A_{eff}\sqrt{T_{obs}}}$$

where,

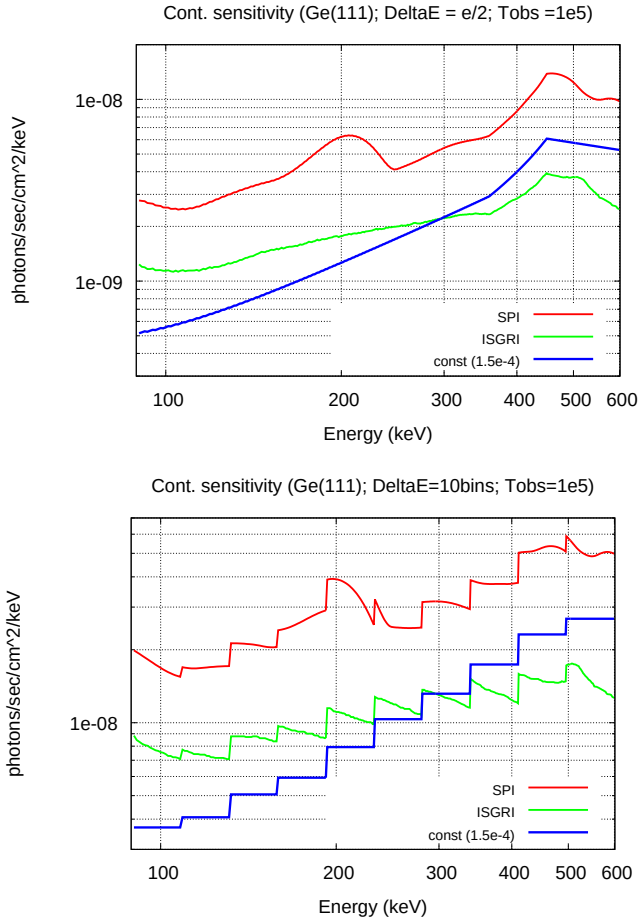

Figure 5.21: 3σ continuum sensitivity of a lens made with Ge(111) crystal tiles for the various backgrounds levels shown in Fig.5.19. $\Delta E = E/2$ (*top* panel) and $\Delta E = 10$ bins (*bottom* panel). Observation time $= 10^5$ sec and $R_{spot} =$ HPR.

- n_σ is the number of σ, which gives a corresponding confidence level. (For e.g., 3σ corresponds to a confidence level of 99.7%);
- $B(E_L)$ is the intensity of the measured background spectrum (in $counts/s/cm^2/keV$) at the energy E_L;
- $A_d(= \pi R^2_{spot})$ is the detector area covered by the incoming photons within a radius of R_{spot};
- $I_c(E_L)$ is the source continuum intensity (in $photons/s/cm^2/keV$) at the centroid of the line;
- η_d is the efficiency of the position sensitive detector;

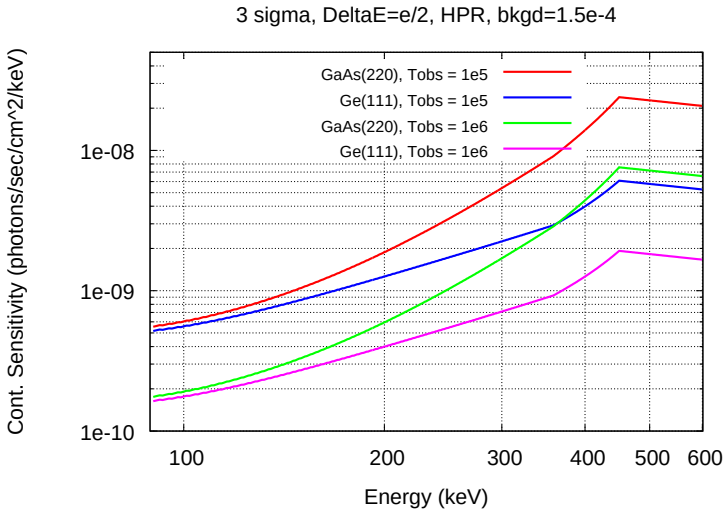

Figure 5.22: 3σ Continuum sensitivity of the lens with time of observation 10^5 seconds and 10^6 seconds with $\Delta E = e/2$, background $= 1.5 \times 10^{-4}$ and $R_{spot} =$ HPR.

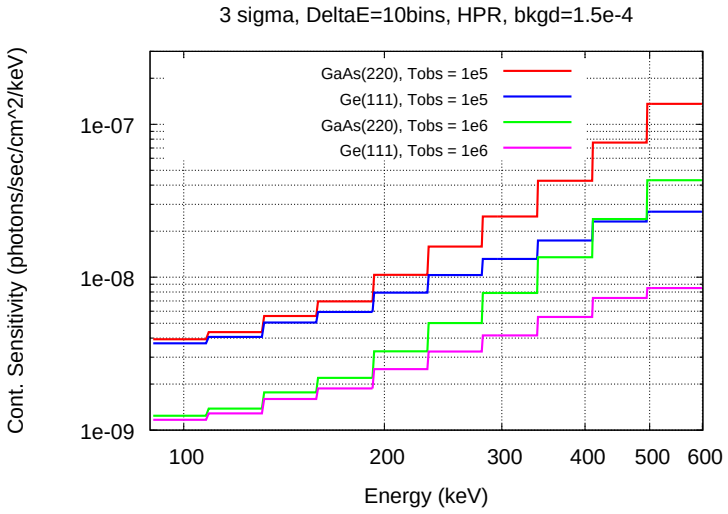

Figure 5.23: 3σ Continuum sensitivity of the lens with time of observation 10^5 seconds and 10^6 seconds with $\Delta E = 10$ bins, background $= 1.5 \times 10^{-4}$ and $R_{spot} =$ HPR.

- f_ϵ is the fraction of photons that is incident on the detector area A_d;

Table 5.8: 3σ continuum sensitivity (in photons/s/cm^2/keV) of the lens for observation times of 10^5 and 10^6 seconds and for $\Delta E = E/2$. These data are taken from the Fig. 5.22 and Fig. 5.23.

Energy	$Tobs = 10^5 sec$		$Tobs = 10^6 sec$	
(keV)	for GaAs(220)	for Ge(111)	for GaAs(220)	for Ge(111)
100	6.04×10^{-10}	5.57×10^{-10}	1.91×10^{-10}	1.76×10^{-10}
200	1.88×10^{-9}	1.26×10^{-9}	5.95×10^{-10}	4.00×10^{-10}
300	5.37×10^{-9}	2.24×10^{-9}	1.69×10^{-9}	7.09×10^{-10}
400	1.39×10^{-8}	3.99×10^{-9}	4.40×10^{-9}	1.26×10^{-9}
511	2.24×10^{-8}	5.76×10^{-9}	7.10×10^{-9}	1.80×10^{-9}

- ΔE is the FWHM of the line profile around E_L. This value also depends upon the energy resolution of the detector;
- T_{obs} is the observation time;
- A_{eff} is the telescope/lens effective area at an energy E_L, given by the product of the geometrical area of the optics times its reflection efficiency at that energy E_L;

The line sensitivity of a lens made of either GaAs(220) or Ge(111) with the crystal tiles perfectly positioned and with no radial distortion, is shown in Fig. 5.24. Each lens is plotted separately for 10^5 and 10^6 observation time. The values of the other parameters that intervene in the line sensitivity formula are the following: $n_\sigma = 3$, A_d (area corresponding to half power radius is given in Table 5.5, $\eta_d = 90\%$, $\Delta E = 2$ keV, which is the energy resolution of the CZT detector intended for our use, and finally A_{eff} corresponds to the data from Fig.5.16 with a filling factor of 0.2 mm.

From Table 5.10 and Table 5.11, it is seen that at about 100 keV, the simulated lens is 4 orders of magnitude better than ISGRI and SPI, and is 3 orders of magnitude better at 511 keV. Comparison is made for $T_{obs} = 10^6$ sec.

Table 5.9: 3σ continuum sensitivity (in photons/s/cm^2/keV) of ISGRI (observation time = 10^5 seconds) and SPI (observation time = 10^6 seconds), with $\Delta E = E/2$.

Energy (keV)	ISGRI ($T_{obs} = 10^5 sec$) (photons/s/cm^2/keV)	SPI ($T_{obs} = 10^6 sec$) (photons/s/cm^2/keV)
100	2.85×10^{-6}	7.0×10^{-6}
200	4.10×10^{-6}	–
300	6.02×10^{-6}	–
400	7.56×10^{-6}	–
500	9.83×10^{-6}	1.5×10^{-6}

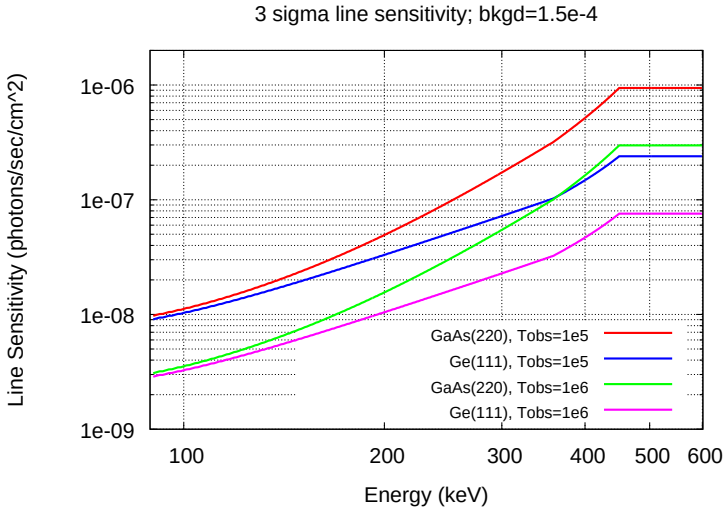

Figure 5.24: Line sensitivity of the lens considering a constant value for the background level (1.5×10^{-4}) and for 10^5 and 10^6 sec observation time (see *legend*).

5.4 Angular resolution

When a source moves off–axis, the effective area gets reduced and hence the sensitivity degrades. Hence its important to simulate the off–axis analysis of the lens. This provides better understanding of the angular resolution as well.

For obtaining the off–axis performance, Monte Carlo simulations has been done on

Table 5.10: 3σ line sensitivity (in photons/s/cm^2) of a lens with time of observation times of 10^5 and 10^6. These data are taken from Fig. 5.24.

Energy (keV)	$Tobs = 10^5 sec$		$Tobs = 10^6 sec$	
	for GaAs(220)	for Ge(111)	for GaAs(220)	for Ge(111)
100	1.11×10^{-8}	1.08×10^{-8}	3.53×10^{-9}	3.26×10^{-9}
200	4.93×10^{-8}	3.31×10^{-8}	1.56×10^{-8}	1.04×10^{-8}
300	1.72×10^{-7}	7.19×10^{-8}	5.45×10^{-8}	2.27×10^{-8}
400	5.16×10^{-7}	1.47×10^{-7}	1.63×10^{-7}	4.67×10^{-8}
511	9.41×10^{-7}	2.39×10^{-7}	2.97×10^{-7}	7.55×10^{-8}

Table 5.11: 3σ line sensitivity (in photons/s/cm^2) of ISGRI and of SPI (observation time = 10^6 seconds, $\Delta E = E/2$).

ISGRI		SPI	
Energy (keV)	Line sensitivity (photons/s/cm^2)	Energy (keV)	Line sensitivity (photons/s/cm^2)
112.9	1.67×10^{-5}	100	4.4×10^{-5}
225.4	3.21×10^{-5}	–	–
449.6	6.64×10^{-5}	–	–
566.1	8.40×10^{-5}	500	3.1×10^{-5}

the basis of ray tracing mechanism. For this, a spherical geometry of the lens is assumed, over which crystals of finite dimension (10 μm $\times$ 10 mm $\times$ 2 mm) has been positioned in order to focus the incoming photons within an energy band from 90 – 600 keV. The finite crystal tile is given the same mosaicity parameters as of GaAs(220) and Ge(111). This assumption takes care of the curvature of the individual crystal tiles of 30 $\times$ 10 $\times$ 2 mm^3 dimension.

Fig. 5.25 shows the off–axis analysis of the lens made by GaAs(220) bent mosaic crystals. Three simulations are compared. One, when the source is on–axis, and the other two, when the source is respectively 1 arcmin and 2 arcmin away from the axis of the lens. It can be seen that the angular resolution of this lens is more than 2 arcmin.

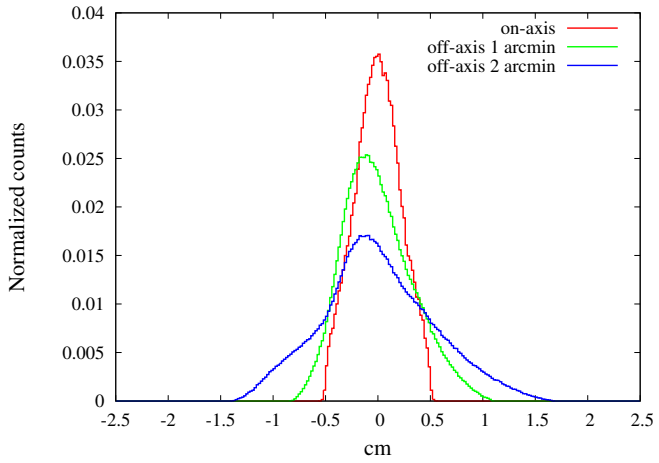

Figure 5.25: The off–axis analysis of the lens made with GaAs(220) bent mosaic crystals. The figure shows three plots corresponding to a source which is respectively, on–axis, 60 arcsec and 120 arcsec off–axis from the axis of the lens.

5.5 Conclusion

The code used for the simulation of the petal has been extended to model an entire lens made of petals. The on–axis performance of a simulated lens made of either GaAs(220) or Ge(111) crystal tiles has been presented. The effective area, the continuum sensitivity as well as the line sensitivity are calculated.

Any misalignment in the positioning of the crystal on the lens petal frame, and also any distortion in the curvature radius will affect the FWHM of the PSF. Figure 5.26 shows the dependence of FWHM on the radial distortion for the two lens cases, assuming a perfect positioning of the crystal tiles on the lens frame. As it can be seen, when there is no misalignment and no radial distortion, the FWHM is 3.4 mm in the case of GaAs(220) and 0.6 mm for Ge(111) as the crystal tile used for building the lens.

The sensitivity results show that this lens is 3 orders of magnitude more sensitive (see Table 5.8 and 5.9) than ISGRI [15] and SPI [29] on-board the INTEGRAL satellite. This is summarised in Table 5.12.

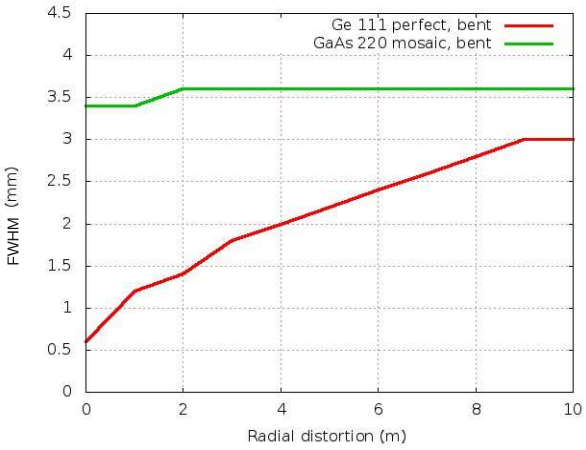

Figure 5.26: FWHM profile of the lens made with perfect positioning of the crystal tiles on the lens frame.

Table 5.12: Comparison of the 3σ continuum sensitivity (in photons/sec/cm^2/keV) of simulated lens with ISGRI and SPI on-board INTEGRAL for $\Delta E = E/2$.

Energy (keV)	Simulation ($T_{obs} = 10^5$s)		ISGRI	SPI
	GaAs(220)	Ge(111)	T_{obs}=10^5s	T_{obs}=10^6s
100	6.04×10^{-10}	5.57×10^{-10}	2.85×10^{-6}	7.0×10^{-6}
500	2.24×10^{-8}	5.76×10^{-9}	9.83×10^{-6}	1.5×10^{-6}

Chapter 6

Open astrophysical cases that can be settled by Laue lens

6.1 Introduction

Hard X-/soft gamma-ray astronomy is a crucial window for the study of the most energetic and violent events in the Universe. With the ESA INTEGRAL observatory, and the NASA Swift satellite, unprecedented sky surveys in the band beyond 20 keV are being performed. As a consequence, hundreds of celestial sources have already been discovered, new classes of Galactic sources are being identified, an overview of the extragalactic sky is available, while evidence of extended matter-antimatter annihilation emission from our Galactic center and of Galactic nucleo-synthesis processes have been also reported. However, in order to take full advantage of the extraordinary potential of soft gamma–ray astronomy, a new generation of telescopes is needed.

Nowadays the best comparison can be done with the continuum sensitivity (about 10^{-6} photons cm^{-2} s^{-1} keV^{-1} in 10^6 s) of the INTEGRAL/ISGRI coded-mask telescope [60] and with the emission line sensitivity (5×10^{-5} photons cm^{-2} s^{-1} in 10^6 s) of the INTEGRAL/SPI coded mask telescope [79]. For comparison, we note that the lens continuum and line sensitivity is at least a factor 300 better.

With this sensitivity figure, the source continuum spectra beyond 100 keV can be well determined. Indeed, while below 100 keV, the spectra of the brightest sources are well determined and, in the future, those of fainter sources will be determined with *NuSTAR*, above 100 keV very little is known on the spectral energy distribution of Galactic and extragalactic sources (see two examples in Fig. 6.1). With the proposed Laue lens we expect to open a new energy window and deal with many still open issues in addition to have the possibility of making unexpected discoveries.

Here I will mention some of the open issues that can be solved only with these un-

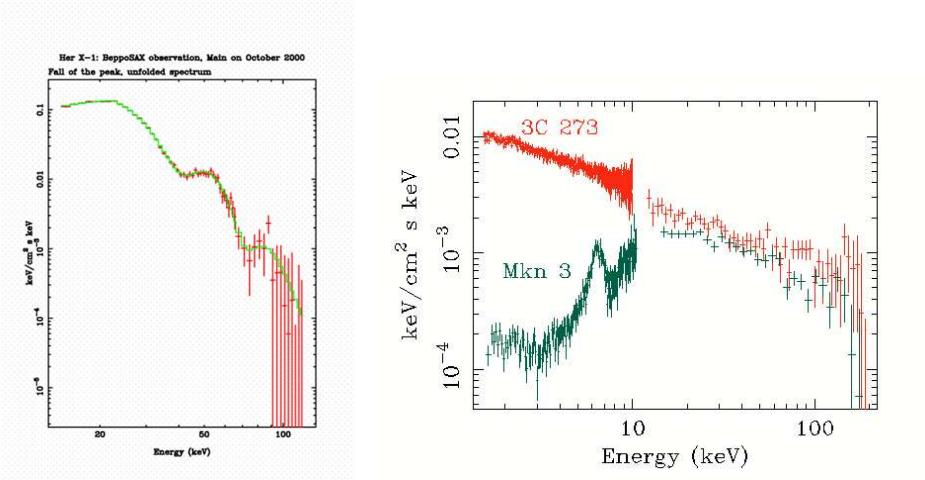

Figure 6.1: The broad band measured spectra of the Galactic X–ray pulsar Her X–1 (*left*) and of the extragalactic Active Galactic Nuclei (AGN) MKN–3 (Seyfert 2 galaxy) and 3C273 (quasar). In the case of Her X–1, the spectrum is well determined only up to 60 keV.

precedented observations beyond 100 keV.

6.2 Physics of accretion onto Galactic compact objects in binary systems

The spectra of the Galactic compact sources (White Dwarfs, Neutron Stars or Black Holes) in binary systems extend from soft X–rays to beyond 100 keV. However, their knowledge beyond 100 keV (or less, see, e.g., Fig. 6.1) requires much more sensitivity than that achieved by satellite missions like *BeppoSAX*, *Rossi–XTE*, and *INTEGRAL*. The results obtained so far clearly show that only a broad energy band that extends beyond 100 keV allows to establish the main physical components in the spectra and to study their origin. For example, in the case of X–ray pulsars, either high energy cyclotron scattering features or harmonics of lower energy features can be discovered, and thus the magnetic field strength and its properties can be investigated.

One of the most interesting and debated topics is the origin of the transient powerlaw-like X-ray tail which was observed above 30 keV in some low-magnetic field NS low-mass X-ray binaries (Z and atoll bursting sources, transient sources). Satellites which observed this feature (BeppoSAX, RXTE, Suzaku, Integral) [81, 20, 80, 66], revealed only the "on" and "off" states, but nothing could be said about possible variations of the

powerlaw spectral index and, most importantly, the position of the high-energy cutoff [70]. At present, models such as hybrid non-thermal Comptonization [27], bulk motion Comptonization [28] or even synchrotron emission [69] can adequately fit the data.

Only with a Laue lens telescope will be possible to thoroughly observe the hard tail evolution and find the position of the high-energy cut-off which would set unambigous constraints on the physical mechanism responsible for the emission.

The physical mechanisms responsible for the production of non-thermal emission in accreting BHs has been demonstrated to reside in the observational appearances of the power-law tails in the X-ray spectra from these objects and their behavior in different spectral states vs. corresponding photon index [88, 58]. The cutoff energies, which can be currently measured at most during the outburst peak of the strongest BH transient sources (see, e.g., Fig. 6.2), is generally below the sensitivity limits or outside the passband of the current instrumentation, in the case of weak sources. Only the use of Laue lenses will fully address this issue for a complete sample of BH sources.

It has been argued [59] that, very close to the event horizon, X-ray photons may be upscattered by bulk electrons to MeV energies. Most of these photons fall down then in the black hole, but some of them have time to interact anyway with another X-ray photon due to the photon-photon process, thus making an electron-positron pair. This pair creation process close to horizon can give rise to a gravitationally or not redshifted positron annihilation line. The study of this line can be carried out only through focusing instrumentation with a passband up to 600 keV.

6.3 Magnetar physics

Both Soft Gamma–Ray Repeaters (SGR) and Anomalous X–ray Pulsars (AXP) are now well established members of the same class of objects known as magnetars, i.e., neutron stars with super-strong magnetic fields ($B = 10^{14}$–10^{16} G) (see review in Ref. [54]). SGRs were known at high energies from many years during their burst–like activity and giant flares (e.g., Ref. [51]), while AXPs were known to be persistent sources with pulsar peridiocities in the 2–8 s range and very soft X-ray ($\leq$ 10 keV) spectra (blackbody plus a power-law with index between 2 and 4). Nowadays we know that also SGRs show similar periodicities during their quiescence states and that AXPs show burst-like activity. However the softness of the AXP spectra did not predict detections at energies above 10 keV. So it was with a great surprise that the imaging instrument IBIS aboard the INTEGRAL satellite measured hard X-rays (see Ref. [48, 56] and references therein).

Broad band spectra of the persistent emission from these sources beyond 10 keV can be described with a power law with photon index less than 2, which would imply a divergent energy output in the case of no spectral cutoff. However, the cutoff energies have not been measured yet (see an example in Fig. 6.3). Thus the question of the physical origin of the high energy component (>100 keV) in magnetars, for which there are several models (see,

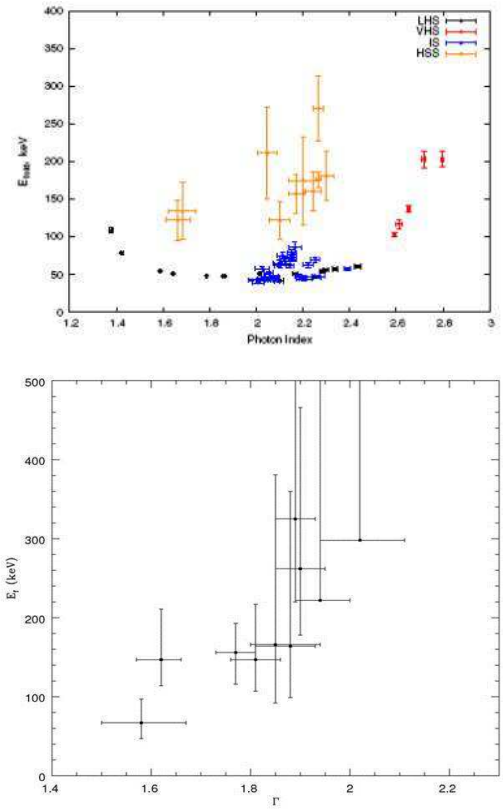

Figure 6.2: *Top panel*: Dependence the cutoff energy versus the photon index for the black hole transient source XTE J1550−564. Reprinted from Ref. [88]. *Bottom panel*: Dependence of the cutoff energy versus the photon index for a sample of Seyfert 1 (radio-quiet AGNs) observed with *BeppoSAX*. Reprinted from Ref. [74].

e.g., Ref. [87]), can be solved only with the focusing telescope of the type proposed here. Indeed from the lens sensitivity in 10^5 s shown in Fig. 5.22, we get, in the units shown in Fig. 6.3, a limiting sensitivity of about 2×10^{-7} MeV cm^{-2} s^{-1} MeV^{-1}, which is about 3 order of magnitude lower than the upper limit shown in the figure.

6.4 Accretion physics in Active Galactic Nuclei (AGN)

In the case of radio–quiet AGNs, like Seyfert galaxies, high energy observations allow one to probe the inner regions of the accretion disk and, in particular, the properties of

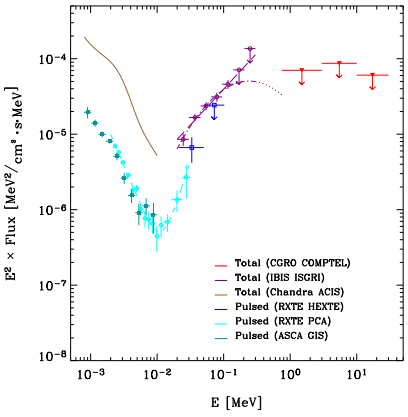

Figure 6.3: Example of the status of our knowledge of the X–/gamma–ray spectra of AXPs and SGRs: the case of the AXP 4U 0142+61. Reprinted from Ref. [56].

the corona around the Massive Black Hole (MBH). While there is general consensus that the X–ray emission is due to Comptonization of UV/soft X–ray disk photons off this hot corona, the coronal electron temperature and its optical depth are poorly known, given that most of them can be observed beyond 100 keV, where the sensitivity of the current instrumentation is background limited (see, e.,g. Fig. 6.1). The most sensitive attempts were done with *BeppoSAX* (see Ref. [74]) with the results shown in Fig. 6.2 bottom panel. More recently, broad band observations with INTEGRAL and a variety of soft X-ray telescopes have made another step in the measurement of high energy cut-offs. Even with all the limitation given by this type of analysis (spectral complexity and non simultaneity of the soft and hard X-ray data), a number of cut-offs have been measured and lower limits reported for complete sample of AGNs. The distribution of the measured cut off energies clusters around 100 keV, while the bulk of the lower limits on this parameter are found below 300 keV [6]. One must then conclude that the high energy cut-off is present and that only the joint use of focusing telescopes, like those aboard *NuSTAR*, combined with a Laue lens to probe the energy range above 100 keV, can solve this issue.

In the case of radio-loud AGNs (Blazars), with prominent jets, the spectra show two main humps, one peaking from millimeter to the X–ray spectral range, the other from the hard X–ray to the high energy gamma–ray range. The first peak is is interpreted as due to synchrotron emission, while the second one as due to Inverse Compton. The highest luminosity Blazars are Flat Spectrum Radio Quasars (FSRQ) and show their Compton peak in the passband of Laue lenses (see left panel of Fig. 6.4), while BL-Lac blazars show, in the energy passband of Laue lenses, the expected dip between the two humps. Only with a sensitive instrument beyond 100 keV, like the Laue lens we are proposing here, we can detect the expected dip between humps and confirm the current models.

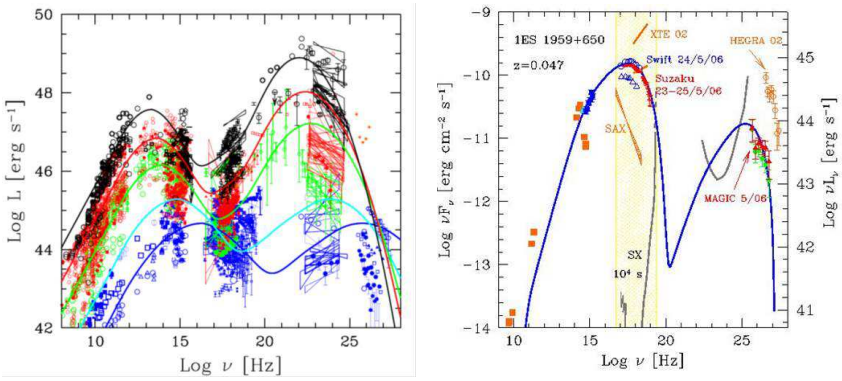

Figure 6.4: *Left panel*: Broad band spectra of blazars of increasing luminosity. Reprinted from Ref. [44]. *Riglt panel*: Example of a blazar source (the BL-Lac source 1ES 1959+650)that shows its expected dip at about 400 keV, that could be detected with the Laue lens we are proposing. Reprinted from Ref. [43].

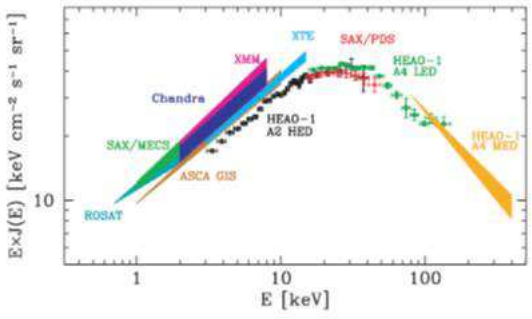

Figure 6.5: EF(E) spectrum of the Cosmic X–ray Background. Reprinted from Ref. [37].

6.5 Origin of the Cosmic X–ray Background

The Cosmic X–ray background (CXB) is characterized by a $EF(E)$ spectrum with a peak around 30 keV followed by a well defined decrease beyond this energy (see Fig. 6.5). Currently, in the X-ray band the CXB has been substantially resolved in terms of obscured and unobscured AGNs (e.g., Ref. [104]), while, around 30 keV, the background composition is being investigated with *NuSTAR* [1].

Instead, the origin of the slope of the spectrum above 30 keV is still debated. CXB synthesis models [47] assume a combination of unobscured, Compton thin and Compton thick radio-quiet AGN populations with different photon index distributions and fixed high

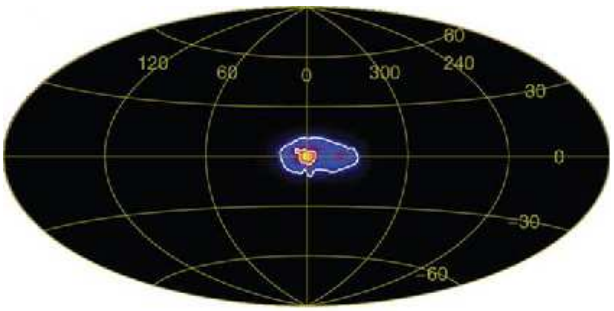

Figure 6.6: Distribution in Galactic coordinates of the positron-annihilation line. Reprinted from Ref. [99].

energy spectral cutoff E_c. However we know from the observation of the strongest AGNs that E_c changes from an AGN to another. Thus it is not realistic to assume a fixed E_c. In addition to radio-quiet AGNs, a contribution to the high energy part of CXB is certainly due to blazars, their real contribution is still matter of discussion due to the absence of deep observations beyond 70–100 keV, where they show their maximum power [43]. The best spectral studies of blazars can be done only extending the energy band of focusing instruments like those aboard *NuSTAR* beyond 100 keV. This can only be obtained by including Laue lenses in future missions.

6.6 Positron astrophysics

Positron production occurs in a variety of cosmic explosions and acceleration sites, and the observation of the characteristic 511 keV annihilation line provides a powerful tool to probe plasma composition, temperature, density and ionization degree. The positron annihilation signature is readily observed from the Galactic bulge region, but yet the origin of the positrons remains mysterious. A SPI/INTEGRAL all-sky map [99] of galactic e^-e^+ annihilation radiation shows an asymmetric distribution of 511 keV emission with a total flux of 1×10^{-3} photons cm^{-2} s^{-1} (see Fig. 6.6). However its origin is still a mystery. The annihilation line can be due to the integrated contribution of positron annihilation features from low mass X-ray binaries with strong emission at photon energies >20 keV (hard LMXBs), as suggested by the authors of the *INTEGRAL* discovery, but it could also have a different origin. For example, it could be due to the presence of antimatter, or to dark matter annihilation as proposed in Ref. [32], or to the existence of a source of radioactive elements, like ^{26}Al, ^{56}Co, ^{44}Ti, or finally to the presence of a Gamma–ray source (e.g., a Gamma–ray pulsar).

To unveil the mystery about the origin of the 511 keV line from the Galactic Center

Region, much more sensitivity and angular resolution is needed, achievable only with Laue lenses. In the lens configuration that we propose in this thesis, the sensitivity to a positron annihilation line is 4 orders of magnitude better than the observed integrated line flux.

6.7 Unveiling the GRB hard X-ray afterglow emission

Despite the enormous progress occurred in the last 20 years, the Gamma-Ray Bursts (GRB) phenomenon is still far to be fully understood. One of the most important open issues is the afterglow emission above 10 keV, which is almost completely unexplored, as a result of the lack of sensitive of detectors operating in this energy band. The only detection of the hard X-ray emission from a GRB (the very bright GRB 990123) performed with the BeppoSAX/PDS instrument (15-200 keV), combined with optical and radio observations, have seriously challenged the standard scenario.

In this scenario the dominant mechanism is synchrotron radiation produced in the shock of an ultra-relativistic fireball with the ISM, showing the need of a substantial revision of current models [17, 67]. The possibility to focus hard X–rays up to several hundreds of keV can provide an important breakthrough in this field, through follow-up observations of bright GRBs detected and localized by GRB dedicated experiments.

6.8 High sensitivity polarization measurements

Several classes of sources (e.g., NS and BH in binary systems, AGNs, GRBs) are expected to show hard X–ray polarization. The last discovery of a polarized component in the Cygnus X–1 spectrum above 400 keV confirms the expectations. With Laue lenses, thanks to the focusing capability, with a proper focal plane detector, the possibility of discovering new polarized components from celestial sources becomes solid. We expect exciting results in this field.

Chapter 7

Conclusions and Prospects

The main goal of this Thesis is the design of a broad band (70/100–600 keV) focusing telescope configuration for unprecedented observations of Galactic and extra-galactic objects. Motivated by the astrophysical importance of extending the focusing band up to 600 keV, with the support of the Italian Space Agency, that approved, first, project named HAXTEL (Hard X-ray Telescope) and thus a project still ongoing, named LAUE, the design of broad band (70/100–600 keV) Laue lenses was started. Two prototypes of Laue lenses made of flat mosaic crystals with short focal length (6 m) have been developed within the framework of the HAXTEL project [38, 39, 95], while, within the framework of the LAUE project a prototype of lens petal made of curved crystals is being assembled in the LARIX facility of the Physics and Earth Sciences Department of the University of Ferrara.

I have been involved in both projects, with the goal of developing a code that simulates both a lens petal and an entire Laue lens like that foreseen to be developed. With this code, written in *Python*, I have, first, established the best crystal and lens parameters of the second lens prototype for the HAXTEL project. A comparison of the experimental results of the developed prototype with expectations was also made [92].

The developed prototype is made of 20 Copper (111) mosaic crystals. It was modeled and engineered to focus hard X-rays of energy centered around 100 keV. The mosaic crystal parameters were initially estimated and then the on–axis Point Spread Function was also modeled, correcting for the effect of diverging beam. The results of this activity was presented [94] at the SPIE Optical Engineering and Applications Conference held in the last week of August 2011 in San Diego (CA, USA).

As part of the thesis, the reflectivity of the bent crystals of perfect Germanium (111) and mosaic Gallium Arsenide (220) – are also simulated. These bent crystals are used to design both a lens petal with 20 m focal length and passband from 90 to 300 keV, and an entire Laue lens with the same focal length and passband from 90 to 600 keV.

I have performed the simulation of the petal structure of the lens petal that is being built. Initially, the frame of the petal is designed, optimizing different parameters and

considering various factors. The details are given in Chapter 4. The on–axis performances of the petal, like PSF, its Full Width Half Maximum (FWHM), and peak intensity are simulated. The design as well as the crystal characterization for the petal were presented at the SPIE Astronomical Telescopes and Instrumentation conference held in Amsterdam in July 2012 [62, 90] and are reported in the thesis.

The simulations made for the petal are extended to model a complete Laue lens, with an energy passband from 90 – 600 keV. The on-axis PSF, its FWHM, its Half Power radius (HPR), effective area and sensitivity (to continuum and to narrow emission lines) of the entire Laue lens has also been modeled. The sensitivity results show that this lens is almost 3 orders of magnitude more sensitive (see Table 5.8 and 5.9) than ISGRI [15] and SPI [29] on-board the INTEGRAL satellite. The results of these simulations were presented [40, 63, 91, 93] at the SPIE Optics and Photonics conference in San Diego in August 2013.

The scientific aspects [40] that can be explored using the Laue lens is also deeply studied (see Chapter 6). With the sensitivity that this lens can achieve, many fundamental open astrophysical cases can be very well settled.

7.1 Future enhancements

The results so far obtained are very promising for future improvements.

1. The thickness of the crystal tile that is being used is 2 mm, which is the maximum thickness, of the crystal tiles that can be bent with a radius of 40 meters using the current bending technology [13, 49]. Using bent crystals with thickness not just restricting to 2 mm, but varying according to band of energy will yield better peak reflectivity (see Figure 2.4 in Chapter 2). In addition, new technologies to increase the maximum thickness to be bent are to be developed. New technologies have to be developed to this purpose.

2. The crystals are permanently attached to the lens frame using a glue, which takes at least 2 hours to polymerise. Assembling more than 24,000 crystals for the entire lens (see Table 5.2 in Chapter 5), will be time consuming. A more efficient solution has to be found.

Activities carried out during PhD

Conferences and Seminars:

- Visit to the ICRANet center in Pescara:
  1-13 October, 2010;
- "IRAP Ph.D. Erasmus Mundus Workshop",
  March 21th-26th, 2011, Pescara (Italy);
- 25th Symposium of Relativistic Astrophysics "Texas 2010",
  Heidelberg, Germany: December 6th-10th, 2010;
- SPIE Optics and Photonics Conference,
  San Diego, California USA: 19 - 23 Aug, 2011;
- "Second Ferrara Workshop on X-Ray astrophysics up to 511keV",
  Ferrara, Italy: 14th-16th September, 2011;
- "RJR-70" Meeting,
  University of La Sapienza, Rome, Italy: 5 - 7 June, 2012;
- SPIE Astronomical Instrumentation and Telescopes Conference,
  Amsterdam, Netherlands: 1 - 6 July, 2012;
- "Marcel Grossmann" meeting,
  Stockholm, Sweden: 1st - 7th July, 2012;
- SPIE Optics and Photonics Conference,
  San Diego, California USA: 25 - 29 Aug, 2013.

Courses, Activity and Certificates

- First certificate in Italian language;
- "Temporal data analysis: Theory and Procedures",
  Prof. Mauro Orlandini (40 hours course);
- "Observation techniques of astrophysical X-rays and Gamma rays",
  Prof. Filippo Frontera (40 hours course)
- "Spectrum energy correlations in GRBs",
  Prof. Lorenzo Amati (40 hours course);
- "Detectors for High Energy Astrophysics",
  Prof. Ezio Caroli (20 hours course);
- "Computational analysis of crystal diffraction",
  Dr. Manuel Sànchez Del Rìo,
  Instrumentation Services and Development Division
  European Synchroton Radiation Facility (ESRF), Grenoble.

Schools and Workshops:

- Erasmus mundus School, Nice, France:
  6-30 Setpember 2010;
- Erasmus Mundus Workshop, Les Houches, France:
  3rd- 8th April, 2011;
- Erasmus Mundus School, Nice, France:
  22 May - 11 June, 2011;
- Erasmus Mundus School, Nice, France:
  5th - 16th September, 2011;
- Erasmus Mundus School, Nice, France:
  3rd – 21st September, 2012;

Presentations and Poster:

- "Laue lenses for hard X–/soft gamma–rays: new prototype results",
  SPIE Optics and Photonics conference,
  San Diego, USA. August 2011.
- "Test results of a new Laue lens prototype for soft gamma-rays",
  Second Ferrara workshop on X-ray Astrophysics upto 511 keV,
  Ferrara, Italy. September 2011.
- "Expected performance of a Laue lens based on bent crystals",
  SPIE Astronomical telescopes and Instrumentation conference,
  Amsterdam. July 2012.
- "Laue lenses for hard X–/soft gamma rays: From retrospective modeling to prospective performance.",
  Erasmus Mundus School,
  Nice, France, September 2012.
- "Results of the simulations of the petal/lens as part of the LAUE project ",
  SPIE Optics and Photonics conference,
  San Diego, USA. August 2013.

Bibliography

[1] D. M. Alexander, D. Stern, A. Del Moro, G. B. Lansbury, R. J. Assef, and et al. The NuSTAR extragalactic survey: A first sensitive look at the high-energy cosmic X-ray background population: Arxiv e-prints. July 2013.

[2] B. Aschenbach, H. Braeuninger, U. Briel, W. Brinkmann, H. Fink, N. Heinecke, H. Hippmann, G. Kettenring, G. Metzner, and A. Ondrusch. The rosat mission. *Space Science Reviews*, 30:569–573, 1981.

[3] André Authier. *Dynamical Theory of X–ray Diffraction*. IUCr OXFORD, 2003.

[4] H. Barré, H. Nye, and G. Janin. An overview of the xmm observatory system. *ESA Bulletin*, 100:15–20, Dec. 1999.

[5] N. M. Barriere, J. Rousselle, P. von Ballmoos, N. V. Abrosimov, P. Courtois, P. Bastie, T. Camus, M. Jentschel, V. N. Curlov, L. Natalucci, G. Roudil, N. F. Brejnholt, and D. Serre. Experimental and theoretical study of diffraction properties of various crystalls for the realization of a soft–gamma ray laue lens. *Journal of Applied Crystallography*, 2009.

[6] L. Bassani, M. Molina, A. Malizia, F. Panessa, R. Landi, A. Bazzano, P. Ubertini, A. J. Bird, and J. B. Stephen. Review on active galactic nuclei at hard x-ray energies: Arxiv e-prints. Feb. 2013.

[7] V. Bellucci, R. Camattari, V. Guidi, I. Neri, and N. Barrière. Self-standing bent silicon crystals for very high efficiency laue lens. *Experimental Astronomy*, 31:45–58, aug 2011.

[8] K. Bennett. COS-B: The highlights. *Nuclear Physics B Proceedings Supplements*, 14:23–34, April 1990.

[9] A. J. Bird, A. Bazzano, L. Bassani, F. Capitanio, M. Fiocchi, A. B. Hill, and et al. The fourth IBIS/ISGRI soft gamma-ray survey catalog. *The Astrophysical Journal Supplement*, 186:1–9, Jan. 2010.

[10] A. Boeuf, S. Lagomarsino, S. Mazkedian, S. Melone, P. Puliti, and F. Rustichelly. *Journal of Applied Cryst.*, 11:442–449, 1978.

[11] W. H. Bragg and W. L. Bragg. In *Proc. Roy. Soc. London*, volume 88, page 428, 1913.

[12] W. H. Bragg and W. L. Bragg. In *Proc. Roy. Soc. London*, volume 89, page 246, 1913.

[13] E. Buffagni, C. Ferrari, F. Rossi, L. Marchini, and A. Zappettini. Preparation of bent crystals as high-efficiency optical elements for hard x-ray astronomy. volume 8443 of *Society of Photo-Optical Instrumentation Engineers (SPIE) Conference Serie*, 2012.

[14] B. E. Burke, R. W. Mountain, P. J. Daniels, M. J. Cooper, and V. S. Dolat. Ccd soft x-ray imagers for asca and axaf. In O. H. Siegmund, editor, *Society of Photo-Optical Instrumentation Engineers (SPIE) Conference Series*, volume 2006 of *Society of Photo-Optical Instrumentation Engineers (SPIE) Conference Series*, pages 272–285, Nov. 1993.

[15] G. Bélanger. *INTEGRAL IBIS Observer's Manual*. ESA, 1.0 edition, March 2012.

[16] R. Camattari, V. Guidi, and I. Neri. Quasi-mosaicity as a tool for focusing hard x-rays. In *Society of Photo-Optical Instrumentation Engineers (SPIE) Conference Series*, volume 8443 of *Society of Photo-Optical Instrumentation Engineers (SPIE) Conference Series*, sep 2012.

[17] A. Corsi, L. Piro, E. Kuulkers, L. Amati, L. A. Antonelli, and et al. The puzzling case of GRB 990123: prompt emission and broad-band afterglow modeling. *Astronomy and Astrophysics*, 438:829–840, Aug. 2005.

[18] E. Costa, F. Frontera, J. Heise, M. Feroci, J. in't Z, and F. Fiore. Discovery of an X-ray afterglow associated with the -ray burst of 28 february 1997. *Nature*, 387:783–785, 1997.

[19] G. Cusumano, V. La Parola, A. Segreto, C. Ferrigno, A. Maselli, and et al. The Palermo Swift-BAT hard X-ray catalogue. III. Results after 54 months of sky survey. *Astronomy and Astrophysics*, 524:A64, Dec. 2010.

[20] A. D'Aí, P. Życki, T. Di Salvo, R. Iaria, G. Lavagetto, and N. R. Robba. Broadband spectral evolution of scorpius x-1 along its color-color diagram. *The Astrophysical Journal*, 667:411–426, Sept. 2007.

[21] C. G. Darwin. *Phil. Mag.*, 27(315):657, 1914.

[22] C. G. Darwin. *Phil. Mag.*, 43:800, 1922.

[23] P. A. J. de Korte, J. A. M. Bleeker, S. P. McKechnie, A. J. F. den Boggende, A. C. Brinkman, E. H. B. M. Gronenschild, G. Branduardi-Raymont, J. L. Culhane, and I. Mason. The x-ray imaging telescopes on exosat. *European Space Agency, ESLAB Symposium on X-ray Astronomy*, 30:495–511, March 1981.

[24] A. J. Dean. Background sensitivity and mission scenario. Gamma ray telescope project design study, 2012.

[25] M. Sànchez del Rio, C. Ferrero, and V. Mochella. Computer simulations of bent perfect crystal diffraction profiles. *SPIE Proceedings*, 3151:312–323, 1997.

[26] R. Diehl, H. Halloin, K. Kretschmer, G. G. Lichti, V. Schönfelder, A. W. Strong, A. von Kienlin, W. Wang, P. Jean, J. Knödlseder, J. Roques, G. Weidenspointner, S. Schanne, D. H. Hartmann, C. Winkler, and C. Wunderer. Radioactive ^{26}Al from massive stars in the galaxy. *Nature*, 439:45–47, Jan. 2006.

[27] R. Farinelli, F. Frontera, A. A. Zdziarski, L. Stella, S. N. Zhang, M. van der Klis, N. Masetti, and L. Amati. The transient hard X-ray tail of GX 17+2: New beppoSAX results. *Astronomy and Astrophysics*, 434:25–34, Apr. 2005.

[28] R. Farinelli, L. Titarchuk, A. Paizis, and F. Frontera. A new comptonization model for weakly magnetized, accreting neutron stars in low-mass X-ray binaries. *The Astrophysical Journal*, 680:602–614, June 2008.

[29] C. Sánchez Fernández. *INTEGRAL SPI Observer's Manual*. ESA, 1.0 edition, March 2012.

[30] F. Ferrari, F. Frontera, G. Loffredo, E. Virgilli, C. Guidorzi, V. Carassiti, F. Evangelisti, L. Landi, S. Chiozzi, S. Squerzanti, E. Caroli, J. B. Stephen, F. Shiavonne, A. Basili, K. H. Andersen, and P. Courtois. New results on focusing of gamma rays with laue lenses. In Stephen L. O'Dell and Giovanni Pareschi, editors, *Optics for EUV, X-Ray, and Gamma-Ray Astronomy III*, volume 7437-19 of *Proceedings of the SPIE*, page 6688. Presented at the Society of Photo-Optical Instrumentation Engineers (SPIE) Conference, 2009.

[31] C. E. Fichtel, R. C. Hartman, D. A. Kniffen, D. J. Thompson, H. Ogelman, M. E. Ozel, T. Tumer, and G. F. Bignami. High-energy gamma-ray results from the second small astronomy satellite. *Astrophysical Journal*, 198:163–182, May 1975.

[32] D. P. Finkbeiner and N. Weiner. Exciting dark matter and the INTEGRAL/SPI 511keV signal. *Physical Review* D, 76(083519), Oct. 2007.

[33] F. Frontera. Hard x–ray imaging via focusing optics with mosaic crystals. *Experimental Astronomy*, 2:25, 1995.

[34] F. Frontera and P. Von Ballmoos. Laue gamma-ray lenses for space astrophysics: status and prospects. *astro-ph.IM*, 2011.

[35] F. Frontera, E. Costa, D. Dal Fiume, M. Feroci, L. Nicastro, M. Orlandini, and G. Zavattini. Performance of the sax/pds high energy x-ray telescope. In *International Cosmic Ray Conference*, volume 2 of *International Cosmic Ray Conference*, page 41, 1995.

[36] F. Frontera, G. Loffredo, A. Pisa, F. Nobili, V. Carassiti, F. Evangelisti, L. Landi, S. Squerzanti, E. Caroli, J. B. Stephen, K. H. Anderson, P. Courtois, N. Auricchio, L. Milani, and B. Negri. Focusing of gamma-rays with laue lenses: first results. In *Society of Photo-Optical Instrumentation Engineers (SPIE) Conference Series*, page 7011. SPIE, 2008.

[37] F. Frontera, M. Orlandini, R. Landi, A. Comastri, F. Fiore, G. Setti, L. Amati, E. Costa, N. Masetti, and E. Palazzi. The cosmic x-ray background and the population of the most heavily obscured AGNs. *The Astrophysical Journal*, 666:86–95, 2007.

[38] F. Frontera, E. Virgilli, V. Liccardo, **V. Valsan**, V. Carassiti, S. Chiozzi, F. Evangelisti, S. Squerzanti, M. Statera, V. Guidi, C. Ferrari, R. A. Zappettini, E. Caroli, N. Auricchio, S. Silvestri, R. Camattari, F. Cassese, L. Recanatesi, M. Pecora, S. Mottini, and B. Negri. Development status of the laue project. In *Society of Photo-Optical Instrumentation Engineers (SPIE) Conference Series*, volume 8443 of *Society of Photo-Optical Instrumentation Engineers (SPIE) Conference Series*, Sep. 2012.

[39] F. Frontera, E. Virgilli, V. Liccardo, **V. Valsan**, V. Carassiti, F. Evangelisti, S. Squerzanti, and G. Risaliti. Gamma-ray laue lenses under development for deep agn observations. *Journal of Physics Conference Series*, 355(1):012005, March 2012.

[40] F. Frontera, E. Virgilli, **V. Valsan**, V. Liccardo, V. Carassiti, E. Caroli, F. Cassase, L. Recanatesi C. Ferrari, V. Guidi, M. Pecora, S.Mottini, L. Amati, N. Auricchio, L. Bassani, R. Campana, R. Farinelli, C. Guidorzi, C. Labanti, R. Landi, A. Malizia, M. Orlandini, V. Sguera, J. B. Stephen, and L. G. Titarchuk. Scientific prospects in soft gamma-ray astronomy thanks to the laue project. volume 8861, 2013.

[41] N. Gehrels. The swift gamma-ray burst mission. In *American Astronomical Society Meeting Abstracts*, volume 36 of *Bulletin of the American Astronomical Society*, page 116.01, Dec. 2004.

[42] N. Gehrels, G. Chincarini, P. Giommi, K. O. Mason, and et al. The swift gamma-ray burst mission. *The Astrophysical Journal*, 611:1005–1020, Aug. 2004.

[43] G. Ghisellini. Blazars in hard x-rays. In J. Rodriguez and P. Ferrando, editors, *American Institute of Physics Conference Series*, volume 1126 of *American Institute of Physics Conference Series*, pages 131–136, May 2009.

[44] G. Ghisellini. Extragalactic relativistic jets: Arxiv e-prints. Mar. 2011.

[45] R. Giacconi, G. Branduardi, U. Briel, A. Epstein, D. Fabricant, E. Feigelson, W. Forman, P. Gorenstein, J. Grindlay, H. Gursky, F. R. Harnden, J. P. Henry, C. Jones, E. Kellogg, D. Koch, S. Murray, E. Schreier, F. Seward, H. Tananbaum, K. Topka, L. Van Speybroeck, S. S. Holt, R. H. Becker, E. A. Boldt, P. J. Serlemitsos, G. Clark,

C. Canizares, T. Markert, R. Novick, D. Helfand, and K. Long. The Einstein /HEAO 2/ X-ray observatory. *Astrophysical Journal*, 230:540–550, June 1979.

[46] R. Giacconi, E. Kellogg, P. Gorenstein, H. Gursky, and H. Tananbaum. An x-ray scan of the galactic plane from uhuru. *Astrophysical Journal*, 165:L27, April 1971.

[47] R. Gilli, A. Comastri, and G. Hasinger. The synthesis of the cosmic X-ray background in the chandra and XMM-Newton era. *Astronomy and Astrophysics*, 463:79–96, Feb. 2007.

[48] D. Götz, S. Mereghetti, A. Tiengo, and P. Esposito. Magnetars as persistent hard X-ray sources: INTEGRAL discovery of a hard tail in SGR 1900+14. *Astronomy and Astrophysics*, 449:L31–L34, April 2006.

[49] V. Guidi, V. Bellucci, R. Camattari, and I. Neri. Bent crystals by superficial grooves for high-efficiency concentration of hard x-ray photons by a laue lens. volume 28 of *The Second Ferrara Workshop on "X-ray Astrophysics up to 511 keV*, 2011.

[50] Vincenzo Guidi, Valerio Bellucci, Riccardo Camattari, and Ilaria Neri. Proposal for a laue lens with quasi-mosaic crystalline tiles. *Journal of Applied Crystallography*, 44(6):1255–1258, 2011.

[51] C. Guidorzi, F. Frontera, E. Montanari, M. Feroci, L. Amati, E. Costa, and M. Orlandini. Comparative study of the two large flares from sgr1900+14 with the beppoSAX gamma-ray burst monitor. *Astronomy and Astrophysics*, 416:297–310, March 2004.

[52] H. Halloin, P. von Ballmoos, J. Evrard, G. K. Skinner, M. Hernanz, N. V. Abrosimov, P. Bastie, B. Hamelin, V. Lonjou, J. M. Alvarez, A. Laurens, P. Jean, J. Knödleseder, R. K. Smither, and G. Vedrenne. Claire gamma-ray lens: flight and long-distance test results. In *Society of Photo-Optical Instrumentation Engineers (SPIE) Conference Series*, volume 5168, pages 471–481, Feb. 2004.

[53] F. A. Harrison, W. W. Craig, F. E. Christensen, C. J. Hailey, W. W. Zhang, and et al. The Nuclear Spectroscopic Telescope Array (NuSTAR) high-energy X-ray mission. *The Astrophysical Journal*, 2013.

[54] K. Hurley. Soft gamma repeaters. volume 81. Memorie Societá Astronomica Italiana, 2010.

[55] K. D. Joensen, F. E. Christensen, H. W. Schnopper, P. Gorenstein, J. Susini, P. Høghøj, R. Hustache, J. Wood, and K. Parker. Medium-sized grazing incidence high-energy x-ray telescopes employing continuously graded multilayers. In *Society of Photo-Optical Instrumentation Engineers (SPIE) Conference Series*, volume 2009, pages 239–248. SPIE, Dec. 1993.

[56] L. Kuiper, W. Hermsen, P. R. den Hartog, and W. Collmar. Discovery of luminous pulsed hard X-ray emission from anomalous X-ray pulsars 1RXS J1708-4009, 4U 0142+61, and 1E 2259+586 by INTEGRAL and RXTE. *The Astrophysical Journal*, 645:556–575, July 2006.

[57] P. Laurent, J. Rodriguez, J. Wilms, M. Cadolle Bel, K. Pottschmidt, and V. Grinberg. Polarized gamma-ray emission from the galactic black hole Cygnus X-1. *Science*, 2011.

[58] P. Laurent and L. Titarchuk. Spectral index as a function of mass accretion rate in black hole sources: Monte carlo simulations and an analytical description. *The Astrophysical Journal*, 727:34, Jan. 2011.

[59] P. Laurent and L. Titarchuk. Pair production close to black hole horizon. volume 39. COSPAR Meeting, 39th COSPAR Scientific Assembly, July 2012.

[60] F. Lebrun, J. P. Leray, P. Lavocat, J. Crétolle, and M. Arquès et al. ISGRI: The integral soft gamma-ray imager. *Astronomy and Astrophysics*, 411:L141–L148, November 2003.

[61] M. D. Leising, D. D. Clayton, W. N. Johnson, R. L. Kinzer, J. D. Kurfess, M. S. Strickman, D. A. Grabelsky, W. R. Purcell, M. P. Ulmer, R. A. Cameron, and G. V. Jung. Cgro/osse observations of recent supernovae: Sn1987a and sn 1991t. In *Bulletin of the American Astronomical Society*, volume 23 of *Bulletin of the American Astronomical Society*, page 1353, Sep. 1991.

[62] V. Liccardo, E. Virgilli, F. Frontera, and **V. Valsan**. Characterization of bent crystals for laue lenses. In *Society of Photo-Optical Instrumentation Engineers (SPIE) Conference Series*, volume 8443 of *Society of Photo-Optical Instrumentation Engineers (SPIE) Conference Series*, Sep. 2012.

[63] V. Liccardo, E. Virgilli, F. Frontera, **V. Valsan**, V. Guidi, and E. Buffagni. Bent crystal selection and assembling for the laue project. In *Society of Photo-Optical Instrumentation Engineers (SPIE) Conference Series*, volume 8861 of *Society of Photo-Optical Instrumentation Engineers (SPIE) Conference Series*, Sep. 2013.

[64] G. Loffredo, F. Frontera, D. Pellicciotta, A. Pisa, V. Carassiti, S. Chiozzi, F. Evangelisti, L. Landi, M. Melchiorri, and S. Squerzanti. The ferrara hard x-ray facility for testing/calibrating hard x-ray focusing telescopes. *Experimental Astronomy*, 20:413–420, Dec. 2005.

[65] N. Lund, C. Budtz-Jørgensen, N. J. Westergaard, S. Brandt, I. L. Rasmussen, A. Hornstrup, C. A. Oxborrow, J. Chenevez, P. A. Jensen, S. Laursen, K. H. Andersen, P. B. Mogensen, I. Rasmussen, K. Omø, S. M. Pedersen, J. Polny, H. Andersson, T. Andersson, V. Kämäräinen, O. Vilhu, J. Huovelin, S. Maisala, M. Morawski, G. Juchnikowski, E. Costa, M. Feroci, A. Rubini, M. Rapisarda,

E. Morelli, V. Carassiti, F. Frontera, C. Pelliciari, G. Loffredo, S. Martínez Núñez, V. Reglero, T. Velasco, S. Larsson, R. Svensson, A. A. Zdziarski, A. Castro-Tirado, P. Attina, M. Goria, G. Giulianelli, F. Cordero, M. Rezazad, M. Schmidt, R. Carli, C. Gomez, P. L. Jensen, G. Sarri, A. Tiemon, A. Orr, R. Much, P. Kretschmar, and H. W. Schnopper. Jem-x: The x-ray monitor aboard integral. *Astronomy and Astrophysics*, 411:L231–L238, Nov. 2003.

[66] T. Maiolino, F. D'Amico, and J. Braga. INTEGRAL observations of scorpius X-1: evidence for comptonization up to 200 kev. *Astronomy and Astrophysics*, 551:L2, Mar. 2013.

[67] E. Maiorano, N. Masetti, E. Palazzi, F. Frontera, P. Grandi, and et al. The puzzling case of GRB 990123: multiwavelength afterglow study. *Astronomy and Astrophysics*, 438:821–827, Aug. 2005.

[68] L. Marchini, E. Buffagni, C. Ferrari, F. Rossi, and A. Zappettini. Bent crystals as high efficiency optical elements for hard x-ray astronomy. volume 40 of *The Second Ferrara Workshop on "X-ray Astrophysics up to 511 keV*, 2011.

[69] S. Markoff, H. Falcke, and R. Fender. A jet model for the broadband spectrum of XTE J1118+480. synchrotron emission from radio to X-rays in the low/hard spectral state. *Astronomy and Astrophysics*, 372:L25–L28, June 2001.

[70] A. Paizis, R. Farinelli, L. Titarchuk, T. J.-L. Courvoisier, A. Bazzano, V. Beckmann, F. Frontera, P. Goldoni, E. Kuulkers, S. Mereghetti, J. Rodriguez, and O. Vilhu. Average hard X-ray emission from NS LMXBs: observational evidence of different spectral states in NS LMXBs. *Astronomy and Astrophysics*, 459:187–197, Nov. 2006.

[71] A. N. Parmar, C. Winkler, P. Barr, L. Hansson, E. Kuulkers, R. Much, and A. Orr. Integral mission. In *Society of Photo-Optical Instrumentation Engineers (SPIE) Conference Series*, volume 4851, pages 1104–1112, March 2003.

[72] A. Peacock, R. D. Andresen, G. Manzo, B. G. Taylor, G. Villa, S. Re, J. C. Ives, and S. Kellock. The gas scintillation proportional counter on exosat. *European Space Agency, ESLAB Symposium on X-ray Astronomy*, 30:525–534, March 1981.

[73] P. Penning and D. Polder. *Philips Research Reports*, 1961.

[74] G. C. Perola, G. Matt, M. Cappi, F. Fiore, M. Guainazzi, L. Maraschi, P. O. Petrucci, and L. Piro. Compton reflection and iron fluorescence in beppoSAX observations of seyfert type 1 galaxies. *Astronomy and Astrophysics*, 389:802–811, July 2002.

[75] L. E. Peterson. Instrumental technique in x-ray astronomy. *Annual review of astronomy and astrophysics*, 13:423–509, 1975.

[76] L. Piro, L. Scarsi, and R. C. Butler. Sax: the wideband mission for x-ray astronomy. In S. Fineschi, editor, *Society of Photo-Optical Instrumentation Engineers (SPIE) Conference Series*, volume 2517 of *Society of Photo-Optical Instrumentation Engineers (SPIE) Conference Series*, pages 169–181, Oct. 1995.

[77] A. Pisa. *Hard X–ray Optics Development: Feasibility Study of a Laue Lens*. PhD thesis, Universit‘ degli Studi di Ferrara, 2004.

[78] N. Produit. Integral:. a gamma-ray observatory. In R. Battiston and B. Bertucci, editors, *Matter, Anti-Matter and Dark Matter*, pages 199–209, Aug. 2002.

[79] J. P. Roques, S. Schanne, A. von Kienlin, J. Knödlseder, R. Briet, and et al. SPI/INTEGRAL in-flight performance. *Astronomy and Astrophysics*, 411:L91–L100, Nov. 2003.

[80] S. Sakurai, S. Yamada, S. Torii, H. Noda, K. Nakazawa, K. Makishima, and H. Takahashi. Accretion geometry of the low-mass x-ray binary aquila x-1 in the soft and hard states. In *Publications of the Astronomy Society of Japan*, volume 64, page 72, Aug. 2012.

[81] T. Di Salvo, R. Farinelli, L. Burderi, F. Frontera, E. Kuulkers, N. Masetti, N. R. Robba, L. Stella, and M. van der Klis. On the spectral evolution of cygnus x-2 along its color-color diagram. *Astronomy and Astrophysics*, 386:535–547, May 2002.

[82] G. H. Share. Discovery of two cosmic x-ray bursts in 1970. *COSPAR, Symposium on Fast Transients in X- and Gamma-Rays*, 42:29–33, June 1976.

[83] J. H. Swank. The XTE mission. In *American Astronomical Society Meeting Abstracts*, volume 26 of *Bulletin of the American Astronomical Society*, page 1420, Dec. 1994.

[84] S. Takagi. *Journal of Physical Society of Japan*, 26:1239, 1969.

[85] Y. Tanaka. First results from asca. In *American Astronomical Society Meeting Abstracts*, volume 25 of *Bulletin of the American Astronomical Society*, page 1344, Dec. 1993.

[86] D. Taupin. *Bulletin of Society for Mineral Crystellography*, 87:469, 1964.

[87] C. Thompson and A. M. Beloborodov. High-energy emission from magnetars. *The Astrophysical Journal*, 634:565–569, Nov. 2005.

[88] L. Titarchuk and N. Shaposhnikov. Implication of the observed spectral cutoff energy evolution in XTE J1550-564. *The Astrophysical Journal*, 724:1147–1152, Dec. 2010.

[89] M. J. L. Turner, A. Smith, and H. U. Zimmermann. The medium energy instrument on exosat. *European Space Agency, ESLAB Symposium on X-ray Astronomy*, 30:513–524, March 1981.

[90] **V. Valsan**, F. Frontera, E. Virgilli, and V. Liccardo. Expected performance of a laue lens based on bent crystals. In *Society of Photo-Optical Instrumentation Engineers (SPIE) Conference Series*, volume 8443 of *Society of Photo-Optical Instrumentation Engineers (SPIE) Conference Series*, Sept. 2012.

[91] **V. Valsan**, F. Frontera, E. Virgilli, V. Liccardo, E. Caroli, and J. B Stephen. Results of the simulations of the petal/lens as part of the laue project. In *Society of Photo-Optical Instrumentation Engineers (SPIE) Conference Series*, volume 8443 of *Society of Photo-Optical Instrumentation Engineers (SPIE) Conference Series*, Oct. 2013.

[92] **V. Valsan**, E. Virgilli, V. Liccardo, and F. Frontera. Test results of a new laue lens prototype for soft gamma-rays. In *X-ray Astrophysics up to 511 keV*, Sep. 2011.

[93] E. Virgilli, F. Frontera, **V. Valsan**, V. Liccardo, V. Carassiti, F. Evangelisti, S. Sqerzanti, M. Parise, M. Statera, v. Guidi, , V. Bellucci, R. Camattari, E. Caroli, N. Auricchio, A. Basili, S. Silvestri, J. B. Stephen, F. Cassese, L. Recanatesi, C. Ferrari, A. Zappettini, E. Buffagni, S. Mottini, M. Pecora, and B. Negri. The laue project and its main results. volume 8861 of *Society of Photo-Optical Instrumentation Engineers (SPIE) Conference Series*, Sep. 2013.

[94] E. Virgilli, F. Frontera, **V. Valsan**, V. Liccardo, V. Carassiti, F. Evangelisti, and S. Squerzanti. Laue lenses for hard x-/soft γ-rays: new prototype results. In *Society of Photo-Optical Instrumentation Engineers (SPIE) Conference Series*, volume 8147 of *Society of Photo-Optical Instrumentation Engineers (SPIE) Conference Series*, Sep. 2011.

[95] E. Virgilli, F. Frontera, **V. Valsan**, V. Liccardo, E. Caroli, J. B. Stephen, F. Cassese, L. Recanatesi, M. Pecora, S. Mottini, P. Attiná, and B. Negri. The laue project for broadband gamma-ray focusing lenses. In *Society of Photo-Optical Instrumentation Engineers (SPIE) Conference Series*, volume 8147 of *Society of Photo-Optical Instrumentation Engineers (SPIE) Conference Series*, Sep. 2011.

[96] P. von Ballmoos, H. Halloin, J. Paul, N. Abrosimov, K. Andersen, P. Astier, S. Basa, D. Barret, P. Bastie, A. Bazzano, A. Bignami, A. Blanchard, B. Cordier, T. Courvoisier, P. Courtois, A. Ealet, B. Hamelin, M. Harris, M. Hernanz, J. Isern, P. Jean, J. Knödlseder, P. Laurent, F. Lebrun, X. Leyre, O. Limousin, A. Marcowith, V. Martinot, A. Mazure, L. Natalucci, J.-F. Olive, R. Pain, S. Paltani, N. Prantzos, H. Riemann, R. Sadat, H. Sainct, G. Skinner, R. K. Smither, P. Ubertini, F. Vedrenne, and G. Weidenspointner. The max mission: Focusing on high-sensitivity gamma-ray spectroscopy. In V. Schoenfelder, G. Lichti, and C. Winkler, editors, *5th INTEGRAL Workshop on the INTEGRAL Universe*, volume 552 of *ESA Special Publication*, page 747, oct 2004.

[97] M. von Laue. *Munchener Sitzungberichte*, 1912:363, 1913.

[98] M. von Laue. *Ann. der Phys.*, 41:989, 1913.

[99] G. Weidenspointner, G. Skinner, P. Jean, J. Knödlseder, P. von Ballmoos, and et al. An asymmetric distribution of positrons in the galactic disk revealed by γ-rays. *Nature*, 451:159–162, Jan. 2008.

[100] M. C. Weisskopf. The chandra x-ray observatory (CXO): An overview. *ArXiv Astrophysics e-prints*, Dec. 1999.

[101] M. C. Weisskopf. Chandra x-ray optics. *Optical Engineering*, 51(1):011013–1–011013–7, 2012.

[102] M. C. Weisskopf, B. Brinkman, C. Canizares, G. Garmire, S. Murray, and L. P. Van Speybroeck. An overview of the performance and scientific results from the chandra x-ray observatory. *The Publications of the Astronomical Society of the Pacific*, 114:1–24, January 2002.

[103] C. Winkler, T. J.-L. Courvoisier, G. Di Cocco, N. Gehrels, A. Giménez, and et al. The integral mission. *Astronomy and Astrophysics*, 411:L1–L6, Nov. 2003.

[104] Y. Q. Xue, B. Luo, W. N. Brandt, F. E. Bauer, B. D. Lehmer, and et al. The chandra deep field-south survey: 4 Ms source catalogs. *The Astrophysical Journal Supplement*, 195:10, July 2011.

[105] W. H. Zachariasen. *Theory of X-ray Diffraction in Crystals*. Wiley, 1945.